E.O. Paton Electric Welding Institute of the National Academy of Science of Ukraine
International Association «Welding»

The Paton Welding Journal

03
2023

International Scientific-Technical and Production Journal ◊ Founded in January 2000 (12 Issues Per Year)

Address of Editorial Board
E.O. Paton Electric Welding Institute, 11 Kazymyr Malevych Str., 03150, Kyiv, Ukraine
Tel./Fax: (38044) 205 23 90, E-mail: journal@paton.kiev.ua
https://patonpublishinghouse.com/eng/journals/tpwj

State Registration Certificate 24933-14873 ПР from 13.08.2021
ISSN 0957-798X, DOI: http://dx.doi.org/10.37434/tpwj

Subscriptions, 12 issues per year:
$384 — annual subscription for the printed (hard copy) version, air postage and packaging included;
$312 — annual subscription for the electronic version (sending issues in pdf format or providing access to IP addresses).

Representative Office of «The Paton Welding Journal» in China:
China-Ukraine Institute of Welding, Guangdong Academy of Sciences
Address: Room 210, No. 363 Changxing Road, Tianhe, Guangzhou, 510650, China.
Zhang Yupeng, Tel: +86-20-61086791, E-mail: patonjournal@gwi.gd.cn

The content of the journal includes articles received from authors from around the world in the field of welding, metallurgy, material science and selectively includes translations into English of articles from the following journals, published by PWI in Ukrainian:
- Automatic Welding (https://patonpublishinghouse.com/eng/journals/as);
- Electrometallurgy Today (https://patonpublishinghouse.com/eng/journals/sem);
- Technical Diagnostics & Nondestructive Testing (https://patonpublishinghouse.com/eng/journals/tdnk).

CONTENTS

ORIGINAL ARTICLES

*Translated Article(s) from «Automatic Welding», No. 3, 2023.

**Translated Article(s) from «Electrometallurgy Today», No. 1, 2023.

***Translated Article(s) from «Technical Diagnostics & Nondestructive Testing», No. 1, 2023.

DOI: https://doi.org/10.37434/tpwj2023.03.01

INFLUENCE OF THE NATURE OF DISTRIBUTION OF NONMETALLIC INCLUSIONS ON THE MECHANICAL PROPERTIES OF WELD METAL OF LOW-ALLOY STEELS

V.V. Holovko[1], O.O. Shtofel[1], D.Yu. Korolenko[2]

[1]E.O. Paton Electric Welding Institute of the NASU
11 Kazymyr Malevych Str., 03150, Kyiv, Ukraine
[2]National Technical University of Ukraine «Igor Sikorsky Kyiv Polytechnic Institute»
37 Peremohy Prosp., 03056, Kyiv, Ukraine

ABSTRACT

A complex of works was carried out on establishing the nature of distribution of nonmetallic inclusions in the metal structure of low-alloy welds. As a result of metallographic examinations, the values of the volume content of inclusions in the structure and their distribution by sizes were established. The rationality of using such an additional indicator as the distribution density for a more informative description of nonmetallic inclusions when evaluating their influence on the mechanical properties of weld metal was shown. The use of fractal analysis to reveal the features of the distribution density of nonmetallic inclusions in the weld metal was proposed.

KEYWORDS: welds, microstructure, nonmetallic inclusions, distribution density, tendency to brittle fracture, fractal analysis

INTRODUCTION

Nonmetallic inclusions are an integral part of the structure of low-alloy steels and that is why a great attention is traditionally paid to their influence on the mechanical properties of welds. It is believed that nonmetallic inclusions in the welding pool are formed as a result of the course of thermodynamic reactions or they enter when melting base metal and welding consumables. Fundamental monographs on this issue [1, 2] showed the features of the influence of the volume content of inclusions, their chemical composition and morphology on the formation of structure and mechanical properties of welds. The carried out studies have shown that some inclusions of a certain morphology may contribute to the formation of microstructural components of a higher toughness in the weld metal of low-alloy steels. Based on these results, the researchers came to the idea not to count on the formation of the required nonmetallic inclusions in the weld metal, but to provide their presence in the metal by inoculation of a controlled number of refractory compounds of a certain size and chemical composition to the welding pool. Recently, publications appeared, which study the features of influence on the structure and mechanical properties of the weld metal of nonmetallic inclusions, which were purposefully inoculated to the welding pool [3, 4]. In a high-temperature metal melt, nonmetallic inclusions are dissolved. Therefore, in order to inhibit this process in relation to inoculants, they are introduced into the "cold" area of welding pool. Accordingly, the conditions of distribution of nonmetallic inclusions in the weld metal are changed. Our research works were aimed at finding out the peculiarities of the distribution of nonmetallic inclusions in the structure of weld metal of low-alloy steels, expanding the knowledge base regarding the influence of certain indicators describing these features on the mechanical properties of the weld metal of low-alloy steels, in particular, the tendency to brittle fracture.

The aim of the work was to determine the possibility of taking into account the distribution density of nonmetallic inclusions in the metal matrix when evaluating their influence on the mechanical properties of weld metal of low-alloy steels.

The studies were performed on nonmetallic titanium-based inclusions, the presence of which in the weld metal provided inoculation of welding pool with appropriate refractory compounds.

PROCEDURE OF INVESTIGATIONS

The studies were conducted on the specimens of weld metal, produced according to the procedure [5] during arc welding in shielding gas (82 % Ar, 18 % CO_2) using a flux-cored wire with a diameter of 1.6 mm of type "metal core" at the direct current of 200 (±5) A, voltage 30 (±2) V with the input energy of 21 (±2) kJ/cm. To determine the nature of distribution of nonmetallic inclusions in the weld metal to the "cold" part of the welding pool, a flux-cored wire with a diameter of 1.6 mm was introduced, whose core contained a mixture of 10 % of particles of refractory compounds of 0.040–0.200 mm and 90 % of the iron powder of grade PZhV according to DSTU 9849. As inoculants,

Table 1. Chemical composition of weld metal

Weld number	C	Si	Mn	S	P	Cr	Ni	Mo	Cu	Al	Ti
FeTi	0.050	0.290	1.32	0.024	0.014	0.16	2.19	0.27	0.36	0.039	0.019
TiC	0.054	0.263	1.28	0.025	0.011	0.13	2.22	0.26	0.49	0.035	0.009
TiN	0.035	0.317	1.40	0.019	0.009	0.14	2.29	0.26	0.56	0.036	0.011
TiO_2	0.035	0.405	1.24	0.016	0.021	0.11	1.97	0.27	0.68	0.031	0.017

Table 2. Mechanical properties of weld metal

Weld number	Rm	Re	A	Z	*KCV*, J/cm^2 at *T*, °C			
	MPa		%		20	0	–20	–40
FeTi	788	739	11.4	35	60	58	57	52
TiC	716	644	19	63	111	97	85	73
TiN	712	580	5.3	14.7	55	47	40	35
TiO_2	709	636	19	57	85	72	60	50

the following titanium-based compounds were selected: titanium oxide (TiO_2 weld), titanium carbide (TiC weld), titanium nitride (TiN weld). The obtained results were compared with the data of the specimens of the weld metal produced during welding using flux-cored wire, into the core composition of which ferrotitanium (FeTi weld) was introduced.

Metallographic examinations were performed on the cross-sections cut out from welded joints. The structure of the weld metal was examined in an optical microscope, the influence of the distribution of nonmetallic inclusions on the features of metal fracture was determined by the results of fractographic images obtained in the scanning electron microscope JSM-35.

The distribution of inclusions by sizes and plotting the corresponding diagrams was performed directly from the sections. According to the program set in the device, the amount of inclusions in each specimen was calculated by dimensional groups — from the minimum to the maximum size.

The distribution density of nonmetallic inclusions in the structure of weld metal was determined by the procedure given in [6].

The mechanical properties of the weld metal were evaluated according to the results of standard tests in accordance with the requirements of DSTU ISO 6892-1:2019, DSTU EN 10045-1:2006 and DSTU ISO 15792-1:2009.

RESEARCH RESULTS

In Tables 1 and 2, the results of determining the chemical composition and mechanical properties of the metal of the studied welds are shown.

In Figure 1, the histograms of distribution by sizes and a volume fraction of nonmetallic inclusions in the weld metal are shown.

In Figure 2, the specimens of microstructure of the weld metal produced by the methods of optical metallography are shown.

The weld of FeTi metal is characterized by a fine-grained bainitic-martensitic structure according at some of its fragmentation and the formation of intravolume dispersed phases, which should provide a high level of mechanical properties. The bainitic component is represented mainly by the lower (more than 50 %) and upper one. Also, up to 10 % of martensitic component was recorded. In the volume of bainitic grains, the phases of the dispersed sizes of a carbide type are clearly viewed.

In the weld metal of TiC specimens, a bainitic-martensitic structure is formed, which contains mainly upper bainite (about 60 %), the lower bainite amounts to about 25 % and martensite (up to 10 %) at a slight fragmentation of the structure. In the volume of grains of the bainitic structure, the particles of phase precipitates of dispersed sizes of a carbide type are observed with their relatively uniform distribution. For inner microvolumes of the structure, a relatively low distribution density of nonmetallic inclusions is characterized.

In the metal of TiN weld, a heterogeneous bainitic-martensitic structure is formed, which contains about 60 % of upper bainite, lower bainite (about 20 %) and martensite (up to 10 %). In the grains of bainitic structure, the particles of phase precipitates of dispersed sizes of a carbide type at a relatively uniform distribution are observed. On the boundaries of ferritic grains, the presence of chains of phase precipitates is observed, which are the phases of a carbonitride type TiCN, which should lead to a decrease in the level of mechanical properties and a noticeable decrease in the crack resistance of a weld.

TiO_2 weld metal is characterized by a nonuniform bainitic-martensitic structure at its slight fragmentation. The bainitic component is represented mainly by the upper (more than 50 %) and lower (about 30 %) bainite. The content of martensite does not exceed

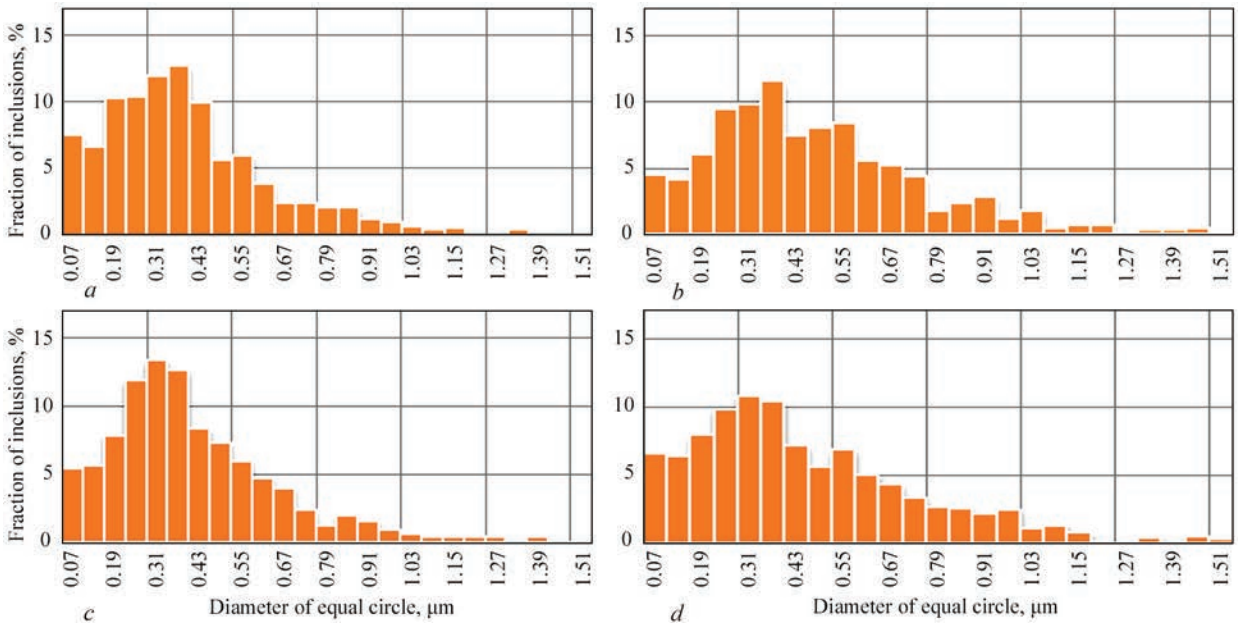

Figure 1. Histograms of distribution by sizes and volume fraction (V) of non-metallic inclusions in the weld metal: *a* — FeTi; *b* — TiC; *c* — TiN; *d* — TiO_2 (*a*, *b* — $V = 0.62$ %; *c* — 0.77; *d* — 0.47)

10 %. In the body of bainitic grains of the structure, the particles of phases of the dispersed sizes of a carbide type, as well as single phase precipitates of a type of titanium oxides of larger sizes are viewed.

ANALYSIS OF RESEARCH RESULTS

The influence of the composition, content and morphology of nonmetallic inclusions on the structure and mechanical properties of low-alloy steels in general and the weld metal in particular traditionally attracts great attention [1–3]. The reduction of mechanical properties, which was obtained on the specimens of TiN weld metal, fully corresponds to the description of the impact of nitrides, which is presented in the mentioned monographs. The attention should be paid to the difference in the distribution of nonmetallic inclusions in the structure of the metal of the studied welds. Metallographic analysis showed that a certain

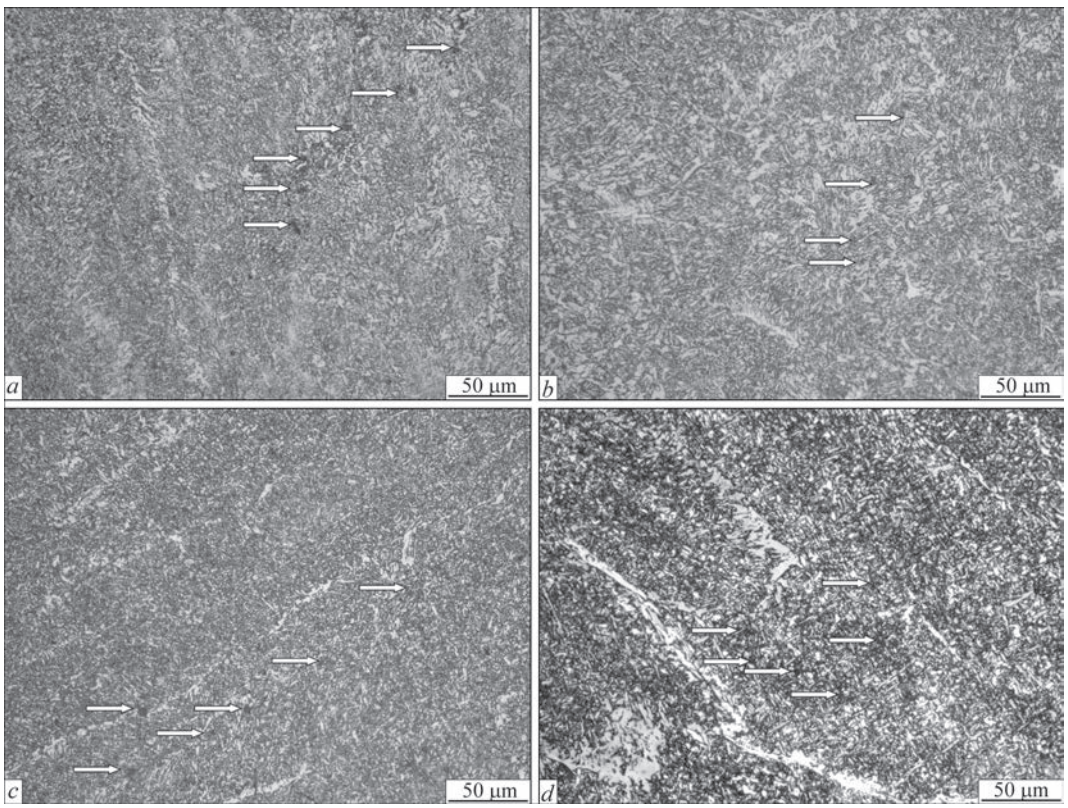

Figure 2. Specimens of microstructure of weld metal: *a* — FeTi; *b* — TiC; *c* — TiN; *d* — TiO_2 (arrows indicate a typical location of nonmetallic inclusions)

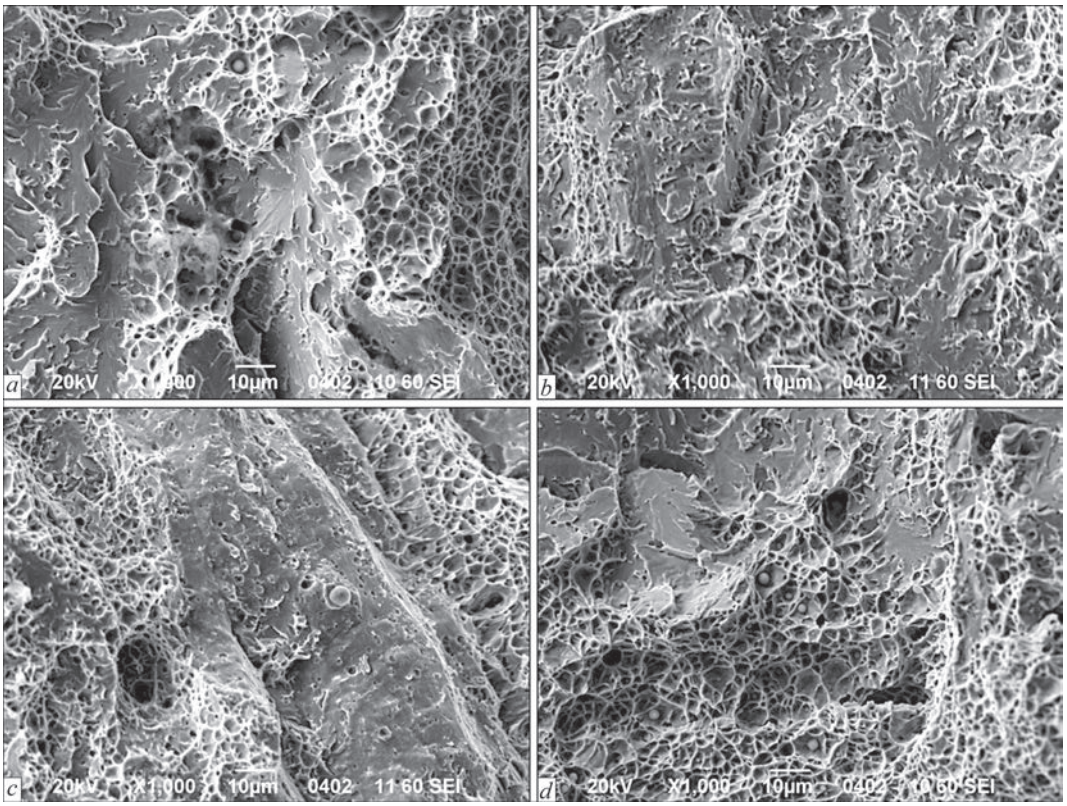

Figure 3. Fractographies of fractures of specimens: *a* — FeTi; *b* — TiC; *c* — TiN; *d* — TiO_2

number of nonmetallic inclusions in FeTi and TiM weld metal are located on the boundaries of ferritic grains, whereas the structure of the welds of TiC and TiO_2 is characterized by the predominant distribution of inclusions in the body of ferritic grains. This feature of the distribution of inclusions is illustrated in Figure 2, where the location of nonmetallic inclusions is marked with arrows.

To find out how such a feature of the distribution of inclusions affects the mechanical properties of the weld metal, fractographic examinations of the specimen fractures were conducted, which were produced during determination of the impact toughness of the weld metal at –40 °C. The results of the examinations are shown in Figure 3.

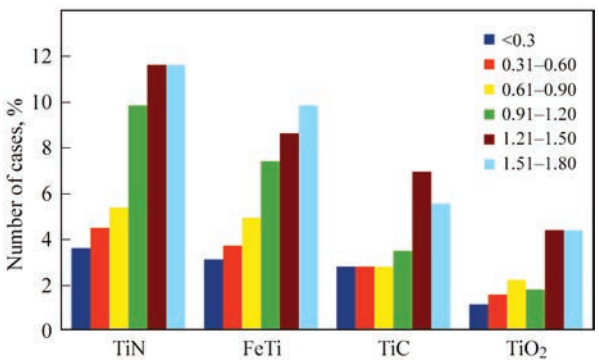

Figure 4. Results of fractal analysis of distribution density of non-metallic inclusions in the weld metal (relative number of cases of distance between two adjacent inclusions (μm) in the designated distance range (μm) is given

The abovementioned data show that dispersed nonmetallic inclusions, located on the boundaries of ferritic grains, serve as sources of initiation of cracks of type of brittle spalling, as is seen in Figure 3, *a*, *c*. In those cases when most inclusions are located in the body of ferritic grains (Figure 3, *b*, *d*), dispersed inclusions are not the centres of brittle crack initiation.

DETERMINING THE NATURE OF DISTRIBUTION OF NONMETALLIC INCLUSIONS

According to modern notions, the influence of nonmetallic inclusions on the tendency of metal to brittle fracture is associated with the stress fields initiated around them. Single-phase inclusions, whose thermal expansion coefficient is lower than in the metal matrix, contribute to the formation of a higher level of stresses compared to inclusions consisting of several layers of different composition. In the case when inclusions are located in the metal matrix at some distance from each other, which exceeds the action radius induced by the stresses, their effect on the tendency of metal to brittle fracture is lower compared to the situation when inclusions are located much closer. Based on these notions, the distance between inclusions is one of the important characteristics of the distribution of nonmetallic inclusions in the weld metal.

The methods of computer processing of optical images of the polished surface of the sections of the examined welds make it possible to obtain digital informa-

tion both of the total content of nonmetallic inclusions in the metal as well as of their distribution by sizes (see Figure 1). These data give a notion of the generalized characteristics of inclusions, but do not allow revealing the features of their distribution in the structure of the weld metal. Information on the total content of nonmetallic inclusions and the nature of their distribution by size does not give grounds to find out the factors that cause the difference between the toughness and ductility values of the weld metal. In order to solve this problem, it is advisable to involve the methods of fractal analysis of nonmetallic inclusions.

In [6], a method of fractal analysis of structural components of the metal was proposed, which allows determining the features of density (distance between adjacent inclusions) of the distribution of nonmetallic inclusions. The impact of inclusions on the tendency to spalling formation in the surrounding metal matrix depends on the level of stresses occurring at the interphase boundary and on the distance to adjacent inclusions. Based on the abovementioned reasons, the works on fractal analysis of the specimens of weld metal were performed in order to determine the nature of their distribution relative to the distance to the nearest adjacent inclusions. The results of the research works are shown in Figure 4.

As is seen from the abovementioned data, the highest distribution density of inclusions is in FeTi and TiN welds. Namely these welds are characterized by a structure in which an increased presence of inclusions on the boundaries of ferritic grains (Figure 2) is noted and this is accompanied by a decrease in the values of toughness and ductility (Table 2). It should be noted that the higher distribution density of inclusions in the metal of TiN weld is accompanied by a lower level of toughness and ductility values.

In the metal of TiC and TiO_2 welds, a number of cases with an increased distribution density of inclusions is noticeably lower, which can serve as an explanation of a higher level of relevant values.

The obtained results indicate that the combination of such two factors as the presence of nonmetallic inclusions on the boundaries of grains and an increased density of their distribution leads to a decrease in the toughness and ductility values of weld metal of high-strength low-alloy steels.

CONCLUSIONS

A complex of works was carried out on establishing the nature of the distribution of nonmetallic inclusions in the metal structure of low-alloy welds. As a result of metallographic examinations, the indicators of volumetric content of inclusions in the structure and their distribution by sizes were established. The feasibility of using such an additional indicator as the distribution density of inclusions when evaluating their impact on the mechanical properties of the weld metal is shown. The use of fractal analysis to find out the features of the influence of nonmetallic inclusions on the mechanical indicators of the weld metal of high-strength low-alloy steels, taking into account the distribution density of inclusions.

REFERENCES

1. Liu, S., Olson, D.L. (1987) The influence of inclusion chemical composition on weld metal microstructure. *J. Mater. Eng.*, **9**, 237–251.
2. Lienert, T.J., Babu, S.S., Siewert, T.A. (2011) *Solid-state transformations in weldments*. ASM Handbook®. Welding Fundamentals and Processes. Ed. by V.L. Acoff, 6A, ASM International®, Materials Park, 133–135.
3. Bhadeshia, H.K.D.H., Honeycombe, R.W.K. (2006) *Steels: Microstructure and properties*. 3rd Ed., Elsevier Ltd.
4. Kang, Y. et al. (2014) Influence of Ti on nonmetallic inclusion formation and acicular ferrite nucleation in high strength low alloy steel weld metals. *Metals and Mater. Int.*, 20(**1**), 119–127.
5. Holovko, V.V., Yermolenko, D.Yu., Stepanyuk, S.M. et al. (2020) Influence of introduction of refractory particles into welding pool on structure and properties of weld metal. *The Paton Welding J.*, **8**, 8–14. DOI: https://doi.org/10.37434/tpwj2020.08.01
6. Shtofel, O., Korolenko, D., Holovko, V. (2023) Computerization of calculation process of nonmetallic inclusion parameters in metal. In: *Proc. of the VII Int. Sci. and Pract. Conf. Stockholm, Sweden,* 423–434. DOI: 10.46299/ISG.2023.1.7

ORCID

V.V. Holovko: 0000-0002-2117-0864,
O.O. Shtofel: 0000-0003-0965-6340

CONFLICT OF INTEREST

The Authors declare no conflict of interest

CORRESPONDING AUTHOR

V.V. Holovko
E.O. Paton Electric Welding Institute of the NASU
11 Kazymyr Malevych Str., 03150, Kyiv, Ukraine.
E-mail: v_golovko@ukr.net

SUGGESTED CITATION

V.V. Holovko, O.O. Shtofel, D.Yu. Korolenko (2023) Influence of the nature of distribution of nonmetallic inclusions on the mechanical properties of weld metal of low-alloy steels. *The Paton Welding J.*, **3**, 3–7.

JOURNAL HOME PAGE

https://patonpublishinghouse.com/eng/journals/tpwj

Received: 06.03.2023
Accepted: 24.04.2023

DOI: https://doi.org/10.37434/tpwj2023.03.02

MATHEMATICAL MODELING OF RESIDUAL STRESSES IN A COMPOSITE WELDED JOINT OF THE COLLECTOR ADAPTER SLEEVE AND THE BRANCH PIPE OF PGV-440 STEAM GENERATOR

A.A. Makarenko[1], **O.V. Makhnenko**[2]

[1]STC of the E.O. Paton Electric Welding Institute of NASU
11 Kazymyr Malevych Str., 03150, Kyiv, Ukraine
[2]E.O. Paton Electric Welding Institute of the NASU
11 Kazymyr Malevych Str., 03150, Kyiv, Ukraine

ABSTRACT

Composite welded joints of dissimilar materials, usually steels of ferritic-pearlitic (bainitic) and austenitic grades, were used in elements of equipment and pipelines of operating nuclear power plants (NPP). The considerable difference in chemical composition of base material and welding consumables leads to chemical and structural heterogeneity of metal in the joint zone, and the difference in the coefficients of thermal expansion of the materials during welding and postweld heat treatment results in formation of high unrelaxed residual stresses, which significantly influence the strength, fatigue life and corrosion resistance of equipment elements. Considerable difficulties of experimental measurement of residual stresses make it complicated to take them into account at determination of the service life of nuclear power plant equipment elements. Damage of the Dn-1100 welded joint in the welded assembly of the coolant collector adapter sleeve from 08Kh18N10T stainless steel and the branch pipe of the steam generator body from 22K steel is one of the problems in safe operation of WWER-440 nuclear power units. Systematized information on the nature and causes for development of this damage are absent. In this connection, the methods of mathematical modeling were used to perform analysis of the microstructural phase composition and residual stresses, arising in this joint in welding, and of their influence on the service life of the welded assembly. Analysis of the results of mathematical modeling of the thermal processes, microstructural phase transformations and stress-strain state (SSS) in the composite welded joint showed that hardening structures in the HAZ of branch pipe metal (St22K) and lowering of the material crack resistance characteristics can be found at violation of surfacing and welding technology during steam generator manufacture, namely non-compliance with the conditions of preheating and concurrent heating ($T \geq 200$ °C). Rather high residual tensile stresses were determined on the composite joint inner surface, which is in contact with the coolant corrosive medium in operation, as well as in the zone of contact (fusion) of the material of branch pipe pearlitic steel with austenitic metal of the weld, where there is a high probability of discontinuity defect formation in welding. It may have a negative influence on the strength and structural integrity of the welded assembly of branch pipe of steam generator (SG) at further long-term service.

KEYWORDS: composite welded joint, PGV-440 steam generator, heat-affected zone, microstructural phase transformations, residual stresses, mathematical modeling

INTRODUCTION

Evaluation of strength, integrity and serviceability of welded joint components, which requires data on residual stresses, is one of the most important issues of safe operation and extension of service life of the equipment of nuclear power plants (NPP) of Ukraine. So-called composite welded joints (CWJ) of dissimilar materials, usually of steels of ferritic-pearlitic and austenitic grades, were quite often used in the elements of equipment and pipelines of operating NPP. A feature of the composite welded joints consists in that the difference in the chemical composition of the base metal and welding consumables may lead to considerable diffusion of chemical elements in the joint zone during welding heating, which causes chemical and structural heterogeneity of CWJ metal [1, 2]. In addition, considerable difference in the coefficients of thermal expansion of the component materials may give rise to significant unrelaxed residual stresses during welding and postweld heat treatment [3, 4]. Structural heterogeneity of CWJ metal and unrelaxed residual stresses have a noticeable influence on the strength, fatigue life and corrosion resistance of the equipment elements [5]. Considerable difficulties in experimental measurement of unrelaxed residual stresses make it more complicated to allow for them at determination of the service life of nuclear power plant equipment elements.

Starting from 2007, one of the problems for the operating nuclear power units of water-water energetic reactor 440 (WWER-440) is damage of CWJ Dn-1100 of the welded assembly of the coolant collectors from 08Kh18N10T stainless steel and branch pipe of the body of steam generators (SG) from 22K steel. The ring discontinuities (cracks) were detected in the zone of fusion of pearlitic and austenitic metals in power units of Armenian NPP, Dukovani NPP

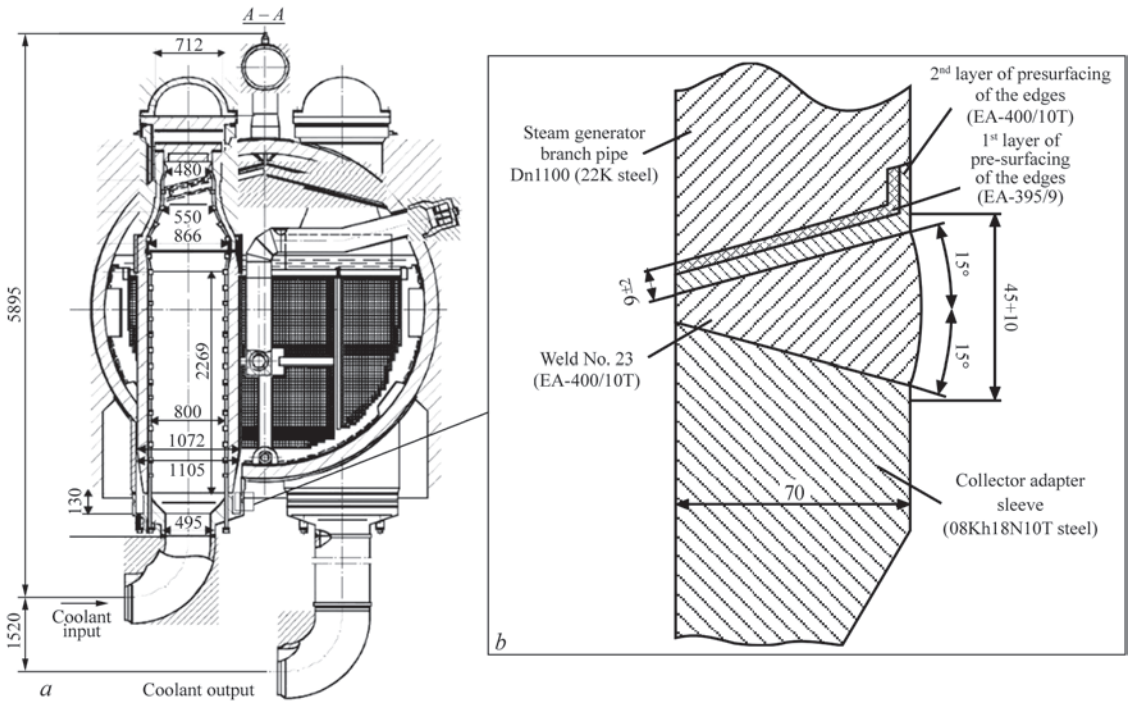

Figure 1. Design of PGV-440 with connected collectors (*a*) and schematic of welded joint of collector adapter sleeve and steam generator branch pipe (*b*)

(Czechia) and some others. Investigations of the nature and cause for development of a high damage level were conducted [13, 14]. Systematized information on analysis of residual stresses developing in this joint and their influence on welded assembly service life are absent.

DESIGN AND TECHNOLOGY OF MAKING THE CWJ OF SG BODY WITH THE COLLECTOR

Figure 1 shows the design of a welded joint in the welded assembly of the collector and branch pipe Dn-1100 of PGV-400 steam generator, which includes the following [6–8, 14]:

1. Steam generator branch pipe Dn-1100 from 22K steel with preliminary two-layer surfacing of the edge: first layer is EA-395/9 (Sv-10Kh16N25AM6), second layer is EA-400/10T (Sv-04Kh19N11MZ). Surfacing is performed with preheating to 100 °C with subsequent heat treatment by the mode of residual tempering at 640 + 20 °C with 9 h soaking.

2. Adapter sleeve from 08Kh18N10T steel, which has a tapered transition on external diameter, with variation of sleeve wall thickness from 70 mm (for welding to steam generator body branch pipe) to 35 mm (for welding the adapter sleeve to circulation pipeline).

3. Weld joining the adapter sleeve to steam generator branch pipe from 22K steel with presurfaced edge, which is made by manual electric-arc welding by EA-400/10T electrodes without preheating. No tempering to relieve the residual stresses is performed.

DAMAGEABILITY OF COMPOSITE WELDED JOINTS OF WWER-440 STEAM GENERATORS

The first damage in composite welded joints of WWER-440 steam generators was found at NPP [13] in 2007. In power unit No. 3 at operational control of metal of ZPG-1 seam generator inadmissible reflectors were detected by UT technique in welded joint No. 23kh (in SG, manufactured later, including those in Rivne NPP, welded joints No. 23kh and No. 23d are designated No. 76 and No. 77, respectively). Mechanical cutting out of templates from welded joint No. 23Kh was performed. Visual examination of the template showed a cracklike discontinuity, filled with corrosion products, which runs through the zone of fusion of pearlitic steel 22K with a deposit on the edge of weld No. 23Kh. The surface of the template from the side of steel 22K, which contacts the medium of the 2nd circuit, is affected by multiple general and pitting corrosion of up to ~3 mm depth.

The macrostructure of welded joint samples is given in Figure 2. Main cracks were detected in the macrosections, which have the same location and direction: from the weld root upwards through the fusion zone. In the sample, the transition deposit made with EA 395 electrode, is of nonuniform thickness, and a considerable part of the welded joint is absent (Figure 2, *a*).

Analysis of the results of fractographic studies on welded joint samples led to the following conclusions [14]:

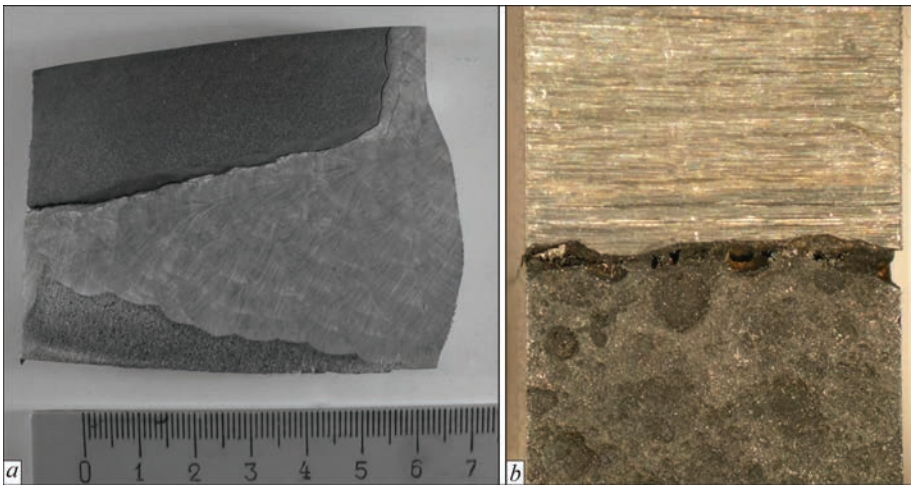

Figure 2. Macrostructure of the welded joint sample: *a* — cross-sectional view; *b* — view of the inner surface contacting the working medium of the 2nd circuit [14]

● main crack growth is staged and it is accompanied by intensive oxidation of its surface;

● the crack initiates in the zone of the fusion line of dissimilar materials of the composite welded joint, which is accompanied by intensive dissolution of base metal with development of a local corrosion center.

Thus, destruction is mainly of a corrosion-mechanical nature, and it can be indentified as stress corrosion cracking, due to a certain nature and level of the stress-strain state and simultaneous influence of the corrosive medium in the collector "pocket".

Moreover, in individual microzones of the sample metallographic analysis clearly established the presence of a changed layer, adjacent to the base metal [14]. This metal layer is the consequence of strong mixing of the metal of austenitic weld and carbon steel; its chemical composition has lower Cr and Ni content, which corresponds to the martensitic region of Scheffler phase diagram. The results of measurement of metal microhardness of the changed layer and of austenitic weld metal are indicative of the higher hardness of this layer, which is characteristic for martensite. Interlayers of acicular martensitic structure were revealed in the higher hardness layer, which could initiate cracking both right after manufacture and in service.

OBJECTIVE OF THE STUDY

Within the scope of solving the problems of safe operation of WWER-440 nuclear power units, mathematical modeling was performed of thermal processes, microstructural phase transformations and residual stresses in welding of composite welded joint Dn-1100 of the coolant collector adapter sleeve and branch pipe of the body of PGV-400 steam generator for further analysis of the nature and causes for damage, developing in this joint and their influence on the welded assembly service life.

DEVELOPMENT OF THE MATHEMATICAL MODEL OF SSS IN CWJ WELDING

Calculation-based prediction of residual stresses in the zone of CWJ of collector adapter sleeve and steam generator branch pipe Dn-1100 was performed using the methods of elasto-viscous-plastic analysis of the thermodeformational processes during surfacing of the steam generator branch pipe edge, intermediate heat treatment and filling the welded joint groove by multipass welding. Although it is believed that low-carbon pearlitic steel 22K is not prone to hardening structure formation under the impact of thermal cycles of welding, nonetheless modeling of microstructural phase transformations was conducted for a more detailed analysis of this matter. Modeling of the creep processes during intermediate heat treatment was performed after the edge surfacing, in order to determine the residual stress relaxation.

Taking into account the partially symmetric design of the welded assembly and the possibility of effective application of the assumption of fast-moving source of welding heat for modeling the temperature distributions and SSS of circumferential welded joints [9], a 2D finite-element model of the assembly of welded joint of the adapter sleeve and steam generator branch pipe Dn-1100 was plotted with the assumption of axial symmetry of the latter (Figure 1). The scheme of the model and boundary conditions of the welded assembly, and finite-element grid in the welded joint zone are shown in Figures 3–4.

The temperature problem was solved under the assumption of a fast-moving heat source, which allowed using a 2D finite-element model in the cross-section of the welded joint (Figure 2). Modeling of temperature distributions when making the welding passes was performed with application of the equation of

nonstationary heat conductivity, which includes allowing for a bulk welding heat source $W(x, y, t)$ [9]

$$\frac{\partial}{\partial x}\left(\lambda\frac{\partial T}{\partial x}\right)+\frac{\partial}{\partial y}\left(\lambda\frac{\partial T}{\partial y}\right)+ +W(x,y,t)=c\rho\frac{\partial T}{\partial t}, \quad (1)$$

where ρ is the material density; c is the specific heat conductivity; λ is the coefficient of heat conductivity; T is the material temperature.

$$W(x,y,t)=\frac{6Q}{ab\sqrt{\pi}}\times \times\exp\left(\frac{-3(x-x_0)^2}{a^2}-\frac{-3(y-y_0)^2}{b^2}\right), \quad (2)$$

where Q is the effective power of the welding heat source; x_0, y_0 are the coordinates of heat source center and a, b are the respective dimensions (width and depth) of the effective heating zone in x, y directions. The time of heating of the metal in each welding pass in the welded joint cross-section depends on welding speed v_w and size of effective heating zone a, in the first approximation, it may be equal to $t_w = a/v_w$.

The welding heat source parameters were selected so that the metal temperature in the weld did not exceed that of melting, and the time between the passes was sufficient for metal cooling to concurrent heating temperature.

Boundary conditions on the surfaces of welded joint elements, taking into account the convective heat exchange with the environment, were assigned in the following form:

$$q=-h(T_{out}-T), \quad (3)$$

where T_{out} is the ambient temperature; q is the heat flux; h is the coefficient of heat transfer from the surface at convective heat exchange with the environment.

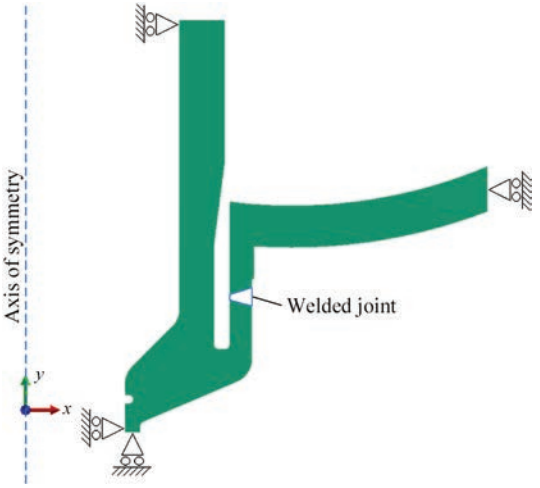

Figure 3. Scheme of 2D model (rotationally-symmetrical relative to axis *Y*) of welded joint assembly and boundary conditions

Nonstationary concentrated heating induces high temperature stresses, as well as plastic strains in the welded joint materials. Taking into account the "plane strain" hypothesis, solution of the problem on determination of the distribution of spatial components of stresses and strains was derived using a 2D model of the welded joint cross-section in the elastoplastic definition, i.e. this strain tensor can be presented as a sum of tensors:

$$\varepsilon_{ij}=\varepsilon_{ij}^e+\varepsilon_{ij}^p, \quad (i,j=x,y,z), \quad (4)$$

where ε_{ij}^e is the elastic strain tensor; ε_{ij}^p is the plastic strain tensor. The components of tensors of stresses σ_{ij} and elastic strains ε_{ij}^e are related to each other by the following Hooke's law:

$$\varepsilon_{ij}^e=\frac{\sigma_{ij}-\delta_{ij}\sigma}{2G}+\delta_{ij}(K\sigma+\varphi), \quad (5)$$

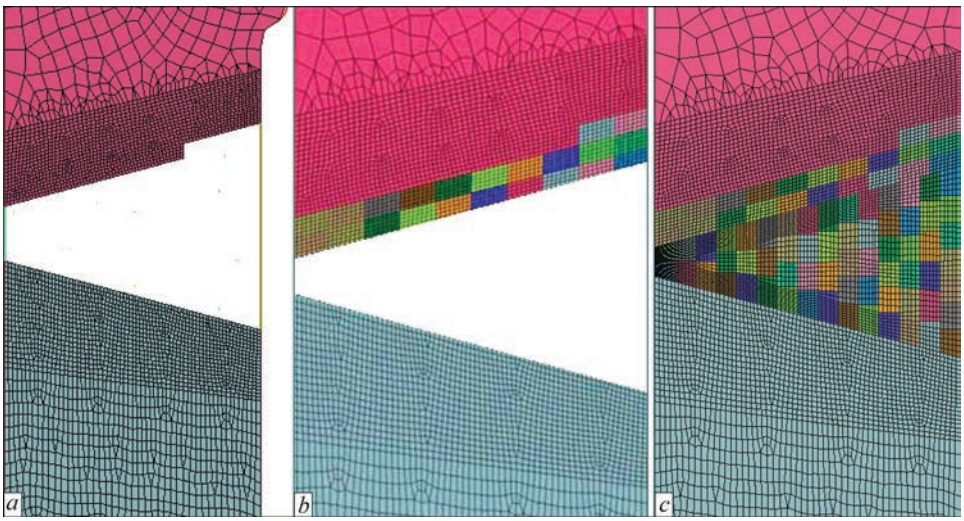

Figure 4. Finite-element grid in welded joint zone: *a* — before surfacing and welding; *b* — after edge surfacing; *c* — after welding

where δ_{ij} is the unit tensor ($\delta_{ij} = 0$, if $i \neq j$, $\delta_{ij} = 1$, if $i = j$); $\sigma = \frac{1}{3}(\sigma_{xx} + \sigma_{yy} + \sigma_{zz})$; $G = \frac{E}{2(1+\nu)}$ is the shear modulus; $K = \frac{1-2\nu}{E}$ is the bulk compression modulus; E is the Young's modulus; ν is the Poisson's ratio; φ is the function of free relative elongations (bulk changes), caused by the temperature change and microstructural phase changes. In a simple case, when no structural transformations take place:

$$\varphi = \alpha(T - T_0), \tag{6}$$

where α is the coefficient of relative temperature elongation of the material.

When welding steels, sensitive to the thermal cycle of welding, microstructural transformations with noticeable bulk changes can take place in the HAZ in K22 pearlitic steel for this welded joint. Allowing for them influences the kinetics of distribution of welding stresses and strains. The total effect of bulk changes from temperature T_0 up to $T(t)$ is found by [9]:

$$3\varphi = \frac{\sum V_j(T,t)\gamma_j(T) - \sum V_j(T_0)\gamma_j(T_0)}{\sum V_j(T_0)\gamma_j(T_0)}, \quad (j = m, b, fp, a), \tag{7}$$

where $\gamma_j(T)$ is the volume of a unit of mass of jth phase at temperature T, $V_j(T)$ is the fraction (in fractions of a unit) of jth phase at temperature T, m, b, fp, a indices are martensite, bainite, ferrite-pearlite and austenite, respectively.

Values $V_j(T)$ for low-alloyed steels can be determined, depending on carbon content C, % [15]:

$$\begin{aligned}
&\gamma_m(T) = 0.12282 + 8.56\cdot10^{-6}T + \\
&+ 2.15\cdot10^{-6}\,\text{C}, (\text{cm}^3/\text{g}); \\
&\gamma_a(T) = 0.12708 + 4.448\cdot10^{-6}T + \\
&+ 2.79\cdot10^{-6}\,\text{C}, (\text{cm}^3/\text{g}); \\
&\gamma_{b,fp}(T) = 0.12708 + 5.528\cdot10^{-6}T, (\text{cm}^3/\text{g});
\end{aligned} \tag{8}$$

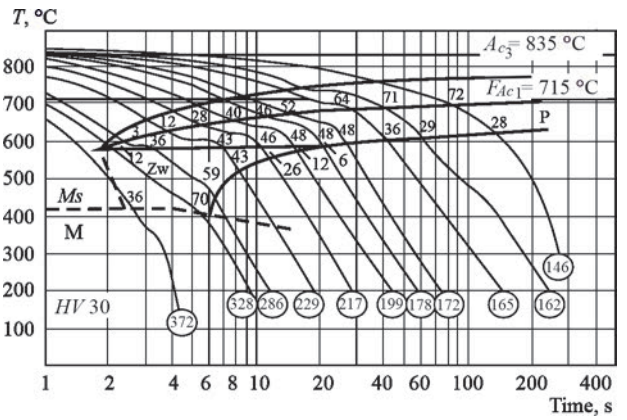

Figure 5. Thermokinetic diagram of austenite decomposition for melting steel close to 22K steel by its chemical composition (C 019 %, Si 0.294 % Mn 0.67 %, S 0.011%, P 0.074 %) [18]

Results of calculation of the mass fraction of each phase $V_j(T)$ in the final microstructure, depend on the cooling rate in the characteristic temperature range (rate of cooling from the temperature of 800 to 500 °C).

Kinetics of the changes of $V_j(T)$ value in the temperature range from $T_s^{(j)}$ — start of jth phase appearance up to $T_e^{(j)}$ — end of jth phase appearance at austenite decomposition, is defined from the following relationships:

$$\begin{aligned}
V_j(T) &= V_j^{\max}\left[1 - \exp\left(a_j \frac{T_{sj} - T}{T_{sj} - T_{ej}}\right)\right] \\
a_j &= -2,7 (j = m, fp, b); \\
V_a(T) &= 1 - \sum_{m,fp,b} V_j(T),
\end{aligned} \tag{9}$$

where $V_a(T)$ is the residual austenite content at temperature T.

Values of temperatures of the start $T_s^{(j)}$ and end $T_e^{(j)}$ of jth phase transformations, as well as its mass fraction in the final microstructure after cooling $V_j^{\max}$ for 22K steel were determined with application of parametric (regression) equations for low-alloyed steels, depending on their chemical composition and characteristic cooling time $\Delta t_{8/5}$, s (time of cooling from the temperature of 800 to 500 °C) [15, 16]:

$$\begin{aligned}
V_m^{\max} &= 0,5\left[1 - erf\frac{\ln \Delta t_{8/5} - \ln \Delta t_m^{50}}{\ln S_m}\right]; \\
V_{fp}^{\max} &= 0,5\left[1 + erf\frac{\ln \Delta t_{8/5} - \ln \Delta t_{fp}^{50}}{\ln S_{fp}}\right]; \\
V_b^{\max} &= 1 - V_m^{\max} - V_{fp}^{\max}.
\end{aligned} \tag{10}$$

Microstructural phase transformations were not modeled in 08Kh18N10T austenitic steel and EA-395/9 (Sv-10Kh16N25AM6), EA-400/10T (Sv-04Kh19N11M3) welding consumables.

A thermokinetic diagram of austenite decomposition (Figure 5) for producing steel [18], close by its composition (C 019 %, Si 0.294 %, Mn 0.67 %, S 0.011 %, P 0.074 %) was considered for analysis of the probable microstructural phase composition in the zone of edge surfacing and welding the branch pipe from 22K steel. One can see that at high cooling rates (30 % °C/s and higher) the branch pipe metal during edge surfacing by an austenitic material, or at subsequent multipass welding of the circumferential butt joint, a pearlitic-bainitic-martensitic structure forms with the possible maximum content of martensite of approximately up to 30 %.

Plastic strains are related to the stressed state by an equation of the theory of plastic nonisothermal flow, associated with von Mises yield criterion:

$$d\varepsilon_{ij}^{p} = d\lambda(\sigma_{ij} - \delta_{ij}\sigma), (i, j = x, y, z), \quad (11)$$

where $\partial\varepsilon_{ij}^{p}$ is the ε_{ij}^{p} tensor increment at the given moment of time t, due to the deformation history; stresses σ_{ij} and temperature T; $d\lambda$ is the scalar function, which is determined by flow conditions in the following form:

$$\begin{aligned} &d\lambda = 0, \text{ if } f = \sigma_i^2 - \sigma_y^2(T) < 0, \\ &\text{або } f = 0 \text{ at } df < 0; \\ &d\lambda > 0, \text{ if } f = 0 \text{ and } df > 0; \\ &f > 0 \text{ state is inadmissible,} \end{aligned} \quad (12)$$

where σ_i is the stress intensity.

$$\sigma_i = \frac{1}{\sqrt{2}} \times \sqrt{\left(\sigma_{xx} - \sigma_{yy}\right)^2 + \left(\sigma_{xx} - \sigma_{zz}\right)^2 + \left(\sigma_{yy} - \sigma_{zz}\right)^2 + 6\left(\sigma_{xy}^2 + \sigma_{xz}^2 + \sigma_{yz}^2\right)},$$

$\sigma_y(T)$ is the material yield limit at temperature T.

In order to obtain results on the components of residual stresses σ_{ij} and strains ε_{ij}, it is necessary to consider the process of development of elastoplastic strains in time, beginning from a certain initial state. The method of sequential tracking is traditionally used for this purpose, when for moment of time t the solution is sought, if complete solution for moment $(t - \Delta t)$ is known, where Δt is the step of tracking the development of elastoplastic strains, within which one can approximately assume that development proceeds by a rather simple loading path. In this case, the connection between the final increment of strain tensor $\Delta\varepsilon_{ij}$ and stress tensor σ_{ij} in keeping with [9], can be written in the following form:

$$\Delta\varepsilon_{ij} = \psi(\sigma_{ij} - \delta_{ij}\sigma) + \delta_{ij}(K\sigma) - b_{ij}, \quad (13)$$

where ψ is the function of material state in point (x, y, z) at moment t.

$$\begin{aligned} &\psi = \frac{1}{2G}, \text{ if } f < 0, \ \psi > \frac{1}{2G}, \text{ if } f > 0, \\ &\text{state } f > 0 \text{ is inadmissible,} \end{aligned} \quad (14)$$

b_{ij} is the tensor function of additional strains, which is determined by $\Delta\varphi$ increase and known results of the previous tacking stage:

$$b_{ij} = \left[\frac{\sigma_{ij} - \delta_{ij}\sigma}{2G} + \delta_{ij}(K\sigma)\right]_{t-\Delta t} + \delta_{ij}\Delta\varphi \quad (i, j = x, y, z). \quad (15)$$

Yield conditions in the form of (11) include significant physical nonlinearity in material state function ψ. Iteration processes are usually used for realization of this type of physical nonlinearity. As a result, in each iteration the physically nonlinear problem becomes a linear one of the type of a problem of the theory of elasticity with a variable shear modulus, which is equal to $1/2\psi$, and additional strains b_{ij}. Numerical methods are used for realization of such a linearized problem.

PHYSICOMECHANICAL PROPERTIES OF MATERIALS

Temperature fields at welding heating were calculated using the values of the coefficient of heat conductivity λ and bulk heat capacity ($c\rho$) of welded joint materials, depending on temperature (Figure 6, *a*, *b*). The deformation processes were calculated using the values of the temperature coefficient of linear expansion α, yield limit σ_y, modulus of elasticity E and Poisson's ratio ν of the materials, also depending on temperature (Figure 6, *c–f*). Dependencies of thermophysical and mechanical properties of the materials on temperature were derived according to reference books [16, 17], as well as by calculation by the chemical composition [19].

Most of the properties of 22K pearlitic steel (Figure 6, *a–d*) differ essentially from those of austenitic high-temperature steel 08Kh18N10T and EA-395/9 (Sv-10Kh16N25AM6), and EA-400/10T (Sv-04Kh19N11M3) welding consumables. Only the Young's modulus and Poisson's ratio are close by their values in the entire temperature range of heating (Figure 6 *e*, *f*).

DEVELOPMENT OF A MATHEMATICAL MODEL OF RESIDUAL STRESS RELAXATION AND REDISTRIBUTION DURING HEAT TREATMENT

In keeping with the data of certificates (PTD) [7, 8], when making composite welded joints of steam generator branch pipe Dn-1100 with the collector adapter sleeve after preliminary surfacing of the edge of the branch pipe from 22K steel by two layers of austenitic material, heat treatment was performed in the high-temperature tempering mode at 640 + 20 °C for 9 h. After making the welding passes of the joint of the adapter sleeve and the steam generator branch pipe with the preliminarily surfaced edge, no tempering was performed to relieve the residual stresses.

After performance of mathematical modeling of the heat treatment process after preliminary surfacing of the branch pipe edge, determination of the nonstationary temperature field was realized due to convective heat exchange on the surfaces at a gradual heating of the environment, soaking and further rather slow cooling. The nonstationary boundary conditions corresponded to uniform increase of ambient tempera-

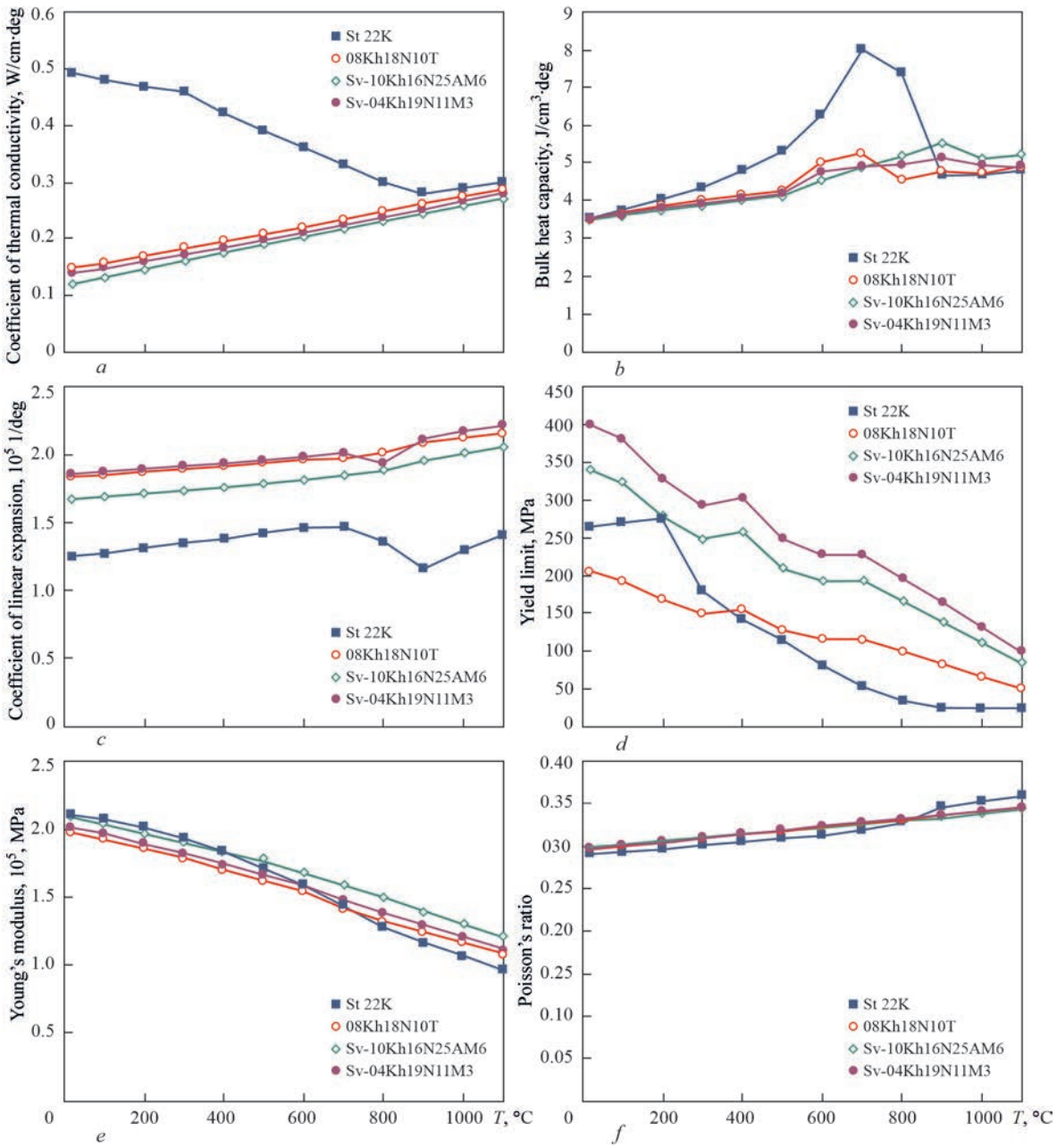

Figure 6. Mechanical and thermophysical properties of base materials: 22K steel, 08Kh18N10T steel and EA-395/9 (Sv-10Kh16N25AM6), EA-400/10T (Sv-04Kh19N11M3) welding consumables, depending on temperature [16–18]: *a* — coefficient of thermal conductivity; *b* — bulk heat capacity; *c* — coefficient of linear temperature expansion; *d* — yield limit; *e* — Young's modulus; *f* — Poisson's ratio

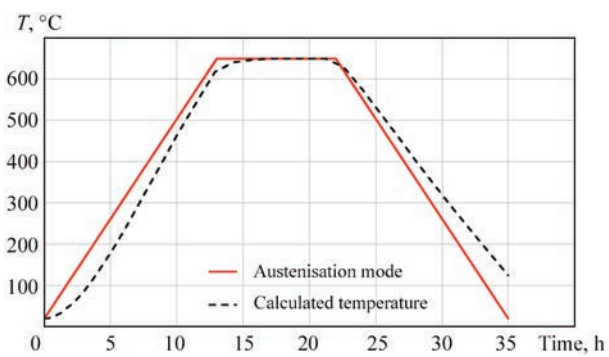

Figure 7. Graph of the change of the material temperature of branch pipe with surfaced edges during heat treatment

ture T_{amb} at the rate of 30 °C/h during heating up to 650 °C, soaking for 9 h and lowering to 20 °C at the rate of 30 °C/h at cooling (Figure 7).

The initial and boundary conditions of the boundary problem of determination of temperature distributions in the branch pipe with surfaced edges at heat treatment were as follows:

$$\text{at } t = 0,\ T_{out}(0) = 20\ ^\circ\text{C},\ T(0) = 20\ ^\circ\text{C},$$
$$q = -h(T_{out}(t) - T),$$
$$(T_{out}(t) = 30\ ^\circ\text{C/h}\cdot t,\ T_{out}^{\max} = 650\ ^\circ\text{C}.$$

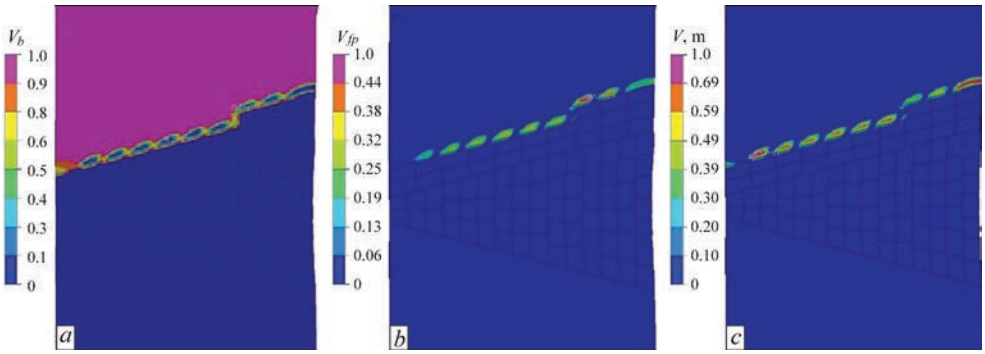

Figure 8. Results of modeling the residual microstructural composition in CWJ zone at $T_{preheating}$ = 100 °C; *a* — bainite; *b* — ferrite-pearlite; *c* — martensite

The coefficient of heat transfer from the branch pipe surface at convective heat exchange with the environment in the furnace and in air was taken equal to value h = 30 W/m^2 under the conditions of natural convection and heating and cooling constant in the entire range of heating and cooling temperatures. Radiant heat exchange in the developed model was not modeled separately, and its contribution was taken into account in a certain increase of the value of heat transfer coefficient.

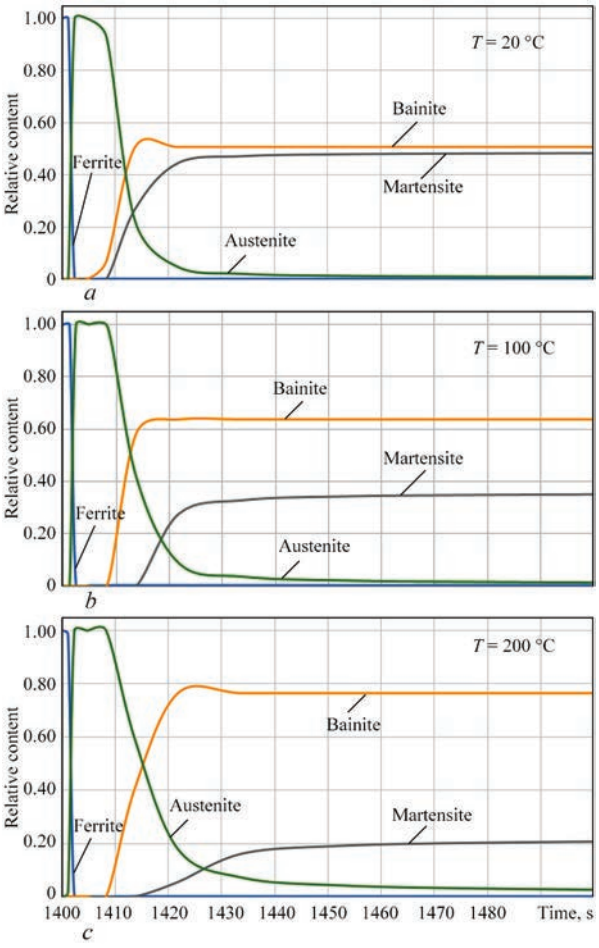

Figure 9. Kinetics of microstructural phase transformations in the characteristic point of the HAZ of SG branch pipe base material (22K steel) for different preheating temperatures: *a* — without preheating; *b* — $T_{preheating}$ = 100 °C; *c* – $T_{preheating}$ = 200 °C

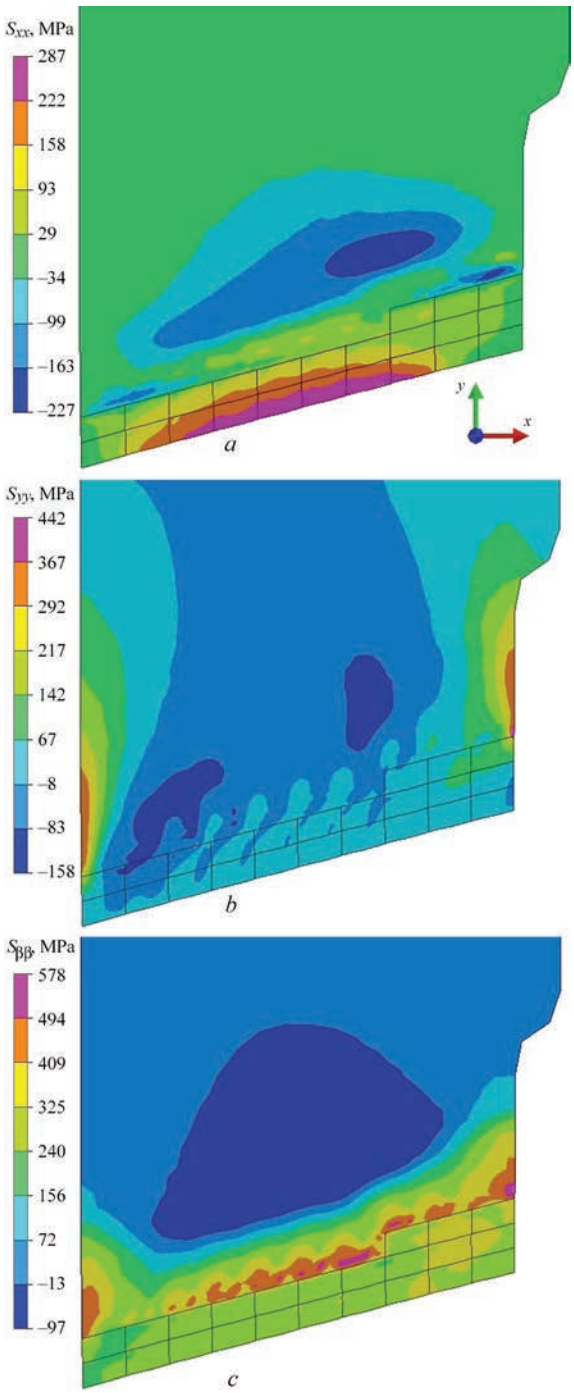

Figure 10. Residual stresses after surfacing the of SG branch pipe edges: *a* — radial σ_{xx}; *b* — axial σ_{yy} ; *c* — circumferential $\sigma_{\beta\beta}$

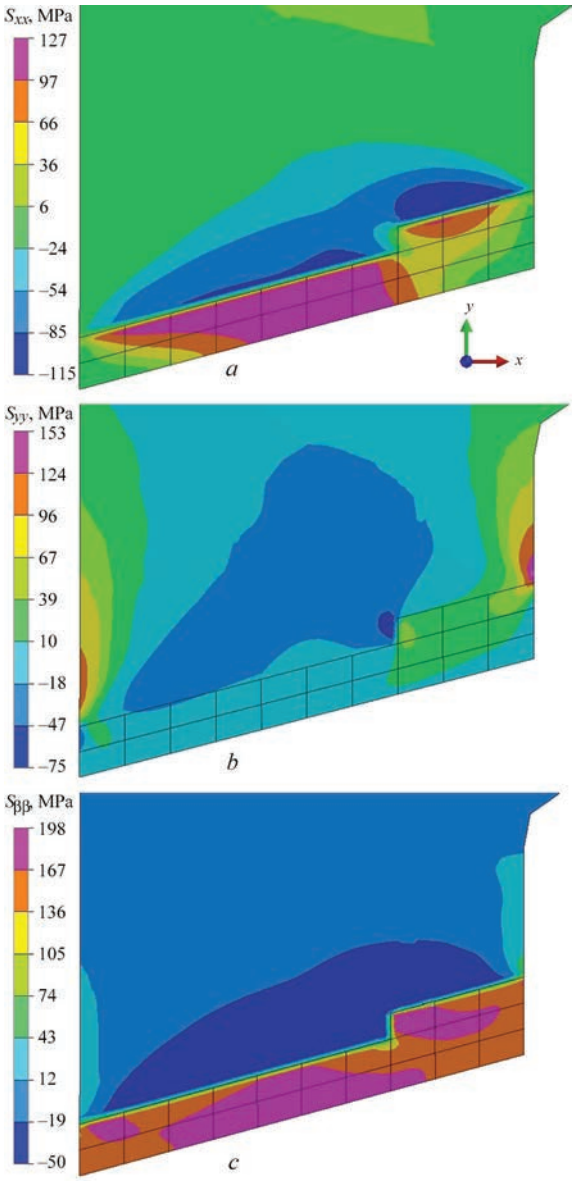

Figure 11. Residual stresses after heat treatment of SG branch pipe edge (T = 650 °C, $T_{soaking}$ = 9 h): *a* — radial σ_{xx}; *b* — axial σ_{yy}; *c* — circumferential $\sigma_{\beta\beta}$

The long-term process of heating up to the soaking temperature of 650 °C causes the processes of high-temperature creep in the material of the branch pipe and the austenitic deposit, which leads to relaxation and redistribution of residual stresses in the surfacing zone.

In the developed model the problem of determination of SSS at heat treatment was solved in the visco-elastoplastic definition [9]:

$$\varepsilon_{ij} = \varepsilon_{ij}^{e} + \varepsilon_{ij}^{p} + \varepsilon_{ij}^{cr} \ (i, j = x, y, z), \tag{16}$$

where the creep strain rate was determined by Bailey–Norton law [11]:

$$\dot{\varepsilon}_{ij}^{cr} = A\sigma_{eq}^{n}. \tag{17}$$

For 22K steel of pearlitic grade at the temperature of 650 °C the following coefficients can be taken, when determining the temperature creep strain rate: $A = 1.73 \cdot 10^{-14}$, $n = 5$ [9], and for austenitic materials of deposits on the edges of SG branch pipe $A = 6.948 \cdot 10^{-14}$, $n = 6.22$ [12].

RESULTS OF MATHEMATICAL MODELING OF TEMPERATURE DISTRIBUTIONS AND MICROSTRUCTURAL PHASE TRANSFORMATIONS

Results of modeling the microstructural transformations in CWJ metal during welding heating ($T_{preheating}$ = = 100 °C) and further cooling revealed (Figure 8) local formation of hardening structures in the HAZ of SG branch pipe metal (22K steel). Figure 9 shows the graphs of the change of microstructural phase state in the characteristic point of SG base material HAZ during welding and further cooing, where maximal residual content of martensite was obtained for different values of the preheating temperature. Application of preheating on the level of T = 200 °C in CWJ welding allows lowering the maximal relative content of martensite in the HAZ from 50 to 20 %, compared to welding without preheating.

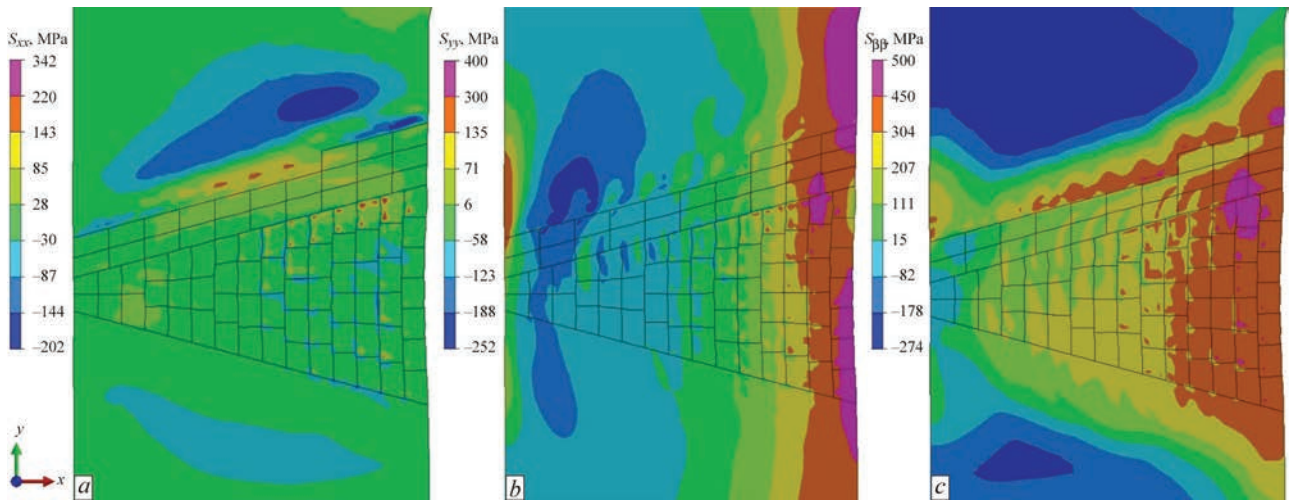

Figure 12. Residual stresses in CWJ after welding: *a* — radial σ_{xx}; *b* — axial σ_{yy}; *c* — circumferential $\sigma_{\beta\beta}$

RESULTS OF MATHEMATICAL MODELING OF RESIDUAL STRESSES AFTER WELDING AND AFTER HEAT TREATMENT

Figure 10 shows the distributions of residual stresses after surfacing the edge of SG branch pipe CWJ at the temperature of preheating and concurrent heating $T_{preheating}$ = 100 °C and subsequent cooling to T = 20 °C. The radial component (Figure 10, *a*) is characterized by a low level of stresses and local zones of maximum tensile stresses of up to 250 MPa in the austenitic material of the deposit. The axial (relative to branch pipe axis) component (Figure 10, *b*) is also characterized by the general low level of stresses and local zones of maximal tensile stresses of up to 300 MPa in the base material of SG branch pipe, which is adjacent to the austenitic weld metal on the inner and outer surfaces of the branch pipe. For the circular component of residual stresses (Figure 10, *c*) the tensile stresses (up to 400 MPa) were determined in the zone of SG branch pipe base material, adjacent to the austenitic weld metal.

After heat treatment (T = 650 °C, $T_{soaking}$ = 9 h) the level of residual stresses induced by surfacing the SG branch pipe edges decreases considerably: maximal radial tensile stresses are up to 120 MPa (Figure 11, *a*), axial ones are up to 130 MPa (Figure 11, *b*), circumferential stresses are up to 190 MPa (Figure 11, *c*).

After multipass welding performance very nonuniform distributions of residual stresses were obtained. The radial component in the welded joint zone (Figure 12, *a*) is characterized by a low level of stresses and local zones of maximal tensile stresses of up to 140 MPa in the base material of SG branch pipe, adjacent to the austenitic weld metal. Axial residual stresses (Figure 12, *b*) have a local zone of maximal tensile stresses

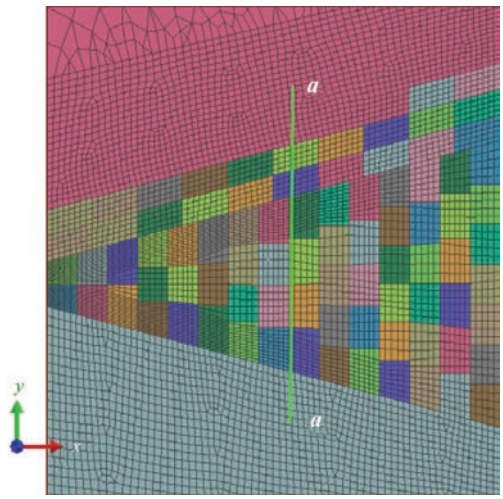

Figure 13. Welded joint section for determination of characteristic stress distributions

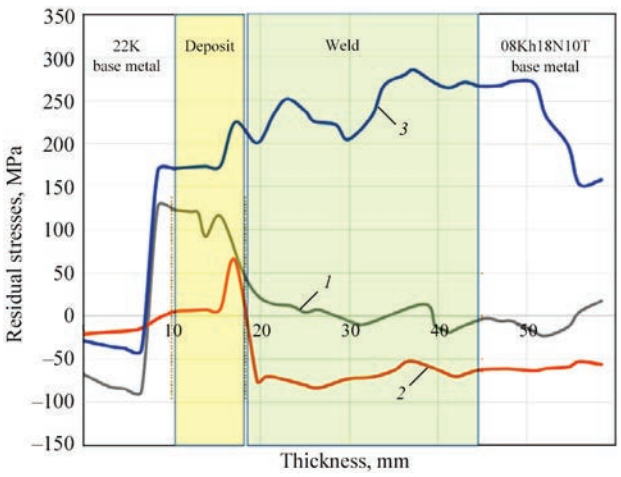

Figure 14. Residual stress distribution in the middle section (*a–a* in Figure 13) of the welded joint: *a* —radial σ_{xx}; *b* — axial σ_{yy}; *c* — circumferential $\sigma_{\beta\beta}$

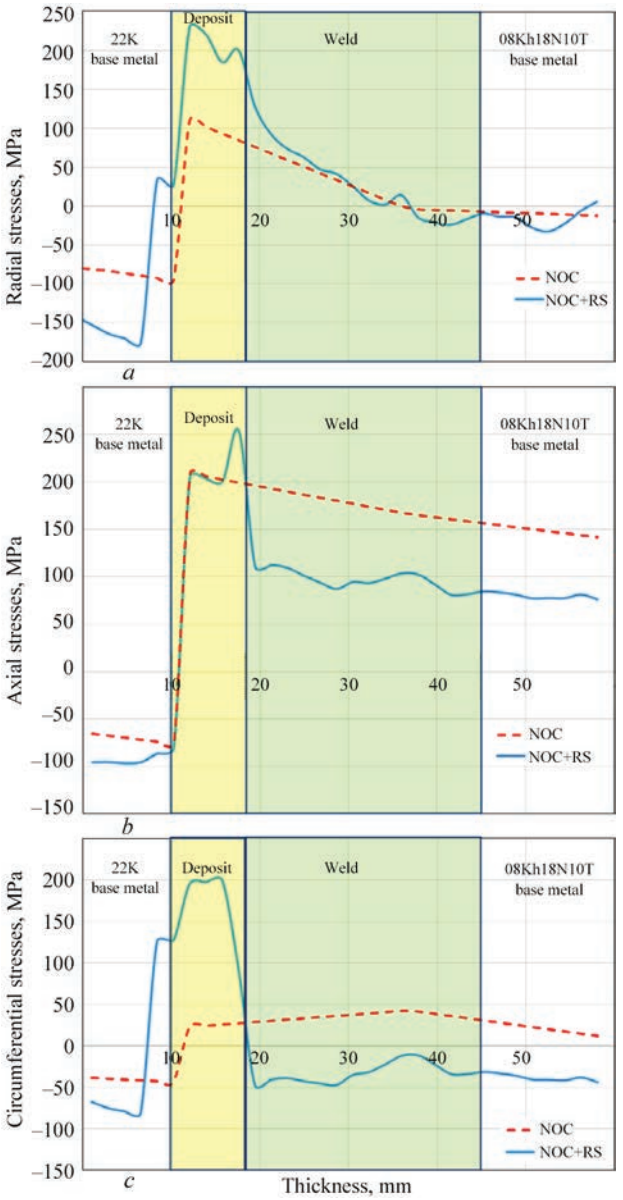

Figure 15. Distributions of operational stresses (operational at NOC, as well as summary operational and residual stresses) in the middle section (*a–a* in Figure 13) of the welded joint: *a* — radial σ_{xx}; *b* — axial σ_{yy}; *c* — circumferential $\sigma_{\beta\beta}$

of up to 200 MPa on the joint inner surface in the base material of SG branch pipe, adjacent to the austenitic weld metal, and tensile stresses of up to 400 MPa are found on the joint outer surface. The highest tensile stresses (up to 450 MPa) were determined for the circular component of the residual stresses (Figure 12, *c*) in the zone of base material of SG branch pipe, adjacent to austenitic weld metal, as well as in the weld material closer to the joint outer surface.

Thus, modeling of CWJ welding showed rather high residual tensile stresses. It is particularly dangerous on the joint inner surface, which is in contact with the coolant corrosive medium in service, as well as in the zone of contact (fusion) of the branch pipe material, namely of pearlitic grade steel with the austenitic metal of the deposit (weld). In this zone there is a high probability of discontinuity defect formation in welding, which may have a negative effect on SG strength at further long-term service.

The graphs of distribution of residual stresses (Figure 14) and operational stresses (operational at normal operating conditions (NOC), as well as summary operational and residual stresses) (Figure 15) in the welded joint middle section (*a–a* in Figure 13) of the welded joint were plotted. The influence of residual stresses (RS) on the stressed state of CWJ assembly is quite significant, namely, in the zone of surfacing and contact (fusion) of the material of branch pipe pearlitic steel to the austenitic metal of the deposit, a noticeable increase in the total stresses takes place, compared to the operational stresses, without allowing for residual stresses (Figure 15, *a*, *c*).

CONCLUSIONS

Analysis of the results of mathematical modeling of the thermal processes, microstructural phase transformations and SSS in the composite welded joint of the collector and the adapter sleeve of PGV-440 steam generator showed that:

1. In welding without preheating, the residual content of hardening structures in the HAZ of branch pipe metal (St22K) can reach 65 %. Application of preliminary (concurrent) preheating ($T \geq 200$ °C) allows a significant lowering of the relative content of martensite in the base material on the fusion boundary with austenitic material of the weld. However, considering the possible violations of the surfacing and welding technology at steam generator manufacture, we should assume the presence of hardening structures in the HAZ of branch pipe metal and lowering of the material crack resistance characteristics.

2. Failure to perform the final postweld heat treatment leads to formation of a complex pattern of distribution of residual stresses with high tensile stresses, both in the zone of the pearlitic material of the branch pipe, and in the zones of austenitic materials of the weld and the collector adapter sleeve.

3. Rather high residual tensile stresses were determined on the inner surface of the composite joint, which during operation is in contact with the coolant corrosive medium, as well as in the zone of fusion of the material of branch pipe pearlitic steel and austenitic metal of the weld, where there is a rather high probability of discontinuity defect formation in welding, which may have a negative influence of the strength and structural integrity of SG welded assembly at further long-term service.

REFERENCES

1. Makhnenko, V.I., Saprykina, G.Yu. (2002) Role of mathematical modeling in solving problems of welding dissimilar steels (Review). *The Paton Welding J*., **3**, 14–25.
2. Makhnenko, V.I., Kozlitina, S.S., Dzyubak, L.I. et al. (2010) Risk of formation of carbides and α-phase in welding of high-alloy chrome-nickel steels. *The Paton Welding J*., **12**, 5–8.
3. Wenchun, J., Wanchuck, W., Yun, L. et al. (2017) Residual stress distribution in a dissimilar weld joint by experimental and simulation study. ***J.*** *of Pressure Vessel Technology*, **139**, 011422-1-011422-10.
4. Deng, D., Ogawa, K., Kiyoshima, S. et al. (2009) Prediction of residual stresses in a dissimilar metal welded pipe with considering cladding, buttering and post weld heat treatment. *Computational Material Sci*., **47**, 398–408.
5. Kasatkin, O.G., Tsaryuk, A.K., Skulsky, V.Yu. et al. (2007) Method for improving local damage resistance of welded joints in NPP pipelines. *The Paton Welding J*., **3**, 27–30.
6. *Steam generator PGV-213*: Operating manual U 213-I-553 [in Russian].
7. *Steam generator body*: Certificate. 1137.50.06.000 PS [in Russian].
8. *Steam generator body*: Certificate. 1137.50.07.000 PS [in Russian].
9. Makhnenko, V.I. (2006) *Safe service life of welded joints and assemblies of modern structures*. Kyiv, Naukova Dumka [in Russian].
10. SOU NAEK 159E: *Safe operation. Welding and surfacing of equipment and pipelines of nuclear power plants with WWER reactors* [in Russian].
11. Rabotnov, Yu.N. (1966) *Creep of structure elements*. Moscow, GIFML [in Russian].
12. Margolin, B.Z., Gulenko, A.G., Kursevich, I.P. et al. (2006) Modeling for fracture in materials under long-term static creep loading and neutron irradiation. Pt 2. Prediction of creep rupture strength for austenitic materials. *Strength of Materials*, 38(**5**), 449–457.
13. Khodakov, V.D., Kharina, I.D., Korneev, A.E. (2008) Examination of nature and damage causes of dissimilar welded joints in welding of transition ring to branch pipe Dn1100 assembly at Novovoronezhsky and Kolsky NPP. In: *Proc. of 10th Int. Conf. (St.-Petersburg, October 2008)*. Vol. 2, St.-Petersburg, Prometej.
14. Vardanyan, A.M. ((2017) *Evaluation of influence of service conditions on residual life of assemblies of steam generators of power units WWER-440*: Syn. of Thesis for Cand. of Tech. Sci. Degree. Erevan, NPUA [in Russian].
15. Kasatkin, O.G., Seyffarth, P. (2002) Calculation models for evaluation of mechanical properties of HAZ metal in welding of low-alloyed steels. In: *Proc. of Int. Conf. on Mathematical*

Modeling and Information Technologies in Welding and Related Processes. Kyiv, 103–106.
16. (2003) *Steel and alloy grades*. Ed. by A.S. Zubchenko. Moscow, Mashinostroenie [in Russian].
17. (2003) *Mechanical properties of structural materials in complex stress state.* Ed. by A.A. Lebedev. Kyiv, In Yure [in Russian].
18. Seyfarth, Meyer, Scharf (1992) Großer Atlas Schweiß-ZTU-Schaubilder *Fachbuchreihe Schweißtechnik*, **110**. Düsseldorf, DVS Verlag.
19. Saunders, N., Guo, U.K., Li, X. et al. (2003). Using JMatPro to model materials properties and behavior. *JOM*, **55**, 60–65. DOI: https://doi.org/10.1007/s11837-003-0013-2

ORCID
A.A. Makarenko: 0000-0002-4713-9726,
O.V. Makhnenko: 0000-0002-8583-0163

CONFLICT OF INTEREST
The Authors declare no conflict of interest

CORRESPONDING AUTHOR
O.V. Makhnenko
E.O. Paton Electric Welding Institute of the NASU
11 Kazymyr Malevych Str., 03150, Kyiv, Ukraine.
E-mail: makhnenko@paton.kiev.ua

SUGGESTED CITATION
A.A. Makarenko, O.V. Makhnenko (2023) Mathematical modeling of residual stresses in a composite welded joint of the collector adapter sleeve and the branch pipe of PGV-440 steam generator. *The Paton Welding J.*, **3**, 8–19.

JOURNAL HOME PAGE
https://patonpublishinghouse.com/eng/journals/tpwj

Received: 08.03.2023
Accepted: 24.04.2023

DOI: https://doi.org/10.37434/tpwj2023.03.03

ELECTRON BEAM SURFACE MELTING OF INGOTS OF HIGH-TEMPERATURE TITANIUM ALLOY VT9

O.M. Pikulin, S.V. Akhonin, V.O. Berezos, A.Yu. Severyn, O.G. Yerokhin

E.O. Paton Electric Welding Institute of the NASU
11 Kazymyr Malevych Str., 03150, Kyiv, Ukraine

ABSTRACT

Proceeding from the results of the performed package of research work, it was established that the chemical composition of metal in the surface-melted layer of high-temperature titanium alloy VT9 corresponds to standard requirements; and a lowering of aluminium content, an alloying element with vapour pressure higher, and an increase in the content of molybdenum and zirconium, alloying elements with vapour pressure lower than that of titanium, is observed. Investigations of the surface-melted layer showed that the penetration depth of the surface layer in ingots of high-temperature titanium alloy VT9 of 600 mm diameter reaches 8 mm, the ingot surface is high-quality mirror-like with characteristic vacuum etching, even microrelief without cracks, tears or lacks-of-fusion, its roughness is within the range of 3–4 class at a waviness of 0.2–0.6 mm. The surface-melted layer of the ingot has a finer structure, compared to base metal, and it consists of areas with isolated α-plates of 1.0–2.5 μm thickness, where the α-plates are gathered into colonies of 10–50 μm width, and the gaps between them are taken up by dispersed particles of 1–2 μm size, which can be the products of metastable phase decomposition.

KEYWORDS: high-temperature titanium alloy, ingot, surface defect, electron beam surface melting, chemical composition, structure

INTRODUCTION

In recent decades, an increased attention has been paid to the creation of alloys based on refractory and chemically active metals. Aerospace and aircraft engineering requires light and strength materials that will be able to supplement high-temperature nickel-, cobalt- and iron-based alloys traditionally used in these areas. The use of titanium-based high-temperature alloys is one of the ways to solve this problem. The world trends in the development of high-temperature titanium alloy ingots and making semi-finished products of them for manufacture of parts are mostly general for leading aircraft enterprises and namely the technology of manufacturing them is a decisive factor in providing stability and the required level of operational properties [1–4].

Figure 1. Ingot of high-temperature titanium alloy VT9 with a diameter of 600 mm, produced by EBM method

ANALYSIS OF LITERATURE DATA AND PROBLEM STATEMENT

Reducing the cost of ingots of high-temperature titanium alloys as an output link for manufacturing semi-finished products simultaneously with the improvement of their quality is a relevant task, since the determining factor in making the decision on their use instead of conventional structural materials is a price-quality ratio [5, 6].

One of the progressive trends in metallurgical production of high-temperature titanium alloys is electron beam melting, which allows not only cleaning these materials from gas and volatile metal impurities, but also significantly simplifying the process of metallurgical treatment and provides manufacturing products with qualitatively new mechanical properties. Electron beam melting also provides the possibility of producing high-temperature titanium alloy ingots by remelting the primary charge in the form of spongy titanium and master alloy [5, 6]. However, for a number of reasons caused by metallurgical and technological features, in the process of electron beam remelting, on the surface of produced ingots, defects in the form of corrugations, cracks, tears and longitudinal strip of metal filling may occur (Figure 1) [7].

It is almost impossible to avoid the formation of this type of defects in EBM, which, in turn, complicates the further heat treatment of ingots and billets, leads to the propagation of hot cracks. The necessary quality of the surface of ingots and billets is achieved by removing the surface layer during mechanical treatment. The mechanical properties of titani-

um-based alloys show that the efficiency of the blade stripping on existing machine-tools is 3–6 times lower than during stripping of alloyed structural steels, and the heat conductivity of titanium-based alloys during blade stripping causes local overheating at the place of contact with the cutter and, as a consequence, to oxidization of chips. High requirements to cleanliness of the source charge materials impose a number of restrictions on reused chips for ingots, which leads to irreversible metal losses [8, 9].

Thus, the works are promising, which study the possibility of non-waste removal of surface defects of the ingots. Positive results of such works allow reducing metal losses in the form of non-conditional wastes (chips) and valuable alloying elements. At the same time, the most promising is the way of application of new technological processes that allow excluding some technological redistributions from the production chain, and at the expense of it improving the quality of the ingot surface, improving the output of suitable material and significantly reducing the cost of products.

At the PWI of the NASU, an extensive experience has been gained in the use of electron beam for treatment of a surface layer of ingots of round and rectangular sections, a number of studies have been conducted using mathematical modeling of the processes of heat and mass transfer in the ingot treated by electron beam [10]. On the basis of these studies, the technology of electron beam surface melting and specialized equipment for its implementation have been developed [10].

The conducted investigations were aimed at studying the effectiveness of the use of the technology of electron beam surface melting of the surface layer of ingots of high-temperature titanium alloy VT9 and the influence of technological parameters of electron beam surface melting on the chemical composition, penetration depth of the surface layer and the structure of the ingot metal.

To achieve the set aim, the following tasks were solved:

- to study the chemical composition and structure of the base metal and the surface-melted layer of ingots;
- to determine the penetration depth of the surface layer of ingots.

MATERIALS AND RESEARCH METHODS

The first widely used serial high-temperature titanium alloy was titanium (α+β)-alloy VT3-1, developed in 1957. The alloy was used for GTE parts, operating for a long time at temperatures of up to 450 °C. In 1958, titanium alloys VT8 and VT9 were developed for long-term operation at 500 °C [11].

The alloy VT9 is a two-phase (α+β)-alloy. A high content of aluminium and silicon alloying provide higher heat-resistant properties compared to alloy VT6. Titanium alloy VT9 is a wrought alloy and refers to materials with a high heat and corrosion resistance. The alloy VT9 is strengthened by heat treatment — hardening and aging. The optimal combination of mechanical properties is provided by double annealing. It can be used to produce GTE parts — discs, blades and other compressor parts [12, 13].

The metal of the high-temperature titanium alloy VT9 was produced by the technology of electron beam melting with cold hearth developed at the PWI. The surface of the produced ingots was subjected to electron beam treatment in the specialized electron beam installation UE-185 (Figure 2) for surface melting of the ingots according to the modes obtained on the results of mathematical modeling of processes of heat and mass trnasfer in the ingots of titanium alloys in electron beam surface melting [10].

Surface melting of ingots of high-temperature titanium alloy VT9 with a diameter of 600 mm was carried out according to the scheme, where the electron beam is fixed and the ingot rotates around its axis (Figure 3). In this case, the linear rate of surface melting was 54 mm/min, and the specific heating power was 7.25 W/mm^2.

To investigate the impact of technological parameters of electron beam surface melting on the chemical composition and penetration depth of the treated layer, the samples were selected in the form of chips and cut-off samples before and after surface melting (Figure 4).

For accurate analysis of the content of alloying elements in the ingots of the produced alloys, the method of optical emission spectrometry with an inductively-coupled plasma (ICP-OES) in the ICP-spectrome-

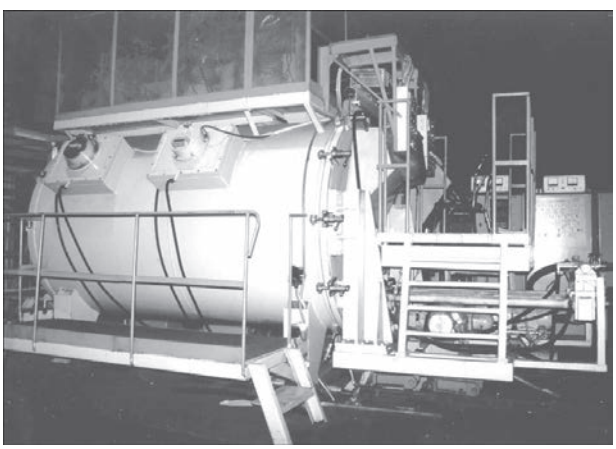

Figure 2. Appearance of a specialized electron beam installation for surface-melting of ingots

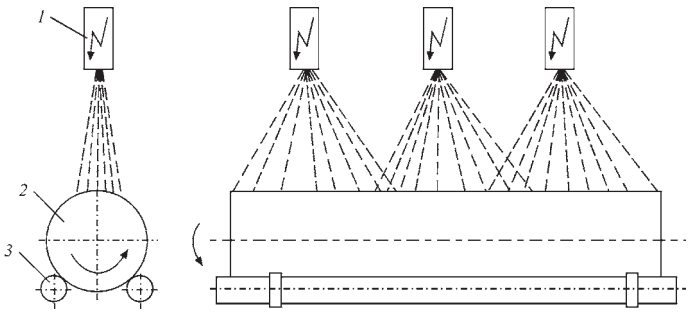

Figure 3. Surface melting scheme: *1* — electron beam gun; *2* — ingot; *3* — rolls

Table 1. Mass concentration of alloying elements in the metal of surface-melted layer of ingots of high-temperature titanium alloy VT9, wt.%

Place of sampling	Al	Mo	Fe	Zr	Si	O	N
Base	6.64	3.63	0.21	1.64	0.32	0.11	0.012
Surface-melted layer	6.13	3.68	0.20	1.69	–"–	0.13	0.016
OST1 90013–81	5.8–7.0	2.8–3.8	≤0.25	1.0–2.0	0.20–0.35	<0.15	<0.05

ter ICAP 6500 DUO of Thermo Electron Corporation production was used. To determine the content of oxygen and nitrogen, the samples of cylindrical shape with diameter and length of 3 mm were made. The content was determined in the devices RO-316 and TN-114 of LECO Company (USA).

The macrostructure of ingots was studied on the transverse templates, cut out from the middle of the ingots. The structure was revealed by etching the templates in a 15 % solution of fluoride acid with the addition of a 3 % solution of nitric acid at room temperature.

To reveal the microstructure of the samples, etching was carried out in a special reagent, which consisted of a mixture of acids in the ratio: 1 part of hydrofluoric (HF) and 3 of nitrogen (HNO_3).

The structure of the samples was examined in the light microscope Neophot-32 at different magnifications. The photos of microstructures were obtained by means of a digital camera C-3000 of OLYMPUS Company.

RESEARCH RESULTS AND DISCUSSION

In order to check the efficiency of the use of electron beam surface melting of the surface layer of high-temperature titanium alloy at the production facilities of SE "SPC "Titan" of the PWI", comprehensive research work were carried out in melting of the batch of ingots with a diameter of 600 mm and a length of up to 2 m and surface melting of their side surface by electron beam (Figures 1, 5).

The side surface of the ingots, melted with an electron beam, had an even microrelief, it was mirror-like with a characteristic vacuum etching, without cracks, tears and lacks-of-fusion, its surface roughness was within 3–4 classes at a waviness of 0.2–0.6 mm (Figure 5).

The results of studies of mass concentration of alloying elements in the metal of the surface-melted layer of ingots of the high-temperature titanium

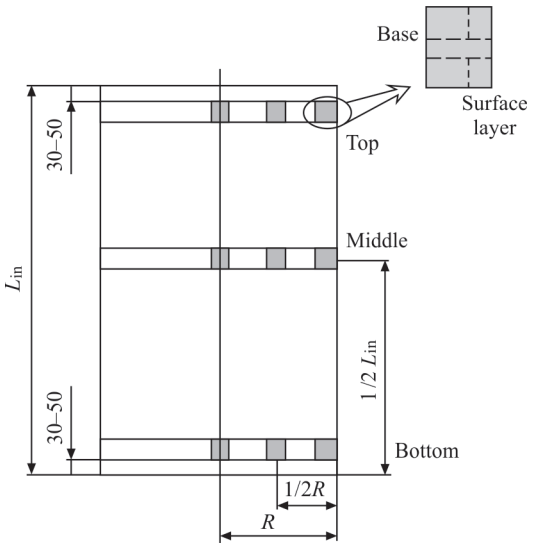

Figure 4. Scheme of sampling for chemical and metallographic analysis

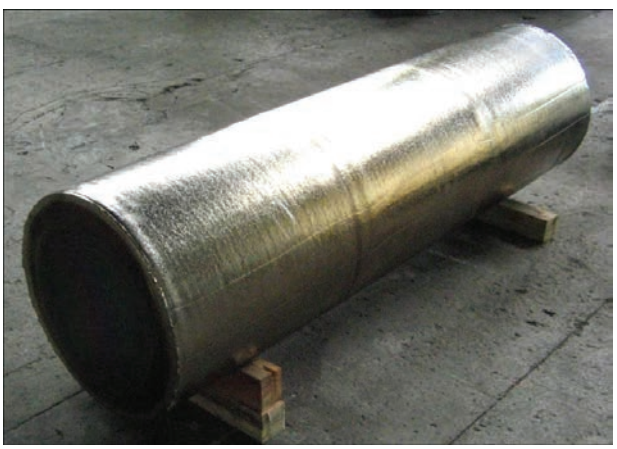

Figure 5. Ingot of high-temperature titanium alloy VT9 of 600 mm diameter with a surface-melted side surface

alloy VT9 showed that their content corresponds to the grade composition, a decrease in the content of aluminium is observed, alloying element with vapor elasticity higher than in the base of the alloy, and an increase in the content of molybdenum, zirconium, alloying elements with vapor elasticity lower than in the base of the alloy (Table 1).

The experimental evaluation of penetration depth of the surface layer of ingots according to the above-mentioned modes was performed on the transverse templates and it amounted up to 8 mm (Figure 6). In this case, the side surface of the ingots had an even microrelief, it was mirror-like with characteristic vacuum etching, without cracks, tears, and lacks-of-fusion (Figure 5).

Metallographic analysis of the metal of the surface-melted ingot of the titanium alloy VT9 was carried out in order to detect structural changes that took place in the metal as a result of thermal impact of the electron beam on the side surface and the base of the ingot. The macrosections of the ingot of the alloy VT9 of 600 mm diameter with the layer surface-melted by electron beams on the surface had no cavities and discontinuities. The macrostructure was characterized by the crystals close to equiaxial, the surface-melted layer was formed by smaller crystals compared to the base of the ingot, elongated towards the crystallization, i.e. to the center of the ingot.

Near the surface of the ingot, the grains of 0.8–1.2 mm size, which were observed to a depth of about 8 mm from the surface, were formed, further in the ingot, the grains were much coarser (Figure 7).

Microstructure of the metal of the surface-melted layer at a larger magnification is shown in Figure 8. The heat-affected-zone from the action of electron beam in melting of the surface is probably narrow and may represent a part of the grain that is not structurally different from the rest of the metal of the ingot. The size of the grain, which is determined on the 10-point scale of macrostructures of the Instruction No. 1054–76 VIAM, corresponds to the grain size Nos 6–7 in the surface-melted layer and the grain size Nos 8–9 in the area of the base metal.

Figure 6. Macrostructure of metal of ingot of high-temperature titanium alloy VT9 of 600 mm diameter with a surface-melted side surface

Examination of the sample microstructure has shown that the surface-melted layer consists of areas with single α-plates, the gaps between which are taken up by dispersed particles. In the metal of the surface-melted layer, there are also areas of the structure, where α-plates are gathered in colonies of different sizes, and dispersed particles are in the gaps between the parallel plates (Figure 8). The areas with single α-plates predominate near the surface of the ingot and deeper in the surface-melted layer, a number of α-colonies is increased. The width of α-colonies in the surface-melted layer is 10–50 μm, and the thickness of α-plates is 1.0–2.5 μm. In the rapidly cooled metal of the surface-melted layer, metastable β-phases and martensite phases can be present. Dispersed particles can be the products of metastable phase decomposition. The size of dispersed particles is 1–2 μm.

The metal microstructure of the ingot base is shown in Figure 9, from which it is seen that in the

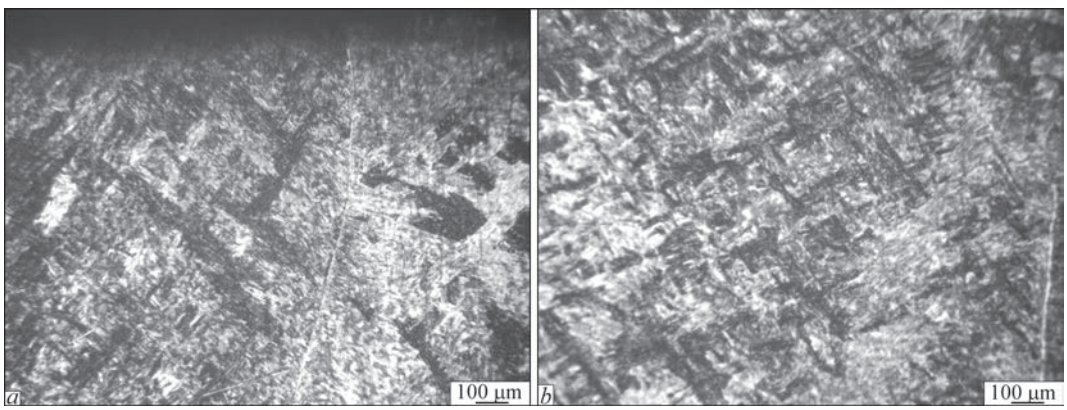

Figure 7. Microstructure of metal of ingot of high-temperature alloy VT9 with a surface-melted side at a depth, mm: *a* — 0.5; *b* — 12.0

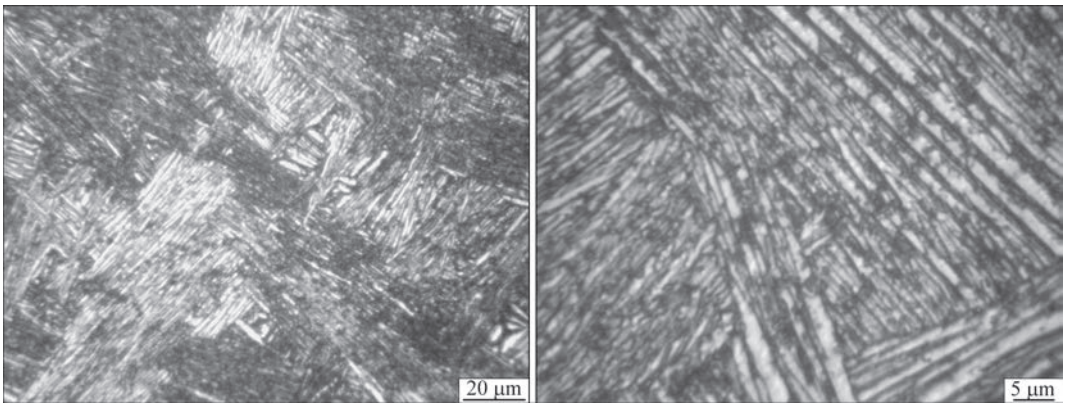

Figure 8. Microstructure of metal of surface-melted ingot at different magnification

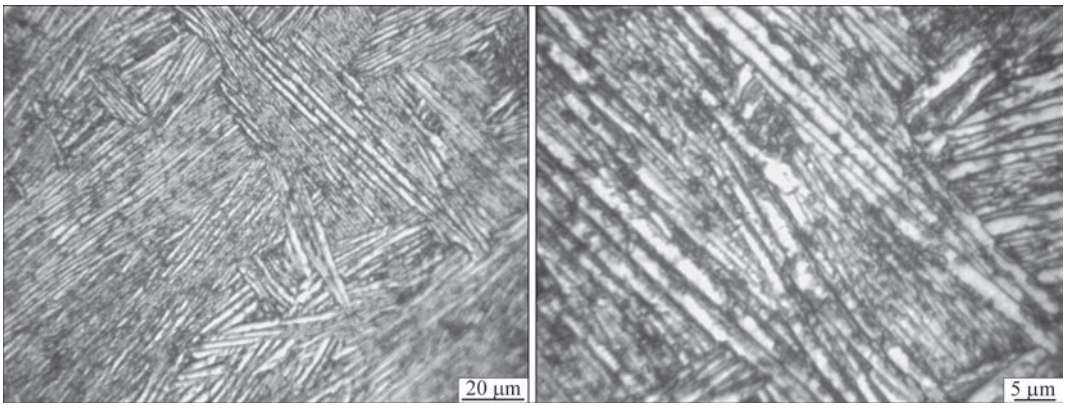

Figure 9. Microstructure of metal base of ingot at different magnification

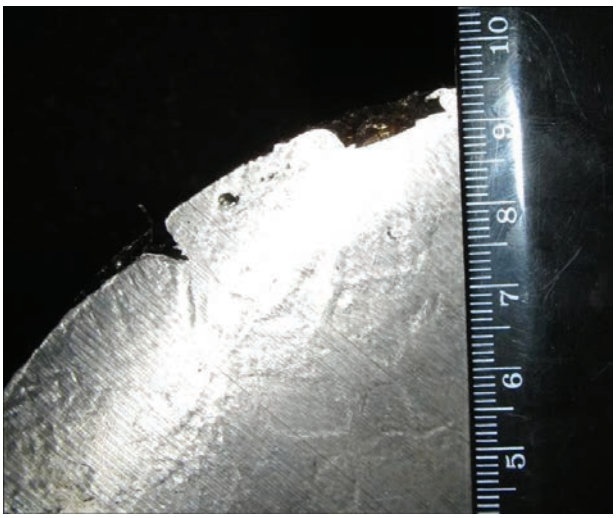

Figure 10. Defective layer of ingot surface

metal a coarse-grained structure predominates, the formation of which was facilitated by a slow cooling of the large volume of metal. The boundaries of primary β-grains are decorated with α-fringe, which in places is continuous and sometimes is intermittent, its width is up to 7 μm. The intragranular structure consists mainly of α-colonies of 10–60 μm. In the gaps between the colonies the areas with a dispersed structure are observed, the sizes of dispersed particles are up to 1–2 μm. Such small particles are also present between α-plates in the colony. In our opinion, this can be explained by the fact that during a slow cooling of the large-sized ingot, a redistribution of alloying elements occurs between the phase components, resulting in the decomposition of metastable martensite phases and β-metastable phase with the precipitation of dispersed particles of stable α- and β-phases. The thickness of the plates in colonies is 1–3 μm.

Thus, the results of the analysis of the microstructure of the surface-melted layer and the base of the ingot of the high-temperature titanium alloy VT9 indicate that the treatment of the ingot surface by electron beams on the abovementioned modes leads to the refinement of α-colonies and α-plates of grains in the surface-melted layer compared to the ingot base.

According to standard technology, defects formed on the surface of ingots of titanium alloys during their melting are eliminated by removing the surface layer using mechanical methods. The thickness of the defective layer, removed from the ingot surface, reaches up to 9 mm (Figure 10), the losses in the chips are up to 100–140 kg for an ingot with a diameter of 600 mm, which amounts up to 4.0–5.5 % of the total ingot mass.

Therefore, the technology of electron beam melting of the ingot surface layer of a high-temperature titanium alloy VT9 allows producing a high-quality

metal in the surface-melted layer with a high efficiency, which meets the requirements of the standard and at the same time maintaining up to 5.5 % of the ingot total mass of a high cost metal.

CONCLUSIONS

1. It was established that the chemical composition of the metal in the surface-melted layer of high-temperature titanium alloy VT9 meets the requirements of the standard, a decrease in aluminium content, alloying element with vapour elasticity higher and an increase in the content of molybdenum, zirconium, alloying elements with vapour elasticity lower than in titanium is observed.

2. It is shown that the penetration depth of the surface layer of ingots of a high-temperature titanium alloy VT9 with a diameter of 600 mm, produced by the technology of electron beam surface-melting reaches up to 8 mm, and the ingot surface is high-quality, mirror-like with characteristic vacuum etching, even microrelief without cracks, tears and lacks-of-fusion, its roughness is within 3–4 class at a waviness of 0.2–0.6 mm.

3. It is shown that the surface-melted layer of the ingot has a smaller structure compared to the base metal and consists of areas with single α-plates of 1.0–2.5 μm thickness, where α-plates are gathered in colonies with a width of 10–50 μm, the gaps between which occupied by dispersed particles with the sizes of 1–2 μm that can be the products of metastable phase decomposition.

REFERENCES

1. Niinomi, M. (2011) Recent trends in titanium research and development in Japan. In: *Proc. of 12th World Conf. on Titanium*, **1**, 30–37.
2. Bania, P. (1993) Beta titanium alloys and their role in the titanium industry. *Beta Titanium Alloys in the 90's*. TMS Publ., Warrendale, PA, 3–14.
3. Cui, C., Hu, B.M., Zhao, L., Liu, S. (2011) Titanium alloy production technology, market prospects and industry development. *Mater. Des*., **32**, 1684–1691. DOI: http://doi/org/10.1016/j.matdes.2010.09.011?
4. Babenko, E.P., Dolzhenkova, E.V. (2014) Investigation of the causes of destruction of a large-sized product made of VT23 alloy. *Metallurgical and Mining Industry*, **3**, 82–85.
5. Khoreev, A.I. (2007) Theory and practice of development of titanium alloys for promising structures. *Tekhnologiya Mashinostroeniya,* **12**, 5–13 [in Russian].
6. Antonyuk, S.L., Moyar, A.G., Kalinyuk A.N. et al. (2003) Titanium alloys for aircraft industry of Ukraine. *Advances in Electrometallurgy*, **1**, 9–13.
7. Pikulin, A.N. (2016) Electron beam fusion of complexly-alloyed titanium alloys. Sovrem. Elektrometall., **3**, 26–30 [in Russian].
8. Koryagin, S.I., Pimenov, I.V., Khudyakov, V.K. (2000) *Methods of treatment of materials: Manual.* Kaliningrad, Kaliningr. University [in Russian].
9. Krivoukhov, V.A., Chubarov, A.D. (1990 *Cutting of titanium alloys*. Moscow, Mashinostroenie [in Russian].
10. Paton, B.E., Trigub, N.P., Akhonin, S.V., Zhuk, G.V. (2006) *Electron beam melting of titanium.* Kyiv, Naukova Dumka [in Russian].
11. Pavlova, T.V., Kashapov, O.S., Nochovnaya, N.A. (2012) *Titanium alloys for gas turbine engines. All materials.* Encyclopaedic Handbook [in Russian].
12. Khoreev, A.I., Khoreev, M.A. (2005) Titanium alloys, their application and prospects of development. *Materialovedenie*, **7**, 25–34 [in Russian].
13. Aleksandrov, V.K., Anoshkin, N.F., Bochvar, G.A. et al. (1979) *Semi-finished products from titanium alloys. Moscow, Metallurgiya* [in Russian].

ORCID

O.M. Pikulin: 0000-0001-6327-3848,
S.V. Akhonin: 0000-0002-7746-2946,
V.O. Berezos: 0000-0002-5026-7366,
A.Yu. Severyn: 0000-0003-4768-2363,
O.G. Yerokhin: 0000-0003-2105-5783

CONFLICT OF INTEREST

The Authors declare no conflict of interest

CORRESPONDING AUTHOR

S.V. Akhonin
E.O. Paton Electric Welding Institute of the NASU
11 Kazymyr Malevych Str., 03150, Kyiv, Ukraine.
E-mail: akhonin.sv@gmail.com

SUGGESTED CITATION

O.M. Pikulin, S.V. Akhonin, V.O. Berezos, A.Yu. Severyn, O.G. Yerokhin (2023) Electron beam surface melting of ingots of high-temperature titanium alloy VT9. *The Paton Welding J*., **3**, 20–25.

JOURNAL HOME PAGE

https://patonpublishinghouse.com/eng/journals/tpwj

Received: 02.12.2022
Accepted: 24.04.2023

DOI: https://doi.org/10.37434/tpwj2023.03.04

FEATURES OF THE STRUCTURE AND PHYSICO-CHEMICAL PROPERTIES OF COPPER PRODUCED BY THE METHOD OF ELECTRON BEAM EVAPORATION AND CONDENSATION IN VACUUM

V.G. Hrechanyuk[1], M.I. Hrechanyuk[2], O.V. Khomenko[2], I.M. Hrechanyuk[1], V.I. Hots[1]

[1]Kyiv National University of Construction and Architecture of the MESU
31 Povitroflotskyi Prosp., 03037, Kyiv, Ukraine
[2]I.M. Frantsevych Institute of Materials Science Problems
3 Omelyan Pritsak Str., 03680, Kyiv, Ukraine

ABSTRACT

The structure and physico-chemical properties of copper, produced by the method of electron beam evaporation and condensation in vacuum were studied. A substrate from steel of St3 grade heated to 700 ± 15 °C was used for metal deposition. An intermediate pool from Cu–Zr–Y alloy was applied in the experiments. Evaluation of the properties of condensed copper, compared to cast one, showed a small difference in the values of specific electric resistance, and a certain increase of the level of mechanical characteristics, that is, probably, associated with the differences in its intragranular block structure. A 1.5 times increase of the condensate hardness was found in the case, when the intermediate pool was used, which is related to Zr and Y microalloying. Gravimetric studies of condensed copper corrosion in water revealed a significant influence on this process of such factors as presence of hardness salts in tap water and high specific electric resistance of distilled water. The greatest changes in the sample weight were observed in the first 10 h of corrosion testing, and then process stabilization and monotonic decrease of sample weight took place. In tap water copper is characterized by the highest corrosion resistance, weight losses being two times higher under dynamic testing conditions than this value for static testing. Under dynamic conditions, the medium movement prevents salt deposition, and electric resistance increase becomes slower. Analysis of corrosion polarization diagrams confirmed the slowing down of corrosion processes in tap water, compared to distilled water. Results of measurement of surface electric resistance of the samples before and after testing showed that the initial corrosion period with a relatively fast weight change, is characterized by an abrupt increase of electric resistance of the sample surface, which points to a predominant formation of copper oxide (I); and reduction of the dynamics of electric resistance change in the next testing periods is due to stabilization of the processes of film growth with copper oxide formation (II).

KEYWORDS: electron beam evaporation, vacuum, copper, condensates, mechanical characteristics, corrosion resistance

INTRODUCTION

At present many composite materials (CM) are manufactured on copper base, which is due to its unique properties [1]. In particular, by its low values of specific electric resistance (at 20 °C it is equal to $1.724–1.80 \cdot 10^{-8}$ Ohm·m), copper is inferior only to silver. Due to that it is widely used in electrical engineering industry for manufacture of power cables, wires and other conductors.

Copper purity has a decisive influence on CM properties, as impurities abruptly lower the electric conductivity [2–4]. Modern methods of refining metals and alloys, in particular, vacuum-induction, plasma-arc and electroslag melting, ensure quite efficient cleaning from metal impurities, nonmetallic inclusions and gases. The most significant results on copper refining, however, were obtained at application of the technology of electron beam remelting [5, 6]. The advantages of this technology are a deeper refining of the metal due to fractional distillation, dehydration, flotation and coagulation, while the high specific surface power in the working spot and availability of vacuum, which prevents gas absorption during welding allow controlling the beam power in space and time. All this enables realization of diverse technological schemes of the process, which it is difficult or impossible to conduct by other methods of vacuum metallurgy [7, 8].

Comprehensive analysis of the chemical composition and structure of condensates based on copper for electric engineering purposes [9–13] showed that formation of the structure, electrotechnical characteristics, mechanical strength and corrosion resistance essentially depends on the purity of the initial materials, which, alongside the alloying components, has a significant influence on the above characteristics. In this connection, studying the structural features and properties of pure condensed copper is of considerable interest. It allows determination of the influence of alloying components added to copper, on CM properties.

The objective of this work is studying the features of formation of the structure, mechanical characteristics and corrosion resistance of pure copper, produced by the method of electron beam condensation and evaporation in vacuum.

MATERIALS AND METHODS OF INVESTIGATION

Cast copper in ingots of MO DSTU 859:2003 grade was used as initial materials. Copper was evaporated in a multipurpose laboratory electron beam unit L-2. Its feature is the possibility of performance in one installation of the majority of typical technological processes, which are currently realized using diverse special-purpose electron beam units [14]. This unit is fitted with three hot cathode guns with strip cathode. The rated accelerating voltage is 20 kV. Vacuum in the working chamber, when producing the condensates, is on the level of 10^{-2}–$5 \cdot 10^{-3}$ Pa. The substrate for copper deposition was a plate from steel of St3 grade, heated to 700 ± 15 °C, on which a separation layer of CaF_2 was first deposited. A copper ingot of 70 mm diameter was placed into a copper water-cooled crucible, from which it was evaporated. The vapour flow deposition rate was 10–15 μm/min. Condensed copper sheets of 200×250 mm size and 1.0–1.2 mm thickness were produced as a result of conducting the evaporation-condensation process. Two series of experiments were performed. The second series differed from the first one by application of an intermediate pool from Cu–Zr–Y alloy during copper evaporation, which accelerated the copper evaporation rate 2–3 times [16]. The microstructure of the produced samples was studied by scanning electron microscopy, mechanical properties were determined at room temperature tensile tests of standard samples to DSTU ISO 6892-1:2019. Samples of initial cast copper of MO grade, DSTU 859:2003 after vacuum annealing for 2 h at 450 °C were also tested for comparison of the properties. Corrosion resistance was analyzed using gravimetric investigations, which were conducted with sample soaking in tap and distilled water for 100 h. Increase of the thickness of corrosion product films was controlled by measurement of electric resistance of the sample surface by the scheme shown

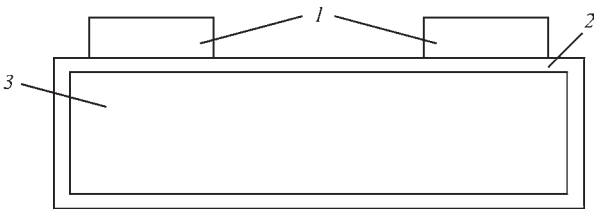

Figure 1. Scheme of contact application for measuring the electric resistance of the sample surface: *1* — put-on contacts; *2* — film; *3* — sample

in Figure 1. Control of the surface electric resistance was conducted after every 10 h of corrosion testing.

INVESTIGATION RESULTS AND THEIR DISCUSSION

Comparative evaluation of the properties of condensed copper and copper produced by the casting method, showed a slight difference of their values (Table 1). A slight increase of electric resistance of condensed copper, produced through an intermediate pool, is attributable to additional alloying by zirconium and yttrium in the total amount of 0.05–0.10 wt.%. Some changes in the level of mechanical characteristics of deposited copper, compared to cast metal, are associated with differences in its intragranular block structure, which forms under the conditions of physical deposition of copper in vacuum [16]. More over, increase of the condensate electric resistance and hardness (1.5 times) in case of application of an intermediate pool, is also associated with copper microalloying by zirconium and yttrium. Final conclusions on this issue require further detailed electron microscopy studies of the condensate microstructure.

Performed electron microscopy studies showed that pure copper condensates have a clearcut columnar structure with crystallite dimensions of approximately 35–40 μm (Figure 2).

Room temperature studies of copper condensate fractures demonstrated the tough fracture mode by the mechanism of microvoid coalescence with large plastic deformation preceding the fracture (Figure 3).

Cast copper and its alloys are prone to uniform corrosion, but here pitting, cavitation and intercrystalline types of corrosion, as well as corrosion cracking are observed [16]. Pure copper has satisfactory corrosion resistance under atmospheric conditions at room temperature. Here, the purer the copper, the higher is its

Table 1. Main physical and mechanical properties of condensed and cast copper

Copper	ρ (density), kg/m^3	*R*, μOhm·m	σ_t, MPa	σ_y, MPa	δ, %	*HB*, MPa
Condensed	$8.85 \cdot 10^3$	0.0181	210–220	55–60	53–55	500–600
Condensed through an intermediate pool	–»–	0.0183	215–225	56–61	50–53	520–630
Cast, annealed	$8.9 \cdot 10^3$	0.0178	200–240	70	40–50	350–400

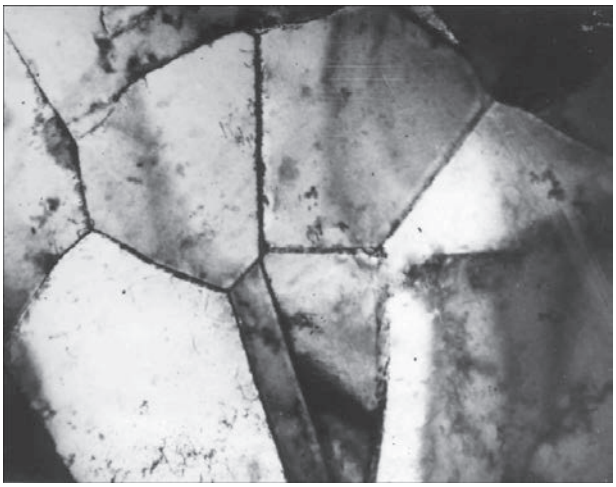

Figure 2. Microstructure of condensed copper in the cross-section, normal to vapour flow incidence (×8000)

corrosion resistance. Pure copper is resistant to atmospheric corrosion due to formation of a thin protective film of $CuSO_4 \cdot 3Cu(OH)_2$ composition on its surface. Fresh water and vapour condensate have practically no effect on copper. The corrosion rate of copper in sea water is also low. In humid air copper oxidizes, forming basic copper carbonate (II):

$$2Cu + H_2O + CO_2 + O_2 \rightarrow Cu_2CO_3(OH)_2\downarrow.$$

From the electrochemical point of view, the surface of copper condensate is microheterogeneous, which is determined by the presence of orientation of individual crystals, existence of grain boundaries, imperfections of the crystalline lattice as a result of dislocation formation and other violations of the fine structure. It leads to nonuniform overstress of the sample surface and, consequently, to running of the anode and cathode processes. Thus, copper corrosion in water environments proceeds by the electrochemical mechanism [17].

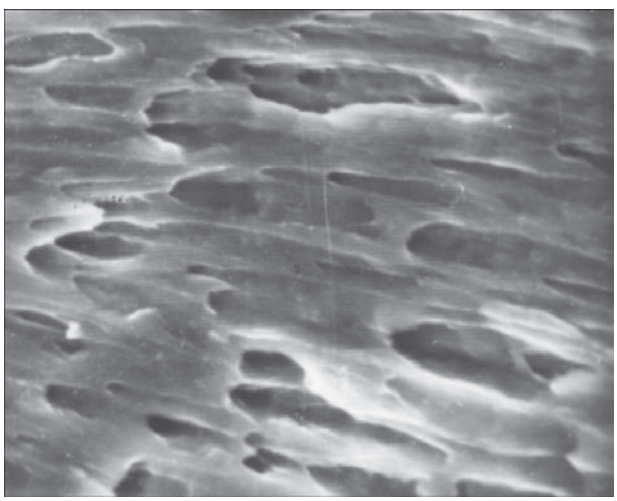

Figure 3. Electronic fractogram of copper condensate fracture (×400)

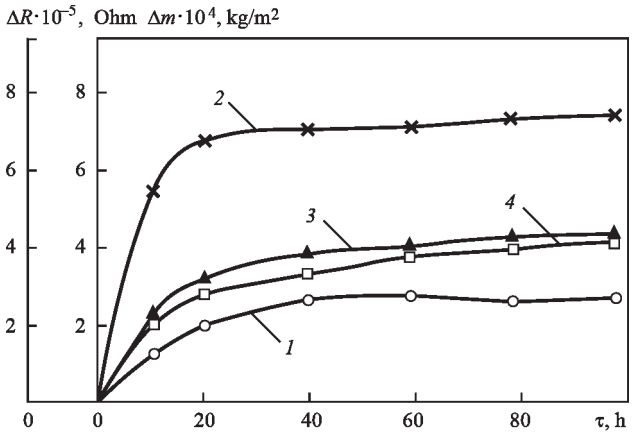

Figure 4. Change of sample weight (*1*, *2*) and electric resistance of sample surface (*3*, *4*) during corrosion testing under static (*1*, *3*) and dynamic conditions (*2*, *4*) in distilled water

The given data of gravimetric testing of copper condensates in the static and dynamic modes in distilled water showed that the greatest changes in the sample weight are observed in the initial period of corrosion testing (10–20 h) (Figure 4).

This is followed by stabilization of the corrosion processes and weight change is of a uniform nature, close to the linear one. Electron microscopy studies showed that corrosion runs uniformly over the entire sample surface. The main anode process consists in copper ionization with transition of double-charge cations into the solution;

$$Cu^0 \rightarrow Cu^{2+} + 2e^-.$$

This is confirmed by the results of chemical analysis of corrosive media after 100 h of testing (Table 2). Stabilisation of the corrosion process probably occurs due to formation on the sample surface of a thin layer of a mixture of copper oxides (I) and (II) having protective properties:

$$2Cu^0 + H_2O = Cu_2O + 2H^+ + 2e^-;$$
$$Cu_2O + H_2O = 2CuO + 2H^+ + 2e^-.$$

Application of the method of measurement of the sample electric resistance for evaluation of the corrosion processes was considered in two aspects: change of electric resistance due to formation of corrosion products on the sample surface and studying the selective dissolution of the electronegative component. As during measurement of the electric resistance the contact was made over the sample surface, and the distance between the contacts was small (6 mm),

Table 2. Chemical analysis of corrosive environments after 1000 h of testing in distilled water

Testing mode	Cu^{2+} ion content, mg/l
Before tests	0.09
Static	0.151
Dynamic	0.186

increase of the sample electric resistance can be attributed to a change of the surface layer thickness and chemical composition of the corrosion products, forming it. Electric resistance of the sample surface before corrosion testing was small and was taken to be zero. Copper oxides, particularly Cu_2O, differ by a much greater specific electric resistance, compared to pure copper. Thus, formation of protective oxide films on the sample surface is accompanied by increase in the total electric resistance of the samples.

Obtained values of measurement of the sample surface electric resistance can be used to calculate the oxide film thickness. The total electric resistance of the sample (R_{tot}) is expressed as follows:

$$R_{tot} = R_{Me} + 2R_f, \quad (1)$$

where R_{Me} is the electric resistance of that part of the sample, which was not exposed to corrosion; R_f is the additional electric resistance, allowing for the presence of corrosion products film.

Electric resistance of uncorroded part of the sample, is found from the following formula:

$$R_{Me} = \rho_{Me} L/(a \cdot b), \quad (2)$$

where ρ_{Me} is the specific electric resistance of the sample material; L is the distance between the contacts; a, b is the sample thickness and width, respectively.

As for copper $\rho = 1.72 \cdot 10^{-8}$ Ohm·m, and the distance between the contacts was selected equal to 0.005 m, then at sample thickness of 0.005 m and width of 0.001 m, its electric resistance will be very small (approximately $1.7 \cdot 10^{-5}$ Ohm·m), compared to $2R_f$. With reduction of the sample cross-section in the corrosion process, resistance R_{Me} will change only slightly. The film electric resistance is equal to:

$$R_f = \rho_f h_f / S_c, \quad (3)$$

where ρ_f is the specific electric resistance of the film; h_f is the film thickness; S_c is the contact area.

As ρ_f has large values, and $S_c = 0.000005$ m^2, the electric resistance is mainly determined by film thickness. Having jointly solved equations (1) and (3) with respect to h_f, we get

$$h_f = (R_{tot} - R_{Me})\, S_c / 2\rho_f.$$

Note that application of the derived equation is complicated for the case, when complex mixtures of corrosion products form on the sample surface, and it is impossible to assess ρ_f. Oxide film thickness calculated by this formula was equal to $3.7 \cdot 10^7$ m.

Results of measurement of the surface electric resistance agree well with gravimetric studies. Alongside a relatively fast change of weight, the initial period of corrosion is characterized by an abrupt increase of electric resistance of the sample surface, which confirms the postulate of predominant formation of copper oxide (1), having a high value of specific electric resistance.

Reduction of the dynamics of R_f change in the following testing periods points to stabilization of the film growth processes and the possibility of qualitative changes in it with formation of copper oxide (II).

Test results show that a greater reduction of the sample weight is observed under dynamic conditions, compared to the static conditions (Figure 3). Under dynamic conditions, due to greater aeration of the environment and better removal of the corrosion products, more favourable conditions are in place for running of the corrosion processes with oxygen depolarization

$$2H_2O + O_2 + 4e^- \rightarrow 4OH^-.$$

Increase of oxygen concentration in the water from 6.90 under static up to 7.34 mg/l under dynamic conditions promotes acceleration of the processes of formation of copper oxides (I) and (II), and sample movement in the environment eliminates the diffusion limitations. Increase of aeration also increases the content of CuO oxide in the film, which has higher electric conductivity, compared to Cu_2O. It is confirmed by lower values of surface electric resistance of the samples tested under the dynamic conditions, compared to static conditions.

Derived results agree with the measured values of ph and electric conductivity (æ) of environments, where corrosion tests were performed (Table 3), The given data confirm the conclusion about activisation of the corrosion processes in the dynamic mode, which is indicated by higher content of copper ions,

Table 3. Change of pH and specific electric conductivity of the environments during corrosion testing

Testing mode	Characteristic	Values after τ, h			
		0	20	50	100
Static	pH	6.41	6.29	6.53	6.81
	æ, S/m	$6.24 \cdot 10^{-4}$	$6.74 \cdot 10^{-4}$	$7.88 \cdot 10^{-4}$	$9.34 \cdot 10^{-4}$
Static	pH	6.41	6.13	6.74	7.01
	æ, S/m	$6.24 \cdot 10^{-4}$	$8.17 \cdot 10^{-4}$	$9.07 \cdot 10^{-4}$	$1.92 \cdot 10^{-3}$

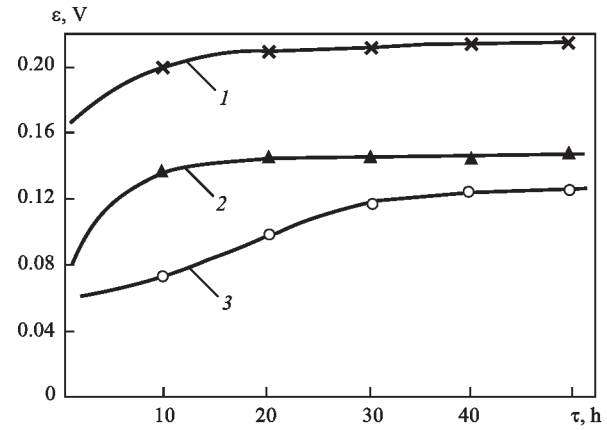

Figure 5. Influence of oxygen concentration [O_2] in distilled water on the magnitude of stationary electrode potential of copper electrodes, mg/l: *1* — 8.95; *2* — 8.67; *3* — 14.29

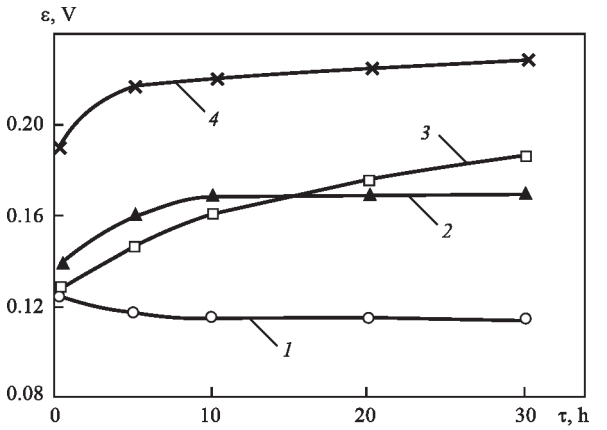

Figure 7. Influence of oxygen concentration [O_2] in tap water on the value of stationary electrode potential in copper condensates, mg/l: *1* — 2.3; *2* — 3.1; *3* — 8.11; *4* — 16.07

which are gone into the solution, and which increased the specific electric conductivity of the environment, respectively.

An important characteristic, which allows judging the kinetics of the corrosion processes, is the magnitude of stationary electrode potential (Figure 5).

Results of investigations in environments with different oxygen content show that increase of oxygen concentration shifts the stationary potential into the positive region, as a result of facilitation of running of the cathode process of oxygen reduction.

NaCl addition to distilled water rather strongly shifts the stationary electrode potential (ε = 0.018 V) to a more negative region, i.e. the corrosion processes run more intensively. It is demonstrated by the corrosion diagram for copper condensates, derived when taking the polarization curves in a potentiodynamic mode in 3 % NaCl solution (Figure 6).

The above data show that at copper condensate corrosion in a 3 % NaCl solution the controlling stage is the process of oxygen reduction running in the diffusion mode. The diffusion current under static conditions is equal to 0.631 A/m^2, and the general dissolution rate is 0.661 A/m^2 at corrosion potential of +0.04 V.

In tap water the stationary electrode potential of copper condensates largely depends on the time of water being in contact with atmospheric air. So, in fresh tap water Cu stationary potential has the highest negative value. During water settling dissolved oxygen concentration in it becomes higher, and part of the hardness salts precipitates. Here, the stationary electrode potential takes more positive values than those in the distilled water.

The influence of the above factors on the value of stationary electrode potential is given in Figure 7. Thus, increase of oxygen content in tap water, pH increase and reduction of the concentration of Ca^{2+} and Mg^{2+} ions promote shifting of the stationary electrode potential of vapour-phase condensates into the positive region.

Gravimetric studies showed that copper condensates are characterized by high corrosion resistance in tap water (Figure 8, curves *1*, *2*). However, under dy-

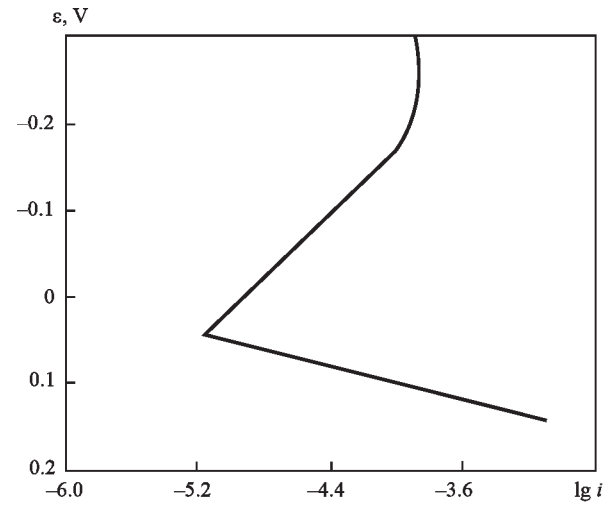

Figure 6. Corrosion polarization diagram for copper condensate in 3 % NaCl solution

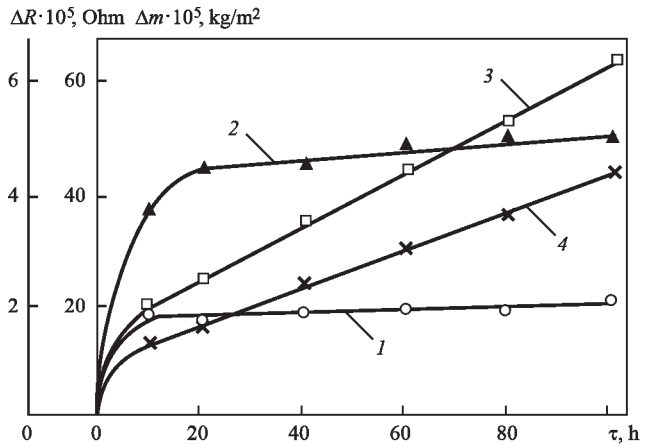

Figure 8. Change of weight (*1*, *2*) and electric resistance of sample surface (*3*, *4*) during corrosion testing under static (*1*, *3*) and dynamic (*2*, *4*) conditions in tap water

Table 4. Results of chemical analysis of tap water after 100 h of corrosion testing

Testing mode	Ion content in corrosive environment, mg/l		
	Cu^{2+}	Ca^{2+}	Mg^{2+}
Before tests	0.053	90.09	10.94
Static	0.113	86.90	10.24
Dynamic	0.162	88.01	10.73

namic test conditions weight losses exceed two times this value for static tests. The greatest weight changes are observed in the first 10 h of corrosion testing, and this is followed by process stabilization and monotonic reduction of sample weight. It follows from the layout of the curves of sample surface electric resistance that under static conditions ΔR grows more intensively, compared to dynamic conditions (Figure 8, curves *3*, *4*). This is attributable to precipitation of hardness salts on the sample surface in the absence of the environment movements, which have high values of specific electric resistance.

Under dynamic conditions, the environment movement prevents salt precipitation, and increase of electric resistance slows down. The results of electrochemical investigations, derived by taking polarization curves, confirmed deceleration of the corrosion processes in tap water, compared to distilled water (Figure 9). This is confirmed by corrosion currents, the values of which are smaller in tap water, than in distilled water, and are equal to $6.31 \cdot 10^{-3}$ A/m^2. The process of electrochemical corrosion runs in two environments with cathode control.

Gravimetric tests agree well with the data of chemical analysis of the environment after corrosion testing (Table 4).

Hardness salt content in the environment decreases in connection with formation of films on the sample surface, which include calcium and magnesium ions; copper ion concentration in the environment becomes higher, which is particularly pronounced for dynamic conditions.

CONCLUSIONS

1. Comparative studies of deposited copper, produced by electron beam evaporation and condensation and by the traditional casting method (MO grade), revealed a slight difference in electric resistance values. A certain increase in the level of deposited copper mechanical characteristic, compared to cast material, is, probably, associated with the differences in its intergranular block structure. A 1.5 times increase in hardness of condensate produced with application of

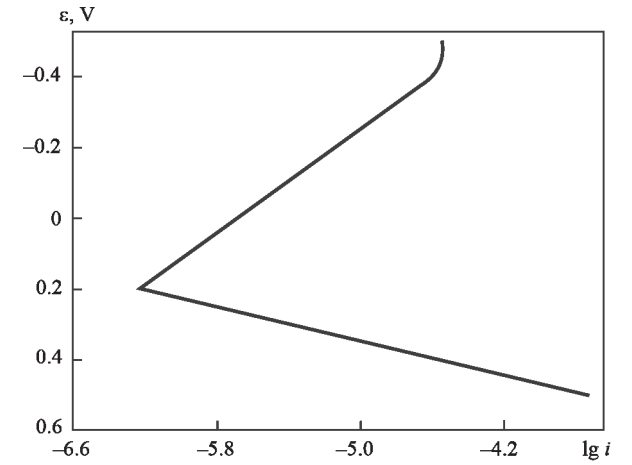

Figure 9. Corrosion polarization diagram of condensed copper in tap water

an intermediate pool, is associated with copper microalloying by zirconium and yttrium.

2. The influence of water environment on corrosion resistance of condensed copper was studied. It was found that copper corrosion in water environments proceeds by the electrochemical mechanism. Slowing down of the corrosion processes in tap water, compared to distilled water, is confirmed by gravimetric testing, data of chemical analysis of the environment after corrosion testing, and corrosion currents, the values of which are lower in tap water, than in the distilled one.

REFERENCES

1. Pradyot, P. (2002) *Inorganic compounds*. Handbook of inorganic chemicals. https://fitk.iainambon.ac.id/tadrisipa/wp-content/uploads/sites/6/2020/10/handbook-of-inorganic-chmemical.pdf
2. Hsu, Y.T., O'Reilly, B. (1977) Impurity effects in high-conductivity copper. *J. of Minerals. Metals and Materials*, **29**, 21–24.
3. Devis, J.R. (2001) *Copper and copper alloys*: ASM Specialty Handbook.
4. Chapman, D. (2011) *High conductivity copper for electrical engineering*. https://leonardo-energy.pl/wp-content/uploads/2019/03/mied%c5%b9-elektryka-raport.pdf
5. Movchan, B.A., Tikhonovsky, A.L., Kudinov, Yu.A. (1973) *Electron beam melting and refining of metals and alloys.* Kyiv, Naukova Dumka [in Russian].
6. Zolotoj, A.L. (1973) To problem of melting of copper and producing of ingots from it in electron beam furnace. *Sb. Nauch. Trudov*, **41**, 45–53, Moscow, Giredmet [in Russian].
7. (2007) *Electron beam melting in foundry.* Ed. by S.V. Ladokhyn. Stal, Kyiv [in Russian].
8. Paton, B.E., Akhonin, S.V., Berezos, V.A. (2018) Development of technologies of electron beam melting of metals at the E.O. Paton Electric Welding Institute of the NAS of Ukraine. *Suchasna Elektrometalurgiya*, **4**, 19–35. DOI: http://dx.doi.org/10.15407/sem2018.04.01
9. Grechanyuk, V.G., Grechanyuk, N.I., Chornovol, V.O. et al. (2022) Copper and molybdenum-based nanocrystalline materials. *Metallofizika i Noveishie Tekhnologii*, 44(**7**), 927–942.
10. Bukhanovski, V.V., Minakova, R.V., Grechanyuk, I.N. et al. (2011) Effect of composition and heat treatment on the struc-

ture and properties of condensed composites of the Cu–W system. *Metal Sci. and Heat Treatment*, 53(**1–2**), 14–23.
11. Grechanyuk, N.I., Konoval, V.P., Grechanyuk, V.G. (2021) Properties of Cu–Mo materials produced by physical vapor deposition for electrical contacts. *Powder Metallurgy and Metal Ceramics*, 60(**3–4**), 183–190.
12. Grechanyuk, N.I., Grechanyuk, V.G. (2018) Precipitation-strengthened and microlayered bulk copper- and molybdenum-based nanocrystalline materials produced by high-speed electron-beam evaporation-condensation in vacuum: Structure and phase composition. *Powder Metallurgy and Metal Ceramics*, 56(**11–12**), 633–646.
13. Grechanyuk, N.I., Kucherenko, P.P., Melnik, A.G. et al. (2016) New electron beam equipment and technologies for producing of advanced materials using vacuum melting and evaporation methods developed at SPE "Eltechmach". *The Paton Welding J.*, **5–6**, 48–55. DOI: http://dx.doi.org/10.15407/tpwj2016.06.08
14. Grechanyuk, N.I., Baglyuk, G.A., Kucherenko, P.P. et al. (2017) Laboratory electron-beam multipurpose installation L-2 for producing alloys, composites, coatings, and powders. *Powder Metallurgy and Metal Ceramics*, 56(**1**), 113–121.
15. Maissel, L., Glang, R. (1977) *Handbook of thin film technology*. 2nd Ed., McGraw-Hill, New York, USA.
16. Zhou, P., Kevin, O. (2018) The corrosion of copper and copper alloys. Ed. by K. Wandelt. *Encyclopedia of Interfacial Chemistry: Surface Sci. and Electrochemistry*, **6**, 478–489. DOI: http://10.1016/B978-0-12-409547-2.13429-8
17. Grechanyuk, V.G. (2006) *Physical chemistry and chemistry of silicates.* Kandor, Kyiv [in Ukrainian].

ORCID
V.G. Hrechanyuk: 0000-0002-2609-6018

CONFLICT OF INTEREST
The Authors declare no conflict of interest

CORRESPONDING AUTHOR
V.G. Hrechanyuk
Kyiv National University of Construction and Architecture of the MESU
31 Povitroflotskyi Prosp., 03037, Kyiv, Ukraine.
E-mail: eltechnic777@ukr.net

SUGGESTED CITATION
V.G. Hrechanyuk, M.I. Hrechanyuk, O.V. Khomenko, I.M. Hrechanyuk, V.I. Hots (2023) Features of the structure and physico-chemical properties of copper produced by the method of electron beam evaporation and condensation in vacuum. *The Paton Welding J.*, **3**, 26–32.

JOURNAL HOME PAGE
https://patonpublishinghouse.com/eng/journals/tpwj

Received: 21.12.2022
Accepted: 24.04.2023

DOI: https://doi.org/10.37434/tpwj2023.03.05

EFFECTIVENESS OF THE PROCESS OF PLASMA-ARC SPHEROIDIZATION OF CURRENT-CONDUCTING TITANIUM WIRE

V.M. Korzhyk, D.V. Strogonov, O.M. Burlachenko, A.Yu. Tunik, O.V. Ganushchak, O.P. Hrishchenko

E.O. Paton Electric Welding Institute of the NAS of Ukraine.
11 Kazymyr Malevych Str., 03150, Kyiv, Ukraine

ABSTRACT

The possibility of producing spherical titanium powders by application of the technology of plasma-arc atomization of compact current-conducting Ti wire of Grade 2 of 1.6 mm diameter was experimentally confirmed. Analysis of granulometric composition of the powder showed that the main fraction of the powder is 25–250 μm, making up 95 % of the total powder volume, quantity of particles of <25 μm and 250–315 μm fractions not exceeding 5 %. Parameters of the titanium powder shape were studied. It was shown that the majority of the particles are of a regular spherical shape with sphericity coefficient close to 0.8. The quantity of defective particles is not more than 3 % of the total weight of the powder. It was found that atomization by the wire-anode scheme leads to a considerable increase of wire heating efficiency (by approximately 4 times), compared to the scheme of atomization of neutral wire, which promotes an increase of process efficiency from 2–5 to 12 kg/h. It is shown that application of the technology of plasma-arc spheroidization of the titanium wire allows producing spherical powders for 3D printing of high-quality products for the aerospace industry by the technologies of selective and direct laser melting, electron beam melting and sintering and by the methods of powder (granulated) metallurgy (hot isostatic pressing with subsequent thermomechanical treatment).

KEYWORDS: plasma-arc atomization, current-conducting wire, spheroidization, titanium powder, granulometric composition<; sphericity

INTRODUCTION

In recent time due to intensive development of aerospace, shipbuilding, power, chemical and biomedical branches there is a need in repair and manufacture of volumetric parts of complex shape from titanium and its alloys using additive manufacturing technologies (3D printing) and granular metallurgy [1].

Selective and direct laser melting and sintering (SML — Selective Laser Melting, SLS — Selective Laser Sintering, DMLS — Direct Metal Laser Sintering), electron beam meting (EBM) should be referred to the main technologies of 3D printing of products from titanium and its alloys. Indicated methods are used for manufacture of such parts as components of jet and rocket engines — blades, disks of compressor and fan, fixture elements, support arms, protective shells, branch pipes; parts of airplane hulls — flaps, wing spars, frames, landing gear flaps; parts of ship power units — valves, heat-exchanger pipes, turbine components; parts of biomedical designation — surgery (dental) implants and endoprostheses etc. [2].

Hot Isostatic Pressing (HIP) [3] is the most perspective among the technologies of granular metallurgy which includes compacting of spherical particles (granules) with microcrystalline (nanocrystalline) structure, that was crystallized from a melt with high velocity, for manufacture of structural, including granular composites based on titanium alloys and titanium intermetallics with a complex of improved physical-chemical characteristics. HIP allows creating the materials with previously set properties due to formation of combinations of granules of different chemical, phase and fractional content in necessary proportions. Such granular composites are perspective for manufacture of parts of aeronautical and automotive engineering (compressor blades of gas-turbine engines, valves of gas distribution, parts of hydraulica, liners, pistons etc.).

Specialized spherical titanium powders with high requirements to their grain-size composition, shape, mechanical and technological properties are used in these methods as consumables for formation of additive layers and granular compositions. For example, powders of narrow fraction of 25–45 μm are used for SLM process, 45–106 μm for EBM, 45–150 μm for DMLS and 106–250 μm for HIP technology [4]. Besides, these powders should have low content of gas blends (oxygen — not more than 0.15 wt.%, hydrogen — not more than 0.01 wt.%) and high technological properties (flowability, yield, apparent density, sphericity coefficient et al.) The powders for HIP should have high apparent density and yield for provision of high density of packaging and further pressing, absence of inner defects (pores) as well as microcrystalline (in some cases nanocrystalline)

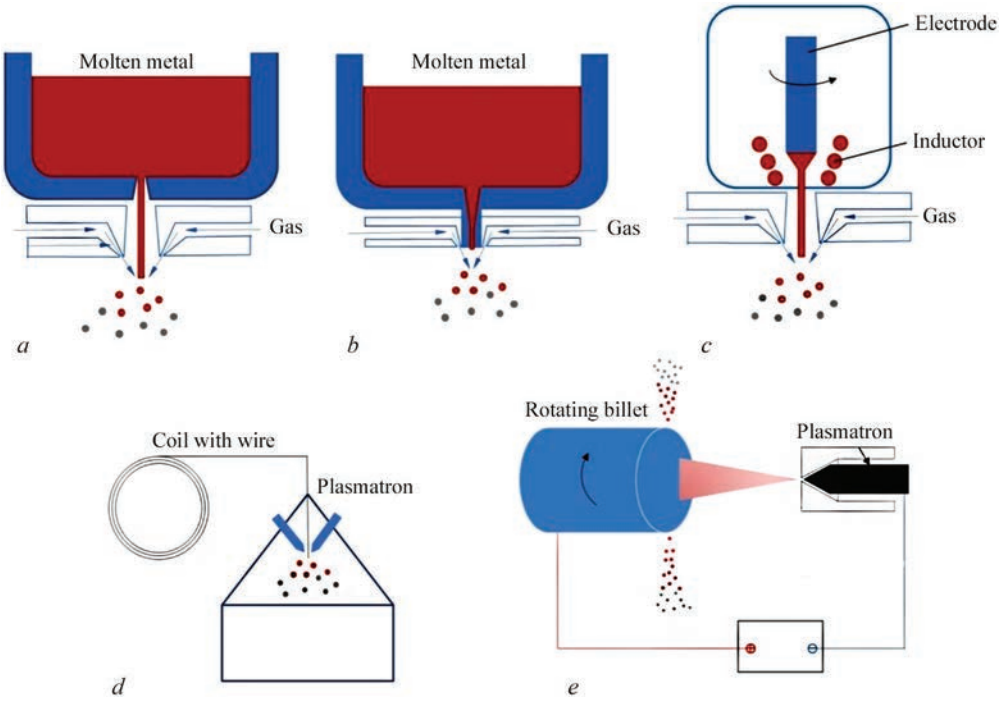

Figure 1. Schemes of atomization process: *a* — FFGA; *b* — CCGA; *c* — EIGA; *d* — PREP [1]

structure which is formed at ultra-high cooling velocities (10^4–10^6 °C/s) and provides increased mechanical properties of finished product [5].

ANALYSIS OF REFERENCE DATA AND PROBLEM STATEMENT

The general practice of production of such powders includes the following technologies (Figure 1): FFGA — Free Fall Gas Atomization, CCGA — Close Coupled Gas Atomization, EIGA — Electrode Induction Gas Atomization, PREP — Plasma Rotating Electrode Process, PA — Plasma Atomization [6].

Table 1 provides the key peculiarities of mentioned above methods of atomization and characteristics of produced powders [7].

The most widespread methods of production of spherical powders of titanium are GA and PREP technologies [8]. However, regardless the presence of large number of advantages they have a series of disadvantages, to which it is necessary to include: GA — relatively low coefficient of sphericity; presence of defective satellite particles and often non-spherical shape, closed argon pores et. al.; PREP — difficulty

Table 1. Peculiarities of different methods of production of spherical powders

Production method	Output material	Grain-size composition	Efficiency	Powder morphology	Powder characteristics
FFGA/CCGA	Preliminary prepared melt	Size of particles 25–500 μm, percent of fine fraction <100 μm up to 40 wt.%	Up to 100 kg/8 h	Shape is almost spherical, sphericity coefficient 0.6–0.7	Presence of satellites, non-spherical particles and particles with pores and inclusions <15 wt.%
EIGA	Precision-machined cylinder billets	–	–	Shape is almost spherical, sphericity coefficient <0.7	Presence of satellites, non-spherical particles and particles with pores <10 wt.%
PA	Wire materials, rods	Size of particles 25–300 μm, percent of fine fraction <100 μm up to 40–50 wt.%	–	Shape is spherical, sphericity coefficient <0.8	Presence of satellites, non-spherical particles and particles with argon pores <5 wt.%
PREP	Precision-machined cylinder billets	Size of particles 50–500 μm, percent of fine fraction <100 μm up to 20 wt.%	Up to 150 kg/ 8h	Shape is spherical, sphericity coefficient <0.9	Complexity of fraction production <50 μm, presence of particles with tungsten inclusions <1.5 wt.%

of production of powders <100 μm, problems related with production of cylindrical billet with accurate dimensions, complexity of kinematic scheme of this equipment, need of its operation at ultra-high velocities of billet rotation assemblies (20000–40000 rpm), difficulties appearing at that.

A significant potential to further development and practical application for production of spherical powders from titanium and highly-alloyed titanium alloys lies in a technology of plasma-arc spraying of wires or rods, one of the varieties of which is PA process mentioned above [9]. The advantage of this technology is the large number of technological parameters which allows regulation of grain-size composition of powder in wide limits as well as possibility of application of wide range of standard consumables from solid wires and rods [10].

It is known that there are two types of the process of plasma-arc spraying of wire (rod), namely the schemes using as a filler material neutral and current-conducting wires (wire-anode) [10]. Because the technology of plasma-arc spraying is only on the stage of industrial implementation the most widespread method is atomization of neutral wire. However, this method has a significant drawback — low efficiency. The researchers from work [11] used a complex of three plasma torches, for spraying of titanium wire Ti6Al4V, which provide total efficiency at 2–5 kg/h level. At that total electric power into wire makes from 20 to 90 kW, i.e. specific electric power for production of 1 kg of titanium wire makes not less than 10 kW·h. A variant of increase of technical-economic parameters of the process can be application of a technology of plasma-arc spraying of current-conducting wires that allows significantly rising efficiency of heating process and wire melting.

AIM AND TASKS OF INVESTIGATION

The aim of work is the analysis of possibility and evaluation of perspectives of application of the process of plasma-arc spraying of current-conducting wires for production of spherical titanium powders, including in comparison with a variant of neutral wire spraying. To reach the aim it is necessary to study a grain-size composition and parameters of sphericity of titanium powder, produced using a technology of plasma-arc spraying in water of current-conducting wire of Ti Grade 2; carry an analysis of efficiency of process of heating of current-conducting titanium wire; provide the recommendations as for practical application of spherical powders of titanium and titanium alloys produced in the process of plasma-arc spraying.

MATERIALS AND INVESTIGATION PROCEDURE

An essence of the process of plasma-arc spraying lies in melting of current-conducting wire-anode which is entered in a zone of high-velocity plasma jet and further breaking of a melt separating from a wire end [12]. An arc burns between nonconsumable tungsten cathode and current-conducting wire-anode being fed behind an edge of plasmatron nozzle. Working (plasma-forming) gas coming into operating chamber is heated using electric arc and comes out from a nozzle in form of plasma-forming jet. Open section of discharge behind the plasma-forming nozzle is blown by gas flow coming out of a circular gap between the plasmatron nozzles. The peculiarity of this method is the fact that melting and jet spraying of wire material is carried out by argon plasma and concurrent gas prevents expansion of open section of a plasma jet. This allows reducing an angle of its opening due to constriction of the plasma jet with concurrent gas flow that provides it acceleration and increase of gas-dynamic pressure on wire edge and promotes production of optimum fractional composition of dispersed phase.

Technological experiments were carried out in open atmosphere using plasma-arc spraying unit PLAZER-30 [13], in which current-conducting electrode wire was used as consumable anode (Figure 2). In order to capture sprayed titanium particles the wire was sprayed in a water-filled vessel from 500 mm distance.

Indicated technological equipment was used for investigation of grain-size composition of particles in spraying of wire-anode from commercial titanium corresponding to Ti Grade 2, USA (analog of VT1-0 grade GOST 19807–91) of 1.6 mm diameter.

Ti Grade 2 titanium wire of 1.6 mm diameter has the next composition, wt.%: Fe — <0.25; C — < 0.07; Si — 0.10; N — <0.04; O — 0.020; H — < 0.01; Ti —base and thermodynamic and thermophysical properties of commercial titanium (VT1-0 grade [15] are:

melting temperature (T_{ml}), K	1945
boiling temperature (T_{boi}), K	3560
melting heat (λ), J/kg	$3.58 \cdot 10^5$
evaporation heat (L_{eva}), J/kg	$8.97 \cdot 10^6$
heat capacity of titanium (C_p) at 1945 K, J/kg·K	989.2
enthalpy of titanium (H) at heating from 298 to 1945 K (liquid titanium), J/kg	$3.15 \cdot 10^5$

An optimum mode was selected according to earlier obtained practical data, by criterion of visual evaluation of shape of plasma jet, at reaching its minimum opening angle and stability of the process. Following it the changes of mode parameters were introduced for discovering the effect of each of them on change of particle fractional composition. Argon of high

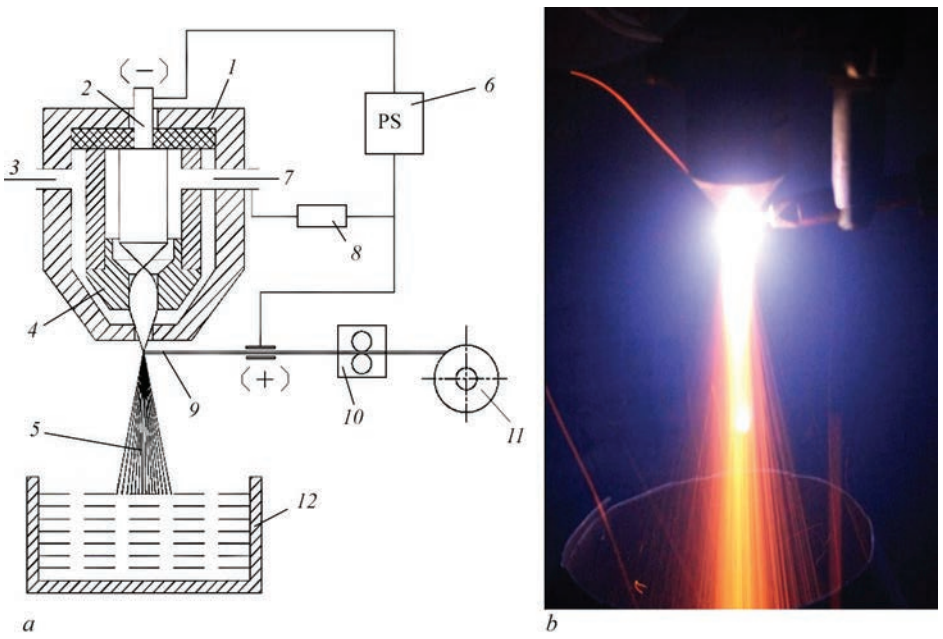

Figure 2. Scheme of the process of plasma-arc spraying and spheroidization of current-conducting wire (*a*) and appearance of spraying process (*b*): *1* — plasmatron operating chamber; *2* — tungsten electrode (cathode); *3* — channel for concurrent gas supply; *4* — plasma-forming nozzle; *5* — jet of particles being sprayed; *6* — power source; *7* — channel for supply of plasma-forming gas; *8* — current-limiting resistance; *9* — wire-anode; *10* — feeding mechanism; *11* — coil with wire; *12* — fridge with water [14]

grade I1 according to ISO 14175–2008 "Welding consumables. Gases and gas mixtures for fusion welding and allied processes" was used as a plasma-forming gas, air was used as a concurrent gas.

Spraying was carried out at the following process parameters, namely current — 250 A, consumption of plasma-forming gas — 30 l/min, wire feed rate — 10.5 m/min, cathode-anode distance — 8 mm.

Selection of the samples for examination of grain-size composition of a powder, morphology of surface et al. was carried out using laboratory vibroshaker Analyzzette 3 Spartan (Germany) with a set of sieves 25–500 μm, weight of sample made less than 100 g of powder. Grain-size composition of laboratory batches of powder was determined using the method of sieve analysis according to procedure ISO 25911:1988 "Test sieving. Pt 1: Methods using test sieves of woven wire cloth and perforated metal plate" with the help of vibroshaker Analyzzette 3 Spartan with a set of sieves 25–40, 40–63, 63-80, 80–100, 106–125, 125–160, 160–200, 200–250, 250–315, 315–400, 400–450, 450–500 μm. Shape of particles, their microstructure were investigated using the methods of light (microscope Neophot-32 (Germany) and analytical scanning electron (microscope PHILIPS SEM-515, Netherlands) microscopy. Description of shape of particles was carried out by a procedure from standard ISO 9276-6:2008 "Representation of results of particle size analysis — Pt 6: Descriptive and quantitative representation of particle shape and morphology".

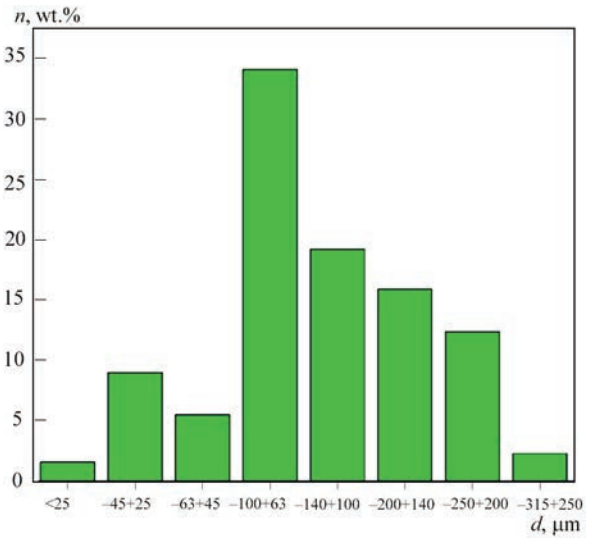

Figure 3. Grain-size composition of titanium powder produced in process of plasma-arc spraying of current-conducting wire of Ti Grade 2

INVESTIGATION RESULTS

INVESTIGATION OF GRAIN-SIZE COMPOSITION AND PARAMETERS OF SPHERICITY OF TITANIUM POWDER

Examination of grain-size composition of particles (Figure 3) showed that in spraying of current-conducting compact wire Ti Grade 2 in water the main fraction is 25–250 μm fraction which makes 95 % of total powder weight. At that amount of particles of fraction <25 μm and 250–315 μm at this mode of spraying does not exceed 5 %.

Portion of 25–45 μm fraction from total weight of powder makes 9.2 wt.%, 45–100 — 39.6; 45–140 — 58.6; 100–250 — 47.5.

Investigation of powder shape showed that powder in general has regular spherical shape (Figure 4) at that a sphericity coefficient makes 0.76.

Typical defects in produced powder are satellites, oxidized particles and particles of irregular shape, portion of which approximately makes not more than 3 wt.%.

It is necessary to note that wire spraying and formation of jet from overheated particles and their further solidification was carried out on air and in water, where processes of intensive chemical interaction of titanium with oxygen, nitrogen and hydrogen take place. The latter can provoke deterioration of parameters of powder sphericity. Similar effect appears in spraying of another chemically active metal–aluminium. The authors of work [16] explain this by formation of a dense oxide layer on the surface of particles in process of their spheroidization and solidification that results in decrease of surface tension force of molten metal and promotes formation of irregular shape particles. In work [17] it is noted that plasma-arc spraying of wire in chambers with inert atmosphere allows producing powder a coefficient of sphericity of which can reach approximately 0.90. Therefore, increase of parameters of sphericity of particles can be reached due to creation of inert atmosphere in a medium where processes of spraying, dispersion and solidification of powders take place.

EVALUATION OF PERFORMANCE FACTOR AND EFFICIENCY OF PROCESSES OF HEATING OF CURRENT-CONDUCTING AND NEUTRAL WIRE WITH PLASMA ARC IN TITANIUM WIRE SPRAYING

Calculation of the processes of heating and melting of wire was carried out using approximated method of V.V. Kudinov [10]. At that the following assumptions were made: anode spot, located on wire, promotes evaporation of 2 wt.% from weight of used wire (based on experimental investigations it was discovered that in spraying of neutral wire in water weight of gathered powder by 4 wt.% less the weight of sprayed wire and in spraying of current-conducting wire this value makes almost 6 wt.%; temperature of liquid drops in a place of melt formation at wire edge equals a metal melting temperature (temperature of particles in a zone of melt formation was measured using optical pyrometer and it was discovered that their temperature exceeds metal melting temperature by 200–300 °C, therefore this overheating was neglected and it was assumed that wire in a zone of spraying is heated to melting temperature); a coefficient of total heat emission from gas to wire was determined based on a heating mode and rate of neutral wire melting (at that a mode of wire heating was determined in such a way that weight-average temperature of plasma in spraying of neutral wire equaled weight-average temperature of plasma in current-conducting wire spraying).

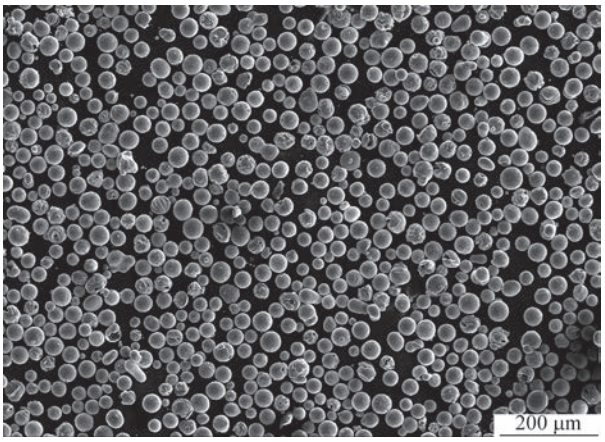

Figure 4. Morphology of powder of 25–45 μm fraction produced by technology of plasma-arc spraying of compact current-conducting wire of Ti 2 Grade into water

There was calculated a total balance of power on wire-anode being heated with plasma arc:

$$q_{\text{h}} + q_{\text{e}} + q_{\text{J}} = q_{\text{ml}} + q_{\text{eva}}, \qquad (1)$$

where q_{h} is the power being transferred to wire due to radiant and convective heat exchange with gas jet; q_{e} is the power being transferred to wire from electrons; q_{J} — power being emitted in wire stick-out at current passing; $q_{\text{ml}} + q_{\text{eva}}$ — power used for heating, melting and evaporation of wire.

Weight-average temperature of gas in a nozzle channel of plasmatron was calculated by the following formula [10]:

$$T_{\text{Ar}} = \frac{I[U - (U_{\text{c}} + U_{\text{a}})]}{\pi d_{\text{n}} \alpha_{\text{n}} l_{\text{a}}} \left(1 - e^{-\frac{\pi d_{\text{n}} \alpha_{\text{n}} l_{\text{a}}}{c_{\rho} \vartheta}}\right), \qquad (2)$$

where I is the current, A; U is the arc voltage, V; d_{n} is the nozzle diameter, m; ϑ is the argon consumption (mass velocity), kg/s; l_{a} is the arc length, m; $U_{\text{c}} + U_{\text{a}}$ is the sum of cathode and anode voltage drop that equals 7 V; α_{n} is the coefficient of heat exchange between gas and nozzle channel, $\alpha_{\text{n}} = 8.38 \cdot 10^2$ W/m^2·K; c_{ρ} is the specific heat of argon which can be considered constant and equal $11.3 \cdot 10^2$ J/kg·K in temperature interval 8000–12000.

In case of spraying of current-conducting wire the arc current made 250 A, arc voltage — 65 V, argon consumption (mass velocity) — $1.49 \cdot 10^{-3}$ kg/s, nozzle diameter — $3 \cdot 10^{-3}$ m, nozzle length — $2 \cdot 10^{-3}$m,

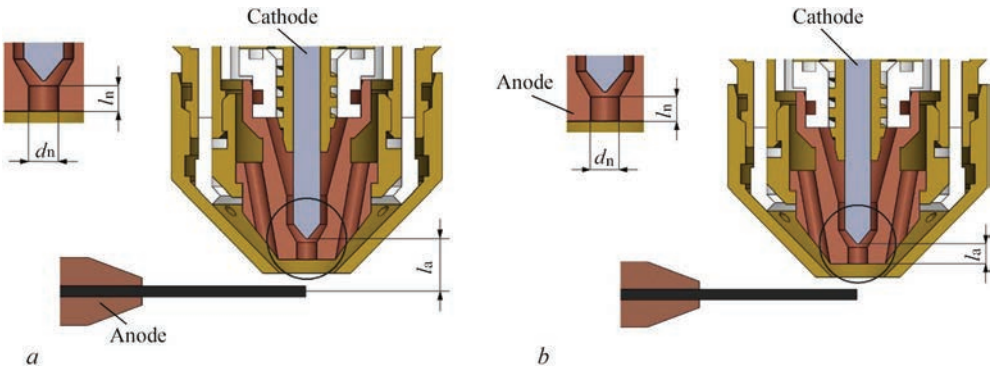

Figure 5. Structural parameters of plasmatron, mm: *a* — in spraying of current-conducting wire (l_a = 7; d_n = 3; l_n = 2); *b* — in spraying of neutral wire (l_a = 3; d_n = 3; l_n = 2

arc length — $7 \cdot 10^{-3}$ m (Figure 5), plasma jet melted $3.3 \cdot 10^{-3}$ kg/s of titanium wire of Ti Grade 2 of 1.6 mm diameter.

In case of spraying of neutral wire the different parameters were: arc current — 380 A, arc voltage — 45 V and its length — $3 \cdot 10^{-3}$ m (Figure 5). This provided the same weight-average temperature of argon plasma for both cases and respectively similar power being transferred from plasma to wire. Based on experimental data it was taken that in such mode of operation the plasma jet melts 4 kg/h ($1.1 \cdot 10^{-3}$ kg/s) of neutral titanium wire of Ti Grade 2 of 1.6 mm diameter.

The next empirical formula was proposed by the authors to determine power being transferred due to heat exchange with gas jet in melting of neutral wire:

$$q_h = V_{ml}(\lambda + H) = 1.1 \cdot 10^{-3} \cdot (3.58 \cdot 10^5 + 3.15 \cdot 10^5) = 741 \text{ W},$$

where V_{ml} is the rate of melting of neutral titanium wire ($1.1 \cdot 10^{-3}$ kg/s); λ is the heat of titanium melting ($3.58 \cdot 10^5$ J/kg); H is the enthalpy of titanium in heating from 298 to 1945 K ($3.15 \cdot 10^5$ J/kg) (see thermodynamic and thermophysical properties of titanium).

The results obtained by the authors based on experimental investigations [10] showed that heat exchange between gas and wire appears in a section $d_n/2$ (Figure 6), where wire is heated from room temperature to temperature of metal melting (T_{ml}). At that the

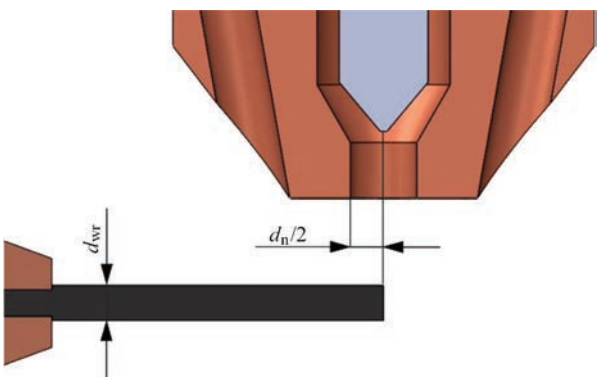

Figure 6. Structural parameters of plasmatron (mm) in determination of surface of heat exchange with gas jet: d_n = 3; d_{wr} = 1.6

authors made an assumption that wire in the section $d_n/2$ has average temperature $T_{wr} = T_{ml}/2$.

Then power being transferred to wire due to heat exchange with gas jet is determined by formula:

$$q_h = F\alpha_h \left(T_{Ar} - T_{wr}\right), \quad (3)$$

where F is the area of surface heat exchange, m^2; α_h is the coefficient of complete heat emission from gas to wire, W/m^2; T_{Ar} is the weight-average temperature of argon plasma, K; T_{wr} is the wire temperature, K.

Area of surface heat exchange is determined:

$$F = \frac{\pi d_{wr}^2}{4} + \pi d_{wr} \frac{d_n}{2}, \quad (4)$$

where d_{wr} is the wire diameter which equals $1.6 \cdot 10^{-3}$ m; d_n is the nozzle diameter which equals $3 \cdot 10^{-3}$ m.

Power being transferred to wire from electrons is determined:

$$q_e = I\left(U_{a(Ar)} + \varphi\right), \quad (5)$$

where I is the current passing through wire, A; $U_{a(Ar)}$ is the value of anode voltage fall for wire metal in argon (2.5 V); φ is the work of electrons output for anode metal (3.9 V).

Power being emitted in wire stick-out at current passing is described by formula:

$$q_J = I^2 \frac{\rho l}{S}, \quad (6)$$

where I is the current passing through wire, A; ρ is the electric resistance of conductor with current for titanium equals $1.68 \cdot 10^{-6}$ Ohm·m; l is the length of conductor (distance from current contact jaw place); l = 0.01 m; S is the area of wire cross section of 1.6 mm diameter which equals $2.6 \cdot 10^{-6}$ m^2.

Since spraying of current-conducting wire promotes evaporation of 2 % from total powder weight,

the velocity of titanium evaporation is determined by equation: $V_{eva} = V_{ml} \cdot \%_{eva} = 6.6 \cdot 10^{-5}$ kg/s.

The authors proposed the next empirical formula for determination of power being used for wire material evaporation:

$$q_{eva} = V_{eva} L_{eva} = 6.6 \cdot 10^{-5}\ 8.97 \cdot 10^{6} = 592 \text{ J},$$

where V_{eva} is the velocity of titanium evaporation in spraying of current-conducting wire ($6.6 \cdot 10^{-5}$ kg/s); L_{eva} is the heat of evaporation ($8.97 \cdot 10^{6}$ J/kg).

Total amount of heat embedded in wire in process of plasma-arc spraying is determined by the next formula:

$$q_{tot} = \eta IU. \quad (7)$$

There was calculated a contribution of each constituent in a total balance of power on titanium wire-anode at arc power 16 kW. The results of calculation are given in Table 2.

In case of heating with plasma arc of neutral titanium wire the efficiency equals:

$$\eta = \frac{741}{380 \cdot 45} \approx 4\ \%,$$

and in spraying of current-conducting titanium wire:

$$\eta = \frac{2744}{250 \cdot 65} \approx 17\ \%.$$

Carried experimental investigations showed that efficiency of the method of plasma-arc spraying of current-conducting titanium wire of 1.6 mm diameter of Ti Grade 2 in a range of utilized power of plasmatron 15–20 kW is at a level of 10–12 kg/h. Efficiency of the method of plasma-arc spraying of neutral wire of 3.2 mm of Ti6A14V grade according to reference data can make approximately 2.5 kg/h at plasmatron power about 28 kW [18] and up to 5 kg/h at power up to 90 kW [19]. Also it is necessary to note that for PREP technology of plasma spheroidization of rods of Ti6A14V grade alloy of 75 mm diameter the process efficiency makes approximately 12.5 kg/h at utilized power 38 kW [20].

Thus, the process of plasma-arc spraying of current-conducting wire-anode is characterized by 4.25 times higher values of efficiency in comparison with plasma-arc spraying of neutral filler wire that significantly effects the process efficiency, the maximum values of which can reach 12 kg/h for utilized power 20 kW. Further increase of efficiency of this process is achieved by means of increase of electric power of sources, plasmatron and equipment for plasma-arc spraying of current-conducting wires.

The calculations show that increase of power of this equipment from 15–20 kW could provoke increase of efficiency index of the process up to 18–20 kg/h. In general, capabilities of plasma equipment allow rising power to 100–120 kW that provides the possibility to use for spraying wires as well as rods of 3–6 mm diameter and larger and to greater extent increase the efficiency indices of the process of production of spherical titanium powders.

Table 2. Total balance of power on wire-anode

Balance item	Power, W	Relative balance value, %
Obtained wire power:	1600	~58
from electrons		
at heat exchange with plasma jet	741	~27
in current passing	403	~15
Total	2744	100
Power spent for:		
heating and melting of wire	2172	~79
wire evaporation	572	~21
Total	2744	100

ANALYSIS OF INVESTIGATION RESULTS

Analysis of the results of investigations of grain-size composition of the products of plasma-arc spraying of current-conducting Ti Grade 2 wire showed that they mainly present themselves spherical powders with particles of 25–250 μm size. Portion of main fractions from total weight of produced powder, which correspond to the requirements of different methods of 3D printing makes: 45–106 μm — 39.6 % (EBM); 45–140 μm — 58.6 % (DMLS); 106–250 μm — 47.5 (HIP).

Investigation of a shape of titanium powder particles showed that in general the particles have regular spherical shape with coefficient of sphericity (S_{sph}) 0.76 at small quantity of defective particles (<3 wt.%). However, in this aspect it is necessary to note that plasma-arc spraying of titanium wire was carried out in air atmosphere with further crystallization into water. During this process a wire end melting and dispersion of a melt take place in argon plasma, hardening and shaping of particles of powders occur in air atmosphere and in water that can be a factor effecting formation of indicated portion of particles of imperfect spherical shape.

Investigation of the processes of heating of current-conducting wire showed that the main source of wire heating is current that makes approximately 58 % of total power embedded into wire. At this efficiency of heating of current-conducting wire is almost 4 times greater in comparison with heating of neutral wire that is revealed in increase of process efficiency from 2–5 to 12 kg/h. Rapid rise of efficiency of wire heating with plasma arc in comparison with plasma jet can be explained by partial change of heating pro-

cess from heat exchange to mechanism of electron bombardment, when electrons passed an arc column are slowed down in anode area forming excessive negative charge and deposit on anode giving their energy to it [21].

Also it is necessary to note that the index of specific energy consumption for production of 1 kg of titanium powder using the technology of plasma-arc spraying of current-conducting wire makes 1.5–1.7 kW·h/kg. It is considerably lower index in comparison with other commercial technologies of plasma spraying — spraying of neutral wire, where the values of index of specific power consumption can vary in wide limits depending on characteristics of equipment and make 11 kW·h/kg at plasmatron power 28 kW or 18 kW·h/kg at total power of three plasmatrons 90 kW. For PREP technology a specific utilized power for production of 1 kg of titanium powder makes around 3 kW·h/kg. At that it is necessary to consider that investigations in this work were carried out by the example of titanium wire of 1.6 mm diameter. Using of the larger diameter wires in this process has a potential of further decrease of specific energy efficiency.

Obtained results of grain-size composition and sphericity parameters of powder allow recommending the technology of plasma-arc spheroidization of current-conducting wire for production of spherical powders (granules) of titanium and titanium alloys for 3D printing using the methods of direct laser and electron-beam melting as well as with the help of the methods of powder metallurgy. Analysis of grain-size composition of content of particles showed that for application of titanium powders in selective laser melting and sintering it is necessary to carry out further investigations on optimization of the modes of plasma-laser spraying of wire for the purpose of increase of portion of 25–45 μm fraction in the total powder volume. Also it is necessary to note that the significant portion of fraction of produced powder on size and coefficient of sphericity correspond to the requirements to materials for technology of compacting in granular metallurgy, particularly, for HIP process (106–250 μm). Especially, indicated powders, produced at ultra-high cooling velocities, create the conditions for formation of microcrystalline (and in some cases nanocrystalline) structure that has positive effect on mechanical properties of products made of them.

CONCLUSIONS

1. By the example of titanium wire Ti Grade 2 of 1.6 mm diameter there were proved the perspectives of application of technology of plasma-arc spraying of current-conducting wire for production of spherical powders from titanium and titanium alloys. It was determined that in plasma-arc spheroidization of current-conducting titanium wire the main fraction is 25–250 μm fraction which makes 95 % of total weight of powder, number of particles of fraction <25 and 250–315 μm under optimum modes of spraying is at sufficiently low level and does not exceed 5 %. In total, the particles have regular spherical shape with index of sphericity coefficient close to 0.8 at small number of defective particles (< 3 wt.%).

2. It was grounded an increase power efficiency of the process of plasma-arc spraying of current-conducting wire-anode, which in comparison with plasma-arc spraying of neutral filler wire is characterized with 4.25 times greater values of efficiency and 1.5–6.0 times index of maximum process productivity 12 kg/h at 20 kW and 2–5 kg/h, respectively, in case of index of utilized electric power 20–90 kw) and smaller specific energy consumption (1.6 kW·h/kg for plasma-arc spraying of current-conducting wire and 11–18 kW·h/kg for neutral one). Also this technology has the advantages on indices of efficiency and specific energy consumption over the PREP process (3 kW·h/kg), which is used in industry for production of titanium powders of spherical shape.

3. Obtained results allow considering plasma-arc spheroidization of current-conducting wire as an effective technology for production of powders (granules) of spherical shape from titanium and titanium alloys that correspond to the requirements to materials for 3D printing of high-quality products using the methods of selective and direct laser melting and sintering, electron-beam melting as well as requirements to materials for granular metallurgy (production of high-quality structural materials by means of compacting of particles (granules) with microcrystalline structure that was crystallized from melt with high velocity).

REFERENCES

1. Sun, P., Fang, Z., Zhang, Y. et al. (2017) Review of the methods for the production of spherical Ti and Ti alloy powder. *JOM*, **69**, 1853–1860. DOI: https://doi.org/10.1007/s11837-017-2513-5
2. Fang, Z., Paramore, J., Sun, P. et al. (2018) Powder metallurgy of titanium — past, present, and future. *Inter. Materials Reviews*, 63(**7**), 407–459. DOI: https://doi.org/10.1080/09506608.2017.1366003
3. Kim, K.T., Yang, H.C. (2013) Densification behavior of titanium alloy powder under hot isostatic pressing. *Powder Metallurgy*, 44(**1**), 41–47. DOI: https://doi.org/10.1179/003258901666158
4. Yanko, T.V., Ovchinnikov, A.V., Korzhyk, V.N. et al. (2018) Technological scheme for producing of titanium alloy powders of aircraft purpose for 3D-printing. *Tekhnologicheskie Sistemy,* **4**, 36–41 [in Russian]. DOI: https://doi.org/10.29010/085.7

5. Kim, Y. et al. (2014) Microstructure and mechanical properties of hot isostatically pressed Ti–6Al–4V alloy. *J. of Alloys and Compounds*, **603**, 207–212. DOI: https://doi.org/10.1016/j.jallcom.2014.03.022
6. Yim, S., Bian, H., Aoyagi, K., Yamanaka, K. (2021) Spreading behavior of Ti48Al2Cr2Nb powders in powder bed fusion additive manufacturing process: Experimental and discrete element method study. *Additive Manufacturing*, **73**, 337–353. DOI: https://doi.org/10.1016/j.addma.2021.102489
7. Chen, G., Zhao, S., Tan, P. et al. (2018) A comparative study of Ti6Al4V powders for additive manufacturing by gas atomization, plasma rotating electrode process and plasma atomization. *Powder Technology*, **333**, 38–46. DOI: https://doi.org/10.1016/j.powtec.2018.04.013
8. Nie, Y., Tang, J., Teng, J. et al. (2020) Particle defects and related properties of metallic powders produced by plasma rotating electrode process (PREP). *Advanced Powder Technology*, **31**, 2912–2920. DOI: https://doi.org/10.1016/j.apt.2020.05.018
9. Smirnov, S.A., Kirsankin, A.A., Kalaida, T.A. (2022) Properties of the spherical titanium VT1-00 powder fabricated by plasma atomization of a wire. *Metall*., **4**, 741–745. DOI: https://doi.org/10.1134/S0036029522070126
10. Kudinov, V.V. (1966) *Heating of current-conducting wire by constricted arc* [in Russian].
11. Kang, I.J., Park, H.J., Cho, C.H. et al. (2021) Development of a plasma and gas hybrid atomization system for the production of metal powder materials. *J. of the Korean Physical Society*, **79**, 1141–1150. DOI: https://doi.org/10.1007/s40042-021-00341-6
12. Korzhyk, V.M., Khaskin, V.Yu., Yao Yuhui et al. (2022) Influence of accompanying compressing air flow on the coating structure and properties in plasma-arc spraying by consumable current-conducting wire. *The Paton Welding J.*, **2**, 3–10. DOI: https://doi.org/10.37434/tpwj2022.02.01
13. Korzhik, V.N., Korob, M.F. (2012) Mechanized line PLAZER 30PL-W for plasma-arc wire surfacing of coatings on large-sized parts of "shaft" type. *Svarshchik,* **4**, 13–15 [in Russian].
14. Strogonov, D.V., Korzhyk, V.M., Jianglong, Yi et al. (2022) Influence of the parameters of the process of plasma-arc spheroidization of current-conducting wire from low-carbon steel on the granulometric composition of the produced powders. *Suchasna Elektrometalurhiya*, **3**, 29–37 [in Ukrainian]. DOI: https://doi.org/10.37434/sem2022.03.05
15. Desai, P.D. (1987) Thermodynamic properties of titanium. Inter. *J. Thermophys*, **8**, 781–794.
16. Dietrich, S., Wunderer, M., Huissel, A., Zaeh, M. (2016) A new approach for a flexible powder production for additive manufacturing. *Procedia Manufacturing*, **6**, 88–95. DOI: https://doi.org/10.1016/j.promfg.2016.11.012
17. Kalayda, T.A., Kirsankin, A.A., Ivannikov, A.Yu. et al. (2021). The plasma atomization process for the Ti–Al–V powder production. *J. Phys. Conf. Ser*., **1942**, 012046. DOI: https:doi.org/10.1088/1742-6596/1942/1/012046
18. Yin, Z., Yu, D., Zhang, Q. et al. (2021) Experimental and numerical analysis of a reverse-polarity plasma torch for plasma atomization. *Plasma Chem. Plasma Process*, **41**, 1471–1495. DOI: https://doi.org/10.1007/s11090-021-10181-8
19. *Producing the most spherical, pure titanium powders*. https://www.pyrogenesis.com/wp-content/uploads/2019/09/Project_Producing-the-Most-Spherical-Pure-Titanium-Powders.pdf
20. *LargeScale PREP System*. (SLPAH). https://prep-system.com/slpa-h/
21. Bykovskyi, O.G. (2021) *Welding, cutting and quality control during production of metal structures.* Kyiv, Osnova [in Ukrainian].

ORCID
V.M. Korzhyk: 0000-0001-9106-8593,
D.V. Strogonov: 0000-0003-4194-764X,
O.M. Burlachenko: 0000-0003-2277-4202,
A.Yu. Tunik: 0000-0001-6801-6461,
O.V. Ganushchak: 0000-0003-4392-6682,
O.P. Hrishchenko: 0000-0003-2640-8656

CONFLICT OF INTEREST
The Authors declare no conflict of interest

CORRESPONDING AUTHOR
V.M. Korzhyk
E.O. Paton Electric Welding Institute of the NASU
11 Kazymyr Malevych Str., 03150, Kyiv, Ukraine.
E-mail: vnkorzhyk@gmail.com

SUGGESTED CITATION
V.M. Korzhyk, D.V. Strogonov, O.M. Burlachenko, A.Yu. Tunik, O.V. Ganushchak, O.P. Hrishchenko (2023) Effectiveness of the process of plasma-arc spheroidization of current-conducting titanium wire. *The Paton Welding J*., **3**, 33–41.

JOURNAL HOME PAGE
https://patonpublishinghouse.com/eng/journals/tpwj

Received: 30.02.2023
Accepted: 24.04.2023

DOI: https://doi.org/10.37434/tpwj2023.03.06

APPLICATION OF CORED GRAPHITIZED ELECTRODES IN ELECTRIC ARC FURNACES OF DIRECT CURRENT (EAF DC)

A.G. Bogachenko[1], D.D. Mishchenko[1], I.A. Honcharov[1],V.I. Braginets[1], I.A. Neylo[1], Y.A. Plevako[2]

[1]E.O. Paton Electric Welding Institute of the NAS of Ukraine
11 Kazymyr Malevych Str., 03150, Kyiv, Ukraine
[2]PJSC "Ferrotrading"
7 Teplychna Str., 69009, Zaporizhzhya, Ukraine

ABSTRACT

An effective means for improvement of technical and economic indicators of EAF DC are graphitized cored electrodes, designed at the E.O. Paton Electric Welding Institute of the NAS of Ukraine. The research works carried out in the industrial furnaces of the type EAF DC-12 showed that the arc of the cored electrode is always maintained in the center of the electrode, which provides a stable electric mode of melting on long arcs and low voltages of the power source. It was established that the voltage in the near cathode area, as well as the range of current and voltage pulsation of the cored electrode arc is significantly lower than in the standard (monolithic) graphitized electrode. The cored electrodes in EAF DC provide saving of active energy, reduction of reactive power losses, increase in cos φ and efficiency, reduction in the burning loss of alloying elements and the furnace noise level.

KEYWORDS: cored graphitized electrodes, EAF DC, electric power, volt-ampere characteristics, current and voltage pulsations, furnace efficiency

INTRODUCTION

In [1–3] it was noted that a characteristic feature of the world metallurgy industry in the last decades has been a year by year growing of steel production. Thus, from the middle of 70s of the XX century the steel production increased by 2.8 times and in 2021 it amounted to 1.950 bln tons.

More than 30 % of steel from the mentioned volume is melted in the electric arc furnaces of alternating (EAF AC) and direct (EAF DC) current. The total volume of electric steel is also continuously growing and by 2050 may reach 43 % [4, 5].

The growth of steel production occurred in highly competitive conditions at the metal products market and this predetermined the rapid development of different technologies and the proper equipment for melting steel, its ladle treatment, pouring, processing, etc. All these developments are aimed at improvement of such important technical and economic indicators of melting as consumption of electric power, refractory materials and graphitized electrodes, improvement of efficiency of furnaces under the condition of providing the high-quality of metal and meeting the requirements to the environmental protection.

A very important stage in the development of electric steel production, providing substantial improvement of technical and economic indicators and environmental problems of this production, was the creation and a wide implementation of EAF DC into industry.

The indisputable advantages of EAF DC are the following: efficient stirring of metal and slag; high stability of arc burning and its higher temperature; comparatively low electric power consumption; low burning loss of metal and alloying elements; very low consumption of electrodes and refractory materials; high and stable quality and satisfactory cost of metal. A stable low noise level of the operating furnaces (by 15–20 %); a significant reduction (by 6–10 times) of dust and gas emissions and reduction of interference level into supplying the mains are also noted.

The main disadvantages of EAF DC are the following: presence of one or more bottom electrodes; arc deflection in the direction opposite to the power source; need in using electrodes of the limited sizes — 700, 750 and even 810 mm [5–9].

While choosing the type of furnace it is naturally to pay attention not only to the abovementioned factors, but also to the condition and characteristics of supplying mains, charge provision, peculiarities of infrastructure, type and purpose of products, etc. Nevertheless, a number of EAF DC supporters grow and some of them believe that the indisputable advantages of EAF DC were already proved [10–14]. A number of EAF DC is continuously growing and about 1000 EAF AC and 200 EAF DC are currently operated in the world [2, 5, 15, 16].

RESEARCH PROCEDURE AND RESULT DISCUSSION

The steelmakers were always seeking and trying to reveal the potential opportunities of electrodes in order to use them as a universal instrument to control the melting parameters, and ultimately, to improve the technical and economic indicators of furnace operation [17].

As-applied to EAF DC, at the PWI, such multifunctional electrodes were designed, having a solid active insert or core. These electrodes were called the cored electrodes. The core in the electrode is made by drilling of one or more vertical holes in the standard (monolithic) electrode, which are filled with different components, including those containing elements of I and II groups of the Mendeleyev's Periodic Table with a low electron work function. Due to that, in the near cathode area of the electrode, the favorable thermodynamic conditions are created for ionization of gases of the arc column.

As a result, geometric and power parameters of the arc change dramatically. In particular, its volt-ampere characteristics (VACh), shape of the working end of the electrode and other characteristics are fundamentally changed, causing the possibility of efficient optimization of technological and electrical melting modes and, as a consequence, improvement of technical and economic indicators of furnace operation. This is evidenced by the results of laboratory and industrial investigations presented in [18]. As an example, Figure 1 shows VACh of arcs of the monolithic and cored electrodes. It is seen that at the same voltages of the arcs (40 V), in the cored electrodes the current is 1.8 times higher than in the monolithic electrode (respectively 900 A and 500 A). The core can be produced in the electrode of any quality and sizes. As the object of our investigations, the EAF DC were initially selected, where the arc repolarization is absent and, consequently, the cored electrode properties are revealed most completely.

In the process of investigations and tests of the cored electrodes, over 100 industrial experimental melts were carried out, 10 compositions of cores and 8 experimental electrical modes were tested.

The works were carried out in the 12-ton EAF DC with padded acid lining using graphitized electrodes of 350 mm diameter based on remelting of FeSiMn wastes. It is important to note that when using cored electrodes, the design of the furnace remains unchanged. The unstable charge quality (large variation in chemical and fractional composition, as well as in CaO content) causes a considerable variation of values of electric power consumption if it is attributed to one ton of a suitable ferroalloy.

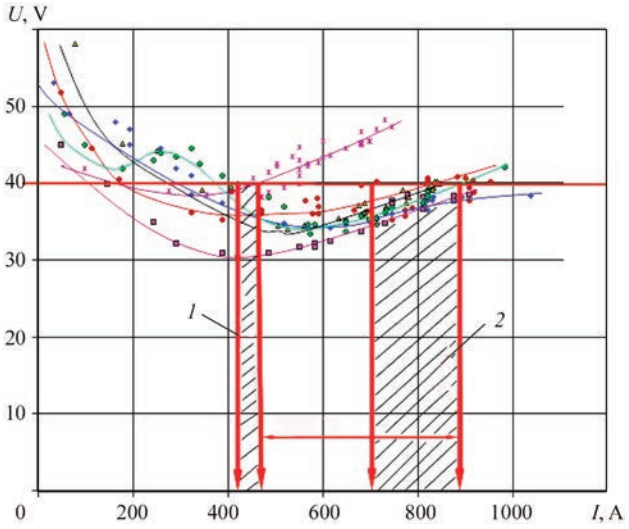

Figure 1. VACh of arcs of monolithic (*1*) and cored (*2*) electrodes of 50 mm diameter: × — monolith; ♦ — C1; ■ — C2; ▲ — C3; ○ — C4; ● — C5; L_a = 15 mm, anode — core

Therefore, the specific active electric power consumption in the specified conditions of production is accepted as the consumption for melting (on the original mass of the charge, *p*, kW·h/melt) and saving of electric power, where the compared indicators are taken as average as to the maximum number of identical melts.

The program of works envisaged: carrying out the comparative tests of the cored electrodes of different composition and monolithic electrodes at the serial modes (Figure 2); evaluation of influence of short and long arcs on power consumption, as compared to the serial mode (Figures 3, 4); evaluation of influence of reduced voltage of the power source on long arcs for the cored electrodes and nipples (Figure 5); evaluation of change in reactive power and cos φ for the cored and monolithic electrodes (Figure 6).

It follows from Figure 2 that the cored electrodes (C1, C2 and C6) at the serial modes provide a reduc-

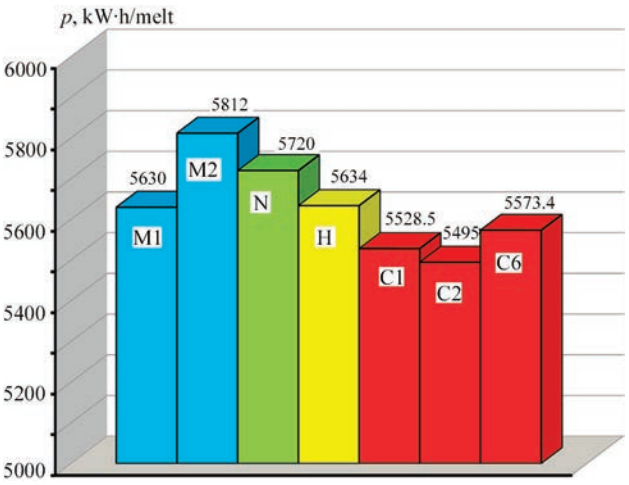

Figure 2. Specific consumption of active electric power on melts according to serial mode with the use of monolithic (M1, M2), hollow nipple (N) and cored electrodes (C1, C2, C6) (8 voltage level)

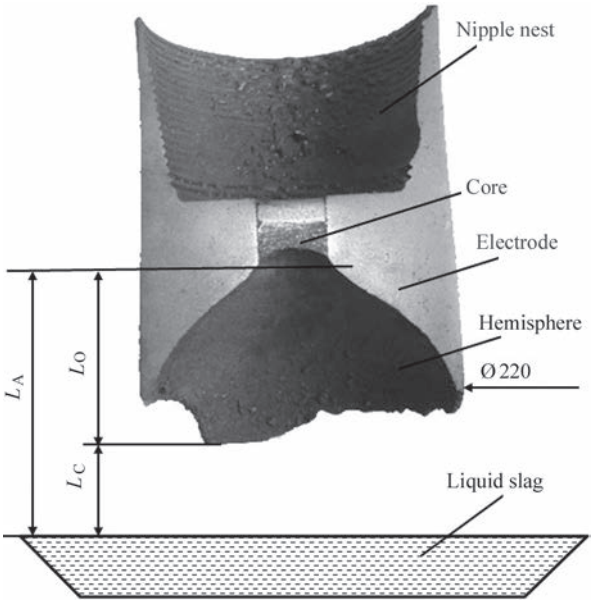

Figure 3. Macrotemplate of cored electrode with initial 350 mm dia and components of arc length of cored electrode (L_A, L_C and L_O)

tion in the active power consumption by 2.4–5.3 % as compared to the monolithic ones (M1 and M2), nipples (N) and hollow electrodes (H).

It is known that the effective means of saving the electric power is the operation of furnace on long arcs [19]. Speaking about the length of the arc as-applied to the cored electrode, it should be taken into account that the end of the cored electrode has always the shape of a concave hemisphere that essentially distinguishes it from the monolithic electrode. Therefore, the arc length of the cored electrode (L_A) consists of the length of its open (L_O) and closed (L_C) part (Figure 3). At the same time, L_A of the cored electrode is always 1.3–1.5 times longer than L_A of the monolithic electrode at the equal parameters of electric mode, which is caused by the presence of the core and its composition. In this paper, as the initial condition, the practical equality of arc length of the monolithic electrode (L_M) and the open part of the arc of the cored electrode (L_C) in a serial electric mode was taken. An increase (or decrease) in the arc length L_O at the experimental modes was carried out by the corresponding adjustment of arc voltage and current in the second half of melting (after the second charge loading). The comparative results of these investigations are shown in Figure 4. It is seen that operation on the long arcs provides a decrease in the specific consumption of electric power on the cored electrodes, on average, by 3.2 and by 8.35 % as compared to the monolithic electrodes (Figure 2). It should be noted that due to a low resistance of padded acid lining used for remelting of FeSiMn wastes, even at a comparatively low increase in the arc length (by 10–15 %) it turned to be impossible to reveal adequately the influence of the long arc factor of the cored electrodes on saving of the electric power. Here, a certain resource exists in the part of saving the electric power, which, in our opinion, will be significant in melting the steel scrap in the furnace with a basic lining. As another factor providing saving of active electric power on the cored electrodes, a stable operation of furnace at lower voltages of the furnace transformer became (Figure 5). This Figure shows that melting with the electrode C2 on the long arc and at the 9 level provided saving of electric power by 2–4 % as compared to the operation on the long arc at the 8 level (Figures 5 *a*, *b*) (serial mode on the monolithic electrodes is not stable at the 9 voltage level). The same dependence is observed on other cored electrodes and nipples (Figure 5, *c*). It is important to note that operation of the furnace on the long arcs provided also the highest efficiency determined by an average melting time of 2.11 h both at the 8 (531 V) as well as 9 (467 V) voltage level without the loss of the metal temperature before pouring. In the experimental modes, envisaging short arcs, the melting time increased in average to 2.28 h, i.e. by 7.5 %. Moreover, the cored electrodes provide also a

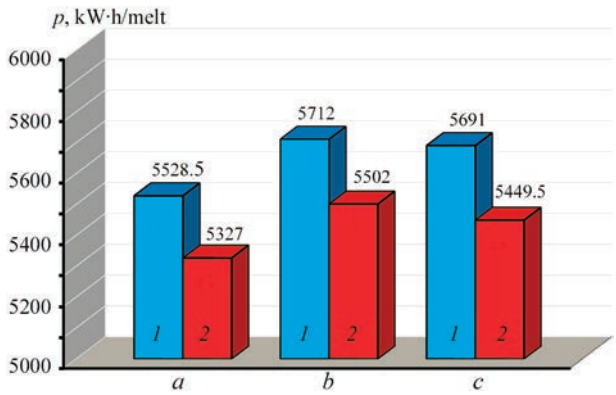

Figure 4. Specific consumption of active electric power on melts with cored electrodes on short (*1*) and long (*2*) arcs: *a* — serial (*1*) and long (*2*) arcs, core C1; *b* — core C2; *c* — core C5

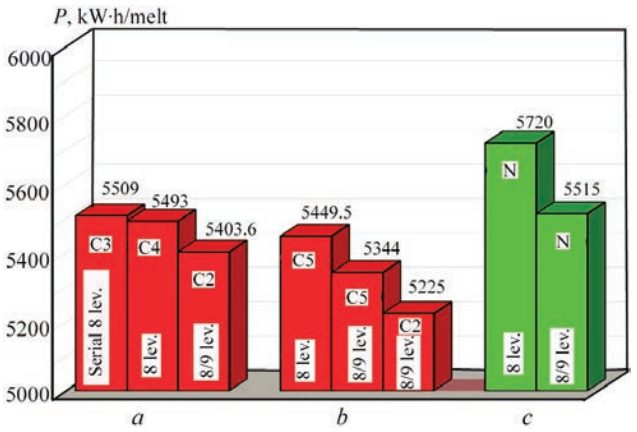

Figure 5. Specific consumption of active electric power on 8 and 9 voltage levels: *a* — cored electrodes C2 (V series), C3 and C4 (IV series) (composition F2); *b* — cored electrode C5 (IV series) (composition F3); *c* — nipples (serial mode)

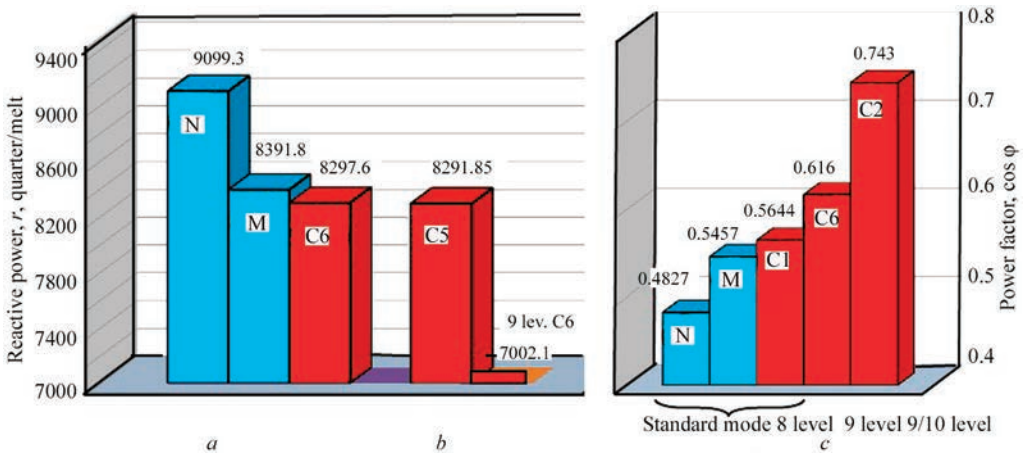

Figure 6. Comparative indicators of reducing reactive power and cos φ: *a* — standard mode, nipple No. 5 (N), monolithic electrodes (M) (melt 3485–3487 according to Batovsky) and cored electrode C6 (melt 3732–3735); *b* — standard mode, C5 and experimental mode, Nos 8 and 9 voltage levels, C6; *c* — cos φ at the standard mode of the 8 level, on experimental mode of the 9 level, on experimental mode of the 9/10 level

stable operation of the furnace and saving the electric power by 2.5 % also at the 10 (394 V) level. These data clearly indicate a high arc stability of the cored electrodes and experimental electric modes, which is provided by the effective operation of the core components. Thus, the cored graphitized electrodes when operating on the long arcs and low voltage levels of the power source can provide up to 8.35 % of saving the active electric power and an increase in the furnace efficiency by 7.5 %.

The cored electrodes provide also a significant reduction in reactive electric power, Figure 6. Already in melting at the standard mode, a reduction in reactive electric power consumption, respectively, by 8.8 and 1.1 %, occurs with the cored electrodes as compared to the nipples and monolithic electrodes (Figure 6, *a*). The consumption of reactive electric power reduced even more when using cored electrodes at a low voltage of the transformer (9 level) and with the long arc as compared to the cored electrode at the standard mode (Figure 6, *b*). And as compared to the nipples at the standard mode, this value is reduced by 23 %.

The cored electrodes cause also an increase in the power factor (cos φ), (Figure 6, *c*). From Figure 6, *c* it follows that cos φ grows from 0.4827 (8 level) in melting with the nipples at a standard mode to 0.743 in melting with the cored electrodes at the experimental mode at the 10 level.

Thus, while operating with cored electrodes of optimal compositions in low transformer voltages and long arcs, saving of the active power to 8.35 % and reduction in reactive power by 23 % and increase in cos φ from 0.483 to 0.743 are provided.

To understand the facts of saving the reactive power and reduction in reactive power losses, let us consider the volt-ampere characteristics (VACh) of arcs of the monolithic and cored electrodes, Figure 7. The mentioned VAC were obtained on the model electrodes of 50 mm diameter for monolithic and five experimental compositions of cores.

In the industrial EAF DC-12, the melting processes are performed at the maximum current of 17.1–17.3 kA with the use of monolithic and cored graphitized electrodes with the initial diameter of 350 mm. In the installation (model) with the electrodes of 50 mm diameter, the mentioned current corresponds to the current of 345–350 A. As is seen from Figure 7, with the use of the cored electrodes (depending on their composition), the same current (400 A) is achieved at much lower voltage (32 V) than in the case with the monolithic electrode (62 V). Such reduction in voltage is provided due to the presence of substances in the cored material with a low electron work function. This explains a stable operation of the cored electrode arc at low transformer voltages (9 and

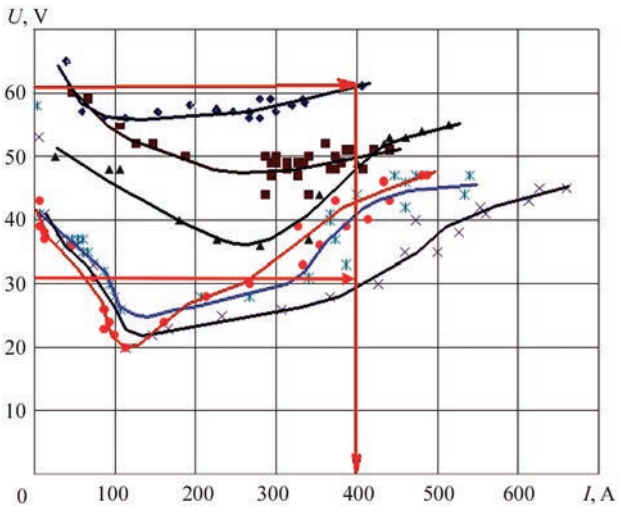

Figure 7. VACh of arcs, obtained on monolithic and cored electrodes, anode–copper: ♦ — M; ■ — C1; ▲ — C2; × — C3; ✶ C4; ● — C5

Table 1. Electric parameters of arcs at 15 mm length*

Parameters	Monolith		Core C3		Core C4		Core C5	
		% from P_a		% from P_a		% from P_a		% from P_a
Total voltage at arc U_a, V	52	–	36	–	41	–	39	–
Cathode voltage U_c, V	18	–	6	–	7.5	–	9	–
Arc column voltage U_{col}, V	20	–	20	–	20.5	–	19	–
Anode voltage U_A, V	14	–	10	–	13	–	11	–
Arc current I_a, A	300	–	420	–	320	–	313	–
Total power P_a, W	15608	–	15128	–	13120	–	12226	–
Cathode power P_c, W	5403	35	2521	17	2400	19	2821	23
Column power P_{col}, W	6003	38	8404	56	6560	51	5956	49
Anode power P_A, W	4202	27	4202	28	4160	30	3448	28

*Average data of three measurements are given.

10 level), as far as the current generated by the core elements (emitters current) takes place.

In Figure 1, this current is 400 A. One of the important consequences of the core components (emitters) operation is a considerable reduction in the voltage drop on the cathode spot of the cored electrodes (Table 1).

As it follows from the data of Table 1, there is one of the fundamental differences in the parameters of the arcs, i.e. the voltage drop at the cathode spot of the cored electrode is 2–3 times lower than on the arc of the monolithic electrode. The mentioned feature of the core arc is present both at equal arc lengths, as well as at equal arc voltages. This phenomenon causes a significant reduction in heat losses in the near cathode area of the cored electrode. In combination with a stable binding of the arc on the core and a stable electric melting mode, it causes the abovementioned saving of active electric power.

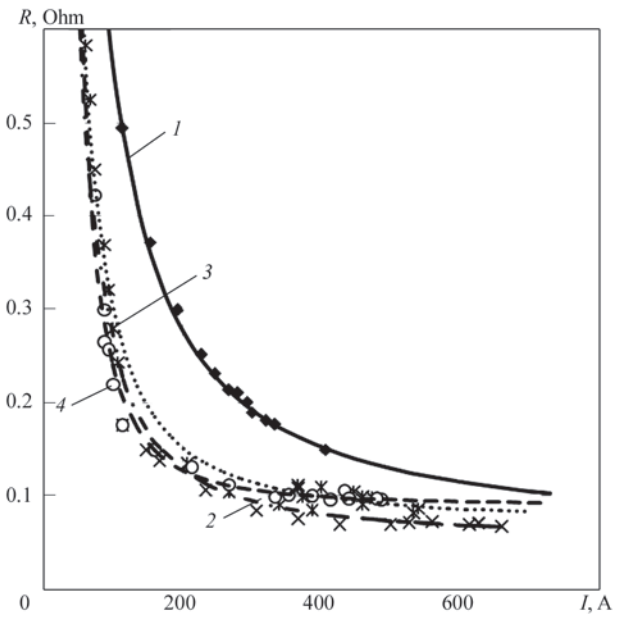

Figure 8. Dependence of arc resistance on current ($R = f(I)$) for monolithic and cored electrodes: *1* — M; *2* — C3; *3* — C4; *4* — C5

ABOUT REACTIVE POWER

At first sight, it looks weird that such high values of reactive power (commensurable with active power) are provided in the electric circuit of rectified current. At the same time, it is known that in the electric circuits, containing energy accumulators (throttle, capacitor) and a non-linear element, the self-oscillations or the so-called deterministic chaos can occur [20]. Such a circuit element in EAF DC is the electric arc possessing the properties of the non-linear active (non-reactive) energy accumulator. The studies of the voltage and current oscillograms, recorded in the industrial EAF DC-12 for the monolithic and cored electrodes at the standard modes showed that the amplitude of both current and voltage pulsations (especially voltage) is significantly larger in the case of monolithic electrode, right until repolanization of voltage. It was found that the range of voltage and current pulsation in the cored electrodes is respectively by 15 and 31 % lower than in the monolithic electrodes.

The reduction of amplitude of pulsations means the reduction of alternating component of current and, consequently, the reduction in reactive power by 23 %.

To explain the influence of activating components of the core on the level of pulsation of electric arc parameters, it is necessary to return to VACh of the arcs again. For better visualization, let us convert the dependencies $U = f(I)$ given in Figure 7 to the dependence of arc resistance on current $R = f(I)$. The experimental measurements were also processed with the help of the computer mathematics

Table 2. Results of mathematical processing of oscillograms of arcs on the model electrodes of 50 mm diameter

Electrode	Equation of dependence $R = f(I)$, Ohm	Equation of derivative dR/dI, Ohm/A	Value of dR/dI at I = 350 A, Ohm/A
Monolithic	$R(I) = 128.56 \cdot I^{-1.2} + 0.056$	$dR/dI = -154.274 \cdot I^{-2.2}$	$-3.903 \cdot 10^{-4}$
C3	$R(I) = 208.52 \cdot I^{-1.5} + 0.055$	$dR/dI = -312.777 \cdot I^{-2.5}$	$-1.365 \cdot 10^{-4}$
C4	$R(I) = 230.52 \cdot I^{-1.5} + 0.071$	$dR/dI = -345.783 \cdot I^{-2.5}$	$-1.509 \cdot 10^{-4}$
C5	$R(I) = 1512.84 \cdot I^{-2} + 0.090$	$dR/dI = -3025.671 \cdot I^{-3}$	$-0.706 \cdot 10^{-4}$

package Scilab and the mathematical dependences $R = f(I)$ were obtained for the each considered case. The results of mathematical processing of experimental measurements are presented in Figure 8. The currents of 345–350 A correspond to the range of rated current of melting in the industrial EAF DC-12 furnace (14.9–17.8 A) in the model conditions on the electrodes of 50 mm diameter. Table 2 gives some results of mathematical processing of oscillograms of arcs on model electrodes.

The indicator of the VACh nonlinearity for the preset value of current is a tilt angle to the curve of the dependence of the arc resistance on the current $R = f(I)$. The value of the tangent of this angle is equal to the first derivative dR/dI at this point. The linear dependence of VACh is characterized by a constancy of resistance, i.e. horizontal line of dependence of resistance on current.

The value of the derivative dR/dI for the current of 345–350 A can be considered as indicator of the VAC nonlinearity. The higher dR/dI from zero, the greater is the difference of VACh from the linear dependence and, as is seen from the given data, in the cores this value is closer to zero than in the monolithic electrode. In other words, the closer VACh of the arc to the linear dependence in the operating current range, the lower is the pulsation of current and voltage, which cause a decrease in reactive power losses during operation with the cored electrodes. Here the phenomenon of autooscillations in the electric circuit of EAF DC is least expressed.

The calculated, experimental and practical data mentioned above provide a strong evidence of clear power advantages of a "cored" arc. The presented data were obtained while remelting wastes of 30 % FeSiMn, i.e. a relatively simple and homogeneous charge. It gave a convincing reason to use cored electrodes for remelting more complex, multifractional and heavy charge. Such a charge was the catalyst — a product of oil refining. Its base is Al_2O_3. The catalyst also contains a large amount of nickel, molybdenum and vanadium. It is featured by a high content of sulphur, which amounts up to 4–6 %, and a high residual content of oil products. The basic purpose of remelting this material consisted in obtaining the maximum amount of molybdenum and nickel (ingots), as well as producing the slag with a high content of V_2O_5 (more than 12 %) for production of 50 % of FeV. Before melting, a preliminary preparation of the catalyst was not carried out, which caused extremely unstable electric and technological conditions and, as a consequence, technical and economic indicators of melting. Against the background of these circumstances, checking the efficiency of the cored electrodes work was of great interest. The work included three stages:

- Stage 1. Remelting of the catalyst itself with obtaining a vanadium-containing slag and a metal phase (ingots), containing Ni and Mo;
- Stage 2. Refining of ingots and obtaining a product with the maximum possible content of Ni and Mo;
- Stage 3. Producing ferrovanadium.

Technical and economic indicators (output rate, kg/h, output of a metal phase (reduction in burning loss), %, electric power consumption, kW·h/t) of the catalyst remelting by stages using the monolithic (M) and cored electrodes (C) are presented in Figure 9. The arrows show the comparable indicators.

First of all, the mentioned data indicate, that cored electrodes at all stages of remelting the catalyst and its products have essential advantages as compared to monolithic electrodes. These advantages have a large range of values (Figure 9, *a–c*), which is explained by two factors. The first is the lack of the charge (catalyst) preparation as required and, as a result, instability of electrical and technological conditions of melting. The second point, which has a major importance, is that compared indicators are largely determined by the composition of cores.

The data given in Figure 9, *a–c* show the following: the efficiency of the furnace during remelting of a catalyst is increased by 21.3–23.6 %. An increase in the output of the metallic phase (decrease in the burning loss of Ni, Mo, Fe) amounts to 1–9 %; a decrease in the specific power consumption is provided in the range of 16.6–30.0 %. Higher indicators were provided in the melts using cores of the composition C11.

During remelting of the metallic phase (of ingots), the following indicators are provided (Figure 9, *d–f*):

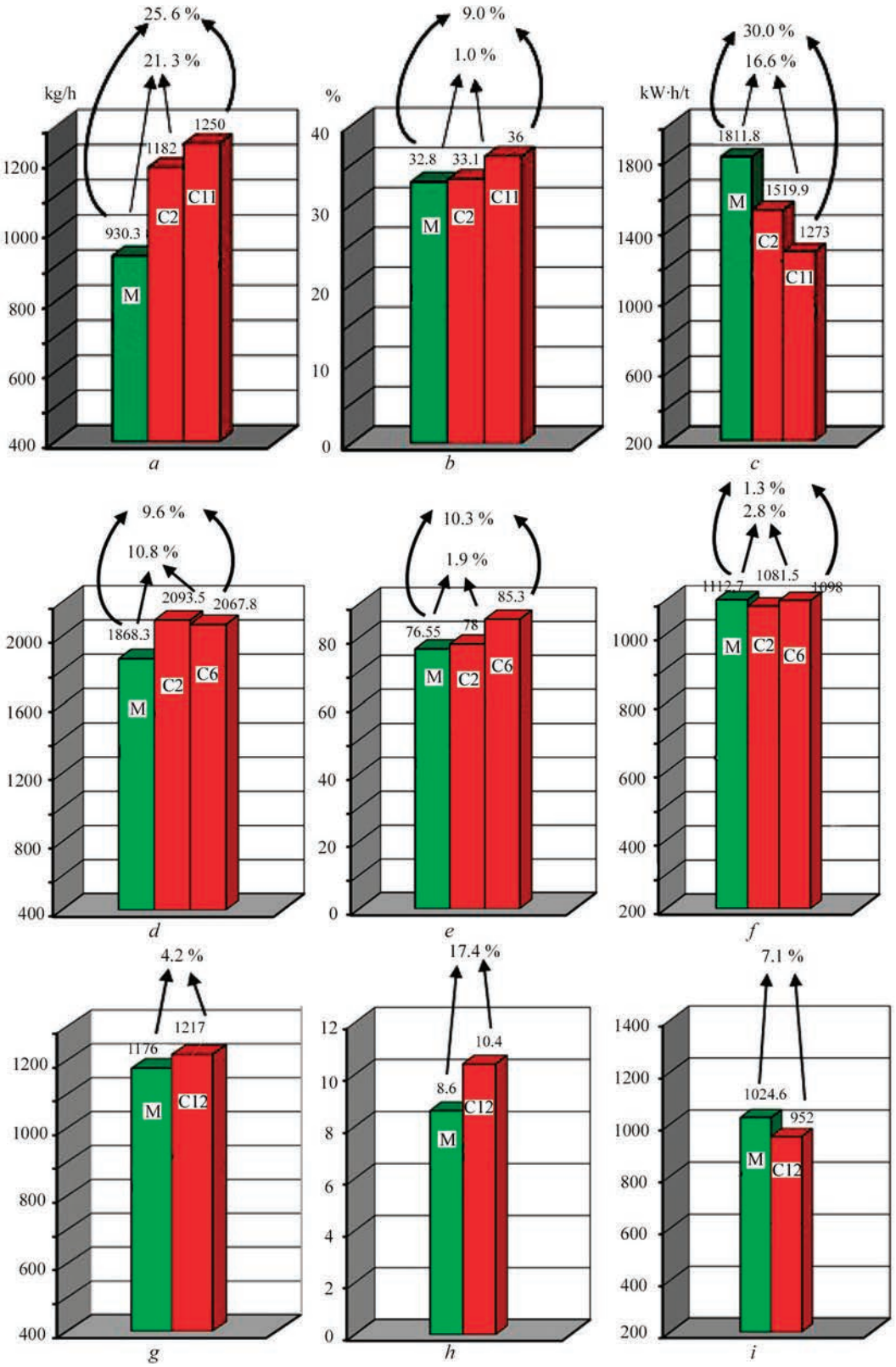

Figure 9. Efficiency of furnace (*a*, *d*, *h*), output of metallic phase (reduction of burning loss of Fe, Ni, Mo), (*b*, *e*, *h*) and consumption of electric power (*c*, *f*, *k*) during remelting of: catalyst with the use of monolithic (M) and cored (C2 and C11) electrodes (stage 1); of metallic phase (ingots) with the use of monolithic (M) and cored (C2 and C6) electrodes (stage 2); and melting of ferrovanadium while using monolithic (M) and cored (C12) electrodes (stage 3)

the efficiency of the furnace is increased by 96–108 %; the output of the metallic phase is increased by 1.9–10.3 % and the power saving is 1.3–2.8 % on the cored electrodes.

During melting of ferrovanadium with the use of cores C12 (Figure 9, *g*–*h*), the efficiency of the furnace is also increased by 4.2 %; a decrease in the burning loss of vanadium by 17 % is provided;

during melting of 50 % ferrovanadium, the power saving amounted to 7.1 %.

In the process of experimental melts in the EAF DC-12 furnace, it was found that an essential advantage of cored electrodes is the fact that during their use, the interval in melting time is 2.0–2.5 times reduced, i.e. a high stability of electrical and thermal conditions of the furnace operation, and a more full proceeding of physical and chemical processes are provided.

An important distinctive feature of cored electrodes consists in the fact that during melting, the working end of such an electrode always has a shape of a concave hemisphere, regardless of the core composition and the parameters of the electrical conditions. This hemisphere predetermines two main technological factors. First, it can concentrate of up to 50 % of the arc power. This, in combination with a high stability of long arcs on the cored electrodes should provide the effective melting of a large-sized charge and a smaller amount of arc breaks during melting of "wells", etc. Therefore, it is expected that the consumption of refractory materials will be shortened by 20–30 %, a number of repairs of the furnace will decrease, and, therefore, its efficiency will increase.

It is also confirmed, that the cored arc also determines a 10–12 % reduction in the noise level during the operation of EAF DC-12.

The data presented in the article have fully substantiated the works on using cored electrodes in electric arc furnaces of alternating current.

CONCLUSIONS

1. It is noted that more than 30 % of steel from the world steel production is melted in arc furnaces of direct (EAF DC) and alternating current (EAF AC).

2. The effective means for improvement of the technical and economical indicators of EAF DC is the use of the cored graphitized electrodes, designed at the PWI. Cored electrodes are composed of components with a low electron work function, which creates favorable thermodynamic conditions for ionization of the arc column gases in the near cathode area.

3. It was found that the arc of the cored electrode is always maintained stable at the core and does not migrate along the end of the electrode, characterized by a high stability at a large length and at low voltages of the power source.

4. It was found that at equal voltages the arc current of a cored electrode is by 1.8 times higher than the current of a monolithic electrode.

5. It was found that the voltage drop in the near cathode area in the cored electrode is 2–3 times lower than in the monolithic electrode, which significantly reduces power (heat) losses in this part of the electrode.

6. It was shown that the amplitude of oscillations of voltage and current of the cored electrode arc is on average by 15 and 31 % lower, respectively, as compared to the arc of the monolithic electrode.

7. In accordance with the features and parameters of the arc of the cored electrodes, during remelting of FeSiMn wastes in the industrial EAF DC, the following parameters are provided: stable electric mode; up to 8.35 % saving of active electric power during operation on long arcs; reduction in reactive power to 23 %; increase in cos φ from 0.48 to 0.74; increase in the furnace efficiency by 7.5 %; reduction in interval between melting time by 2.0–2.5 times;

8. During remelting of the catalyst and its derivatives (ingots, vanadium-containing slag, melting of ferrovanadium), the cored electrodes depending on their composition, provide the following indicators: increase in the furnace efficiency by up to 25.6 %; reduction in burning loss of Ni and Mo during remelting and ingot refining by 10.3%; reduction in burning loss of vanadium by 17.4 % during melting of ferrovanadium; reduction in specific electric power consumption by 30 %.

9. The obtained results have fully substantiated the works on using cored electrodes in electric arc furnaces of alternating current.

REFERENCES

1. Dyudkin, D.A., Kisilenko, V.V. (2008) *Steelmaking.* Vol. 1. Moscow, Teplotekhnik [in Russian].
2. (2013) *"Steeltime"*. Data portal on ferrous and non-ferrous metallurgy.
3. Belkovsky, A.G., Kats, Ya.L., Krisnyansky, M.V. (2012) State-of-the-art and tendencies of development of steel production technology in DSP and their structures. *Staleplavilnoe Proizvodstvo,* **8**, 15–18 [in Russian].
4. Grishchenko, S.G., Granovsky, V.K. (2015) Metallurgy of the world and Ukraine in 2015: Problems and Prospects. *Int. Sci.-Tech. Conf. of National Metallurgical Academy of Ukraine (Ukraine, Dnipro, 9–11 December, 2015)*, 23–26 [in Russian].
5. *Shatokha V.* (2015) Review of core support capabilities of the equipment SoS analysis and evaluation. In: *Proc. of 2nd Inter. Conf. on Advanced in Metallurgical Processes and Material (Kyiv, Ukraine, June 3–5 2015)*.
6. Milyaev, A.F., Kadnikov, S.V. (2002) Choice of type and capacity of cast iron and steel in foundry. *Elektrometallurgiya*, **11**, 21–24 [in Russian].
7. Dyudkin, D.A., Bat, S.Yu., Grinberg, S.E., Marintsev, S.N. (2003) *Steel production at ladle-furnace unit.* Donetsk, OOO Yugovostok [in Russian].
8. Ramires, M., Alexis, I., Trapage, G. et al. (2002) Stirring of melt in direct current arc furnace. *Novosti Chyornoi Metallurgii za Rubezhom,* **3**, 54–57 [in Russian].
9. Savitsky, A. (2000) On choice of rational design of direct current DSP. *Elektrometallurgiya*, **8**, 13–19 [in Russian].
10. (2015) *Classification of modern arc electric furnaces. Direct and alternating current arc furnaces.* Ukrainian Association of steelmakers. Inform. Portal [in Russian].
11. Elansky, D.G. (2001) Tendencies of development of electric steelmaking. *Elektrometallurgiya*, **5**, 3–18 [in Russian].

12. Platonov, B.P., Kotelnikov, O.I. (1996) Examination of dust-gas emissions of direct and alternating current arc furnaces. *Litejnoe Proizvodstvo,* **1**, 24–27 [in Russian].
13. Volodin, A.M., Bogdanovsky, A.S., Malinovsky, V.S. (2004) Results of operation of DC furnace DS PTU-20 at OJSC "Tyazhpressmash". *Litejnoe Proizvodstvo*, **4**, 31–35 [in Russian].
14. Makarov, A.N., Shimko, M.B., Ostrik, V.V. (2004) Analysis of the main technical and economic indices of DC and AC arc furnace operation. *Elektrometallurgiya,* **3**, 5–9 [in Russian].
15. *Boom Rob* (2015) Breakthrough development in ironmaking and steelmaking: Collaboration or competition. In: *Proc. of 2nd Inter. Conf. on Advanced in Metallurgical Processes and Materials (Kyiv, Ukraine, June 3–5 2015)*.
16. Tishchenko, P.I.,Timoshenko, S.N., Onishchenko, S.P. (2015) *Hearth electrodes DSP PT. Review of the main technical solutions.* DonNTU, PE ROUD Society. Ukrainian Association of steelmakers. Inform. Portal on Ferrous and Nonferrous Metallurgy. Donetsk, Ukraine [in Russian].
17. Paton, B.E., Lakomsky, V.I., Galinich, V.I. et al. (2011) Cored electrodes of electric arc furnaces. *Chiornye Metally,* **5**, 13–15 [in Russian].
18. Bogachenko, A.G., Mishchenko, D.D., Braginets, V.I. et al. (2016) Saving of electric power at the arc steel melting furnaces of direct current with graphitized cored electrodes. *Sovrem. Elektrometall.,* **1**, 58–64 [in Russian].
19. Kazachkov, E.A., Chepurnoj, A.D. (2005) Ways to increase the productivity of arc steel furnaces. *Visnyk Pryazov. DTU,* **15**, 1–5 [in Russian].
20. Sidorets, V.N., Pentegov, I.V. (2013) *Deterministic chaos in nonlinear circuits with an electric arc.* Kyiv, IAW [in Russian].

CONFLICT OF INTEREST

The Authors declare no conflict of interest

CORRESPONDING AUTHOR

A.G. Bogachenko
E.O. Paton Electric Welding Institute of the NASU
11 Kazymyr Malevych Str., 03150, Kyiv, Ukraine.
E-mail: stemet@ukr.net

SUGGESTED CITATION

A.G. Bogachenko, D.D. Mishchenko, I.A. Honcharov,V.I. Braginets, I.A. Neylo, Y.A. Plevako (2023) Application of cored graphitized electrodes in electric arc furnaces of direct current (EAF DC). *The Paton Welding J.*, **3**, 42–50.

JOURNAL HOME PAGE

https://patonpublishinghouse.com/eng/journals/tpwj

Received: 20.02.2023
Accepted: 24.04.2023

DOI: https://doi.org/10.37434/tpwj2023.03.07

NUMERICAL ASSESSMENT OF BRITTLE STRENGTH OF FIELD WELDS OF THE MAIN GAS PIPELINES AT TRANSPORTATION OF GAS-HYDROGEN BLENDS

O.S. Milenin, O.A. Velykoivanenko, G.P. Rozynka, N.I. Pivtorak

E.O. Paton Electric Welding Institute of the NASU
11 Kazymyr Malevych Str., 03150, Kyiv, Ukraine

ABSTRACT

Features of the influence of hydrogen degradation of pipe steel on brittle strength of circumferential field welded joints were considered within the framework of analysis of the possibility of using the Ukrainian gas-transportation system for transportation of mixtures of natural gas and hydrogen. Applied for these purposes were the methods of finite-element modeling of the structure stress-strain state during welding and further service together with modern criteria of macroscopic fracture of a cracked body. Results of prediction of brittle strength margin of a typical welded section of the main gas pipeline with postulated surface cracks at transportation of gas-hydrogen mixtures of different composition showed that the areas of the weld and heat-affected zone are the most prone to brittle fracture. However, as regards fatigue strength of welded joints, greater ranges of stress intensity factors in the heat-affected zone under the impact of cyclic loading by inner pressure or bending moment, result in an essential reduction of the residual strength margins at prediction of long-term brittle strength.

KEYWORDS: gas-hydrogen mixture, main gas pipeline, hydrogen degradation, technical condition, brittle strength, cyclic loading

INTRODUCTION

Practical perspective of application of Ukrainian gas-transporting system for transportation of blends of fossil natural gas and green hydrogen requires corresponding substantiation of safety of gas pipeline operation. In addition to control of possible leakages and accumulation of gaseous hydrogen during analysis of technical condition of gas pipelines it is necessary to take into account different aspects of hydrogen degradation of pipe steel. At that one of the most susceptible places are field circumferential welded joints with corresponding residual stress and deformation fields caused by assembly welding under field conditions. This promotes larger tendency to appearance of different types of defects of metal inhomogeneity (lacks of penetration, pitting corrosion, stress-corrosion cracking etc.) and increase of risks of initiation of unallowable damage of structure as a result of effect of static or cyclic operation loading.

Analysis of professional references [1–4] showed that the problem of hydrogen degradation of pipe steels is sufficiently well outlined, however, majority of the works are dedicated to solution of materials science problems of determination of peculiarities of interaction of diffusion hydrogen with metal in certain state, including after welding. The final aim of such investigations is determination of dependencies of degradation of mechanical properties of typical materials as a result of long-term operation in hydrogen medium. Nevertheless, the relevant is a set of problems on analysis of effect of material hydrogen degradation on decrease of bearing capacity and general deterioration of technical state of specific gas pipeline under design operation conditions. In particular, it is known that one of the negative effects of increased concentration of diffusion hydrogen in typical pipe steels of different strength class is decrease of their brittle fracture and fatigue fracture resistance [5]. Similar negative effect has assembly or repair welding. It causes formation of residual tensile stresses in weld metal area and heat-affected zone (HAZ) that promotes initiation and propagation of cracks. However, solution of a complex problem of analysis of reliability of welded joints of pipeline systems in transportation of gas-hydrogen blends (GHB) has insufficient representation.

This work considers an issue of numerical analysis of brittle strength of assembly welds of main gas pipelines (MG) in transportation of GHB with the purpose of determination of peculiarities of effect of hydrogen degradation of pipe metal on their reliability and operability.

INVESTIGATION PROCEDURE

Combination of a technological factor of welding effect and degradation of MG material resistance as a result of excessive hydrogenation complicates analysis of bearing capacity of pipeline in area of circumferential field weld. Therefore, it is reasonable to use the methods of mathematical modeling and computer simulation of the welding processes with corresponding numerical analysis of susceptibility of welded structure to failure that allows consideration of various aspects of external operation effect on properties and

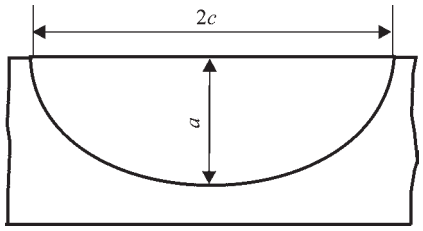

Figure 1. Scheme of surface semi-elliptical crack

boundary condition of structure. A basis of evaluation of brittle strength of welded joints was a principle of "virtual" defects, i.e. the general rules of fracture mechanics of bodies with cracks was used for calculation of a boundary condition of welded joint with postulated crack. An idea of this calculation lies in the fact that in a process of flaw detection of welded joints the small crack-like defects (the most dangerous of which are surface ones, Figure 1) can be missed or they can be formed on the first stages of structure operation. Application of such approach allows considering an effect of welding process on stress-strain state (SSS) in the area of permanent joint as well as interaction of postwelding and service stresses on welded structure reliability.

Prediction of a current and residual SSS in a section of MG welded area was performed using a finite-element analysis of kinetic of nonstationary temperature field in area of effect of welding heat source and corresponding distribution of stresses and strains of pipe metal. Thus, a distribution of temperatures was determined by solution of a heat conduction equation with temperature-dependent thermophysical characteristics of material [6]. Calculation of structure SSS kinetics was realized by means of a consecutive tracing of elasto-plastic deformations from the beginning of welding up to complete cooling of structure and further operation loading in scope of a boundary problem of nonstationary thermoplasticity [7]. Thus, the components of tensor of strains ε_{ij} and stresses σ_{ij} correlate between each other respectively to the generalized Hooke's law and associated law of plastic flow [8]:

$$\Delta\varepsilon_{ij} = \Psi\left(\sigma_{ij} - \delta_{ij}\sigma\right) + \delta_{ij}\left(K\sigma + \Delta\varepsilon_T\right) - \\ -\frac{1}{2G}\left(\sigma_{ij} - \delta_{ij}\sigma\right)^* - \left(K\sigma\right)^*, \quad (1)$$

where $i, j = r, \beta, z$ in a cylinder coordinate system; δ_{ij} is the Kronecker symbol; $K = (1–2\nu)/E$ is the modulus of three-dimensional compression; E is the Young's modulus; ν is the Poisson's ratio; $G = 0.5E/(1+\nu)$ is the shear modulus; ε_T is the temperature deformation, symbol "*" attributes corresponding change to previous step of tracing; Ψ is the function of material condition, which determines plastic flow condition:

$$\Psi = \frac{1}{2G}, \text{ if } \sigma_i < \sigma_y, \Psi > \frac{1}{2G}, \text{ if } \sigma_i = \sigma_y, \\ \sigma_i > \sigma_y \text{ state is unallowable.} \quad (2)$$

where σ_i is the stress intensity; σ_y is the yield limit.

Determination of Ψ function was performed by iteration in each step of a numerical tracing by time or increase of external power load in scope of solution of a boundary problem of nonstationary thermoplasticity [8].

Realization of a method of "virtual " defects for evaluation of brittle strength of MG welded joints with different level of hydrogen degradation of metal lies in a postulation of crack of certain size and orientation in each of assemblies of finite-element partition of pipe surface, in scope of which a total SSS caused by welding and service loads was determined. For each case of a virtual defect it was calculated a residual safety factor of brittle strength n based on corresponding criterion of a boundary condition of body with crack. One of the most widespread criteria is a procedure R6 [9] which is based on a two-parameter diagram of brittle-tough failure of a body with crack (Figure 2) and has the following mathematical description:

$$nK_r\left(L_r\right) = \begin{cases} \left[1 - 0.14\left(nL_r\right)^2\right] \times \\ \times\left\{0.3 + 0.7\exp\left[-0.65\left(nL_r\right)^6\right]\right\}, \\ \text{if } nL_r \le L_{r\max} \\ 0, \text{ if } nL_r > L_{r\max}. \end{cases} \quad (3)$$

where $K_r = K_I/K_{Ic}$, $L_r = \sigma_{ref}/\sigma_y$; K_i are the coefficients of stress intensity; K_{Ic} is the fracture toughness; σ_{ref} are the reference stresses

Calculation of K_I, σ_{ref} present in (3) was carried out according to the algorithms provided in particular in [10].

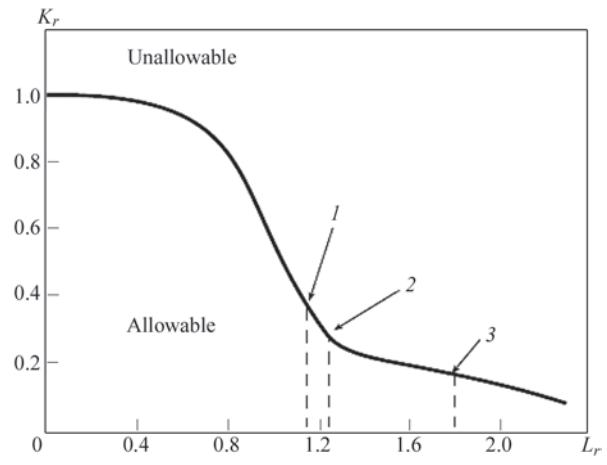

Figure 2. Two-parameter diagram of evaluation of susceptibility to brittle-tough fracture of structures with crack-like defect [9]: *1* — 1.15 (typical low-alloy steels and welded joints); *2* — 1.25 (typical low-carbon steels and austenite welded joints); *3* — 1.8 (typical austenite steels)

Analysis of distribution of strength safety factors in a structure section allows evaluating brittle strength of welded joint depending on parameters of welding process, conditions of external force effect and hydrogen degradation of material. One of the key aspects of specific realization of given algorithm is a selection of size of a postulated defect. On the one hand, linear dimension of a crack should not exceed resolution of the flaw detection tools, and on the other hand, be sufficiently large for detection of welded structure susceptibility to brittle fracture. As a conservative approach it is possible to use the standard requirements as for a size of postulated defect or correlate a residual safety factor of pipeline with crack with the design requirements [11].

Evaluation of operability of a MG welded element in addition to hydrogen degradation of material properties requires consideration of possibility of fatigue failure as a result of effect of cyclic load. This type of failure can be considered from point of view of the classical approaches to analysis of long-term strength of welded structures using *S*–*N*-diagrams [12] as well as based on evaluation of allowability of the postulated cracks by the algorithms mentioned above. At that additionally it is necessary to take into account a fatigue growth of sizes of defects for certain operation period. A rate of growth of fatigue crack (increase of its linear sizes) depending on number of cycles of load N with asymmetry of cycle R is calculated according to the Paris's law [13]:

$$\frac{da}{dN} = \frac{C\Delta K^m}{(1-R)-\frac{\Delta K}{K_{Ic}}}, \qquad (4)$$

where C, m is the Paris coefficients; ΔK is the range of load intensity coefficient.

PRACTICAL EXAMPLE

The peculiarities of effect of hydrogen in a content of a blend transported by pipeline on strength of field welded joints was investigated by a typical example of straight MG section of D = 1420 mm diameter and wall thickness t = 20 mm, pipe material — pipe steel 17G1S. Inner pressure of a transported GHB (maximum value P = 7.5 MPa) was considered as an external load and additionally a bending moment in pipe axis plane M as for the case of static loading as well as at cyclic one to 10000 cycles. A maximum value of bending moment was taken equal $8.4 \cdot 10^9$ N·mm that correspond to the values of additional axial stresses comparable with those provoked by the maximum inner pressure. In general case the bending moment of similar type can be caused by different factors depending on type and conditions of operation of a specific pipe section. Thus, for the sections of aerial crossings through artificial or natural obstacles an additional bend is typically formed at wind loads or in passing pipe inspection gears (in particular, at resonance increase of oscillation amplitude). For underwater MG sections similar additional force effect can appear in failure of integrity of distributed ballasting and cyclic effect of undercurrents.

Table 1. Effect of hydrogen in atmosphere on properties of smooth specimens from pipe steel at tensile tests and rate of fatigue crack development [14]

Hydrogen concentration, vol.%	Ultimate strength, MPa	Yield limit, MPa	$C \cdot 10^8$	m
0	656.39	523.90	2.25	2.592
5	666.00	518.56	25.7	2.582
10	657.81	525.52	29.8	2.580
20	656.06	524.83	35.1	2.574
50	661.54	523.67	99.3	2.389

In general case the mechanical properties of metal of pipeline element being considered depend on hydrogen concentration ν_H in transported GHB and corresponding level of hydrogen degradation. According to available data [14] the most negative effect of hydrogen on pipe steels is observed on characteristics of fatigue fracture resistance that is quantitatively described by the changes of the Paris coefficients C and m (see Table 1). At that at indicated concentrations of hydrogen in GHB up to 50 % no significant decrease of fracture toughness K_{1c} is observed [15]. Similarly, it was assumed that for low-alloy pipe steels a prevailing factor affecting resistance to fatigue crack development in area of weld metal and HAZ is the significant residual stresses (reaching metal yield limit) and high ΔK, whereas inhomogeneity of the Paris coefficients in a welded structure section is insignificant.

As it was mentioned above, an important parameter in calculation of brittle strength of MG welded element is a value of postulated surface crack $2c \times a$ (see Figure 1). For a case being considered using preliminary calculation it was determined that at $2c \times a$ = = 3.0×0.5 mm a brittle strength margin of pipe on a welded joint periphery made around 1.81 and, thus, conservatively corresponds to the pipeline design requirements (1.79). The cracks of different orientation relatively to pipe axis (longitudinal, circumferential) were studied for a particular consideration of 3D SSS in calculation of brittle strength and minimum safety factor n was selected.

RESULTS AND DISCUSSION

A finite-element analysis of residual SSS in area of welding of circumferential welds allowed taking into account an effect of assembly technological aspect on

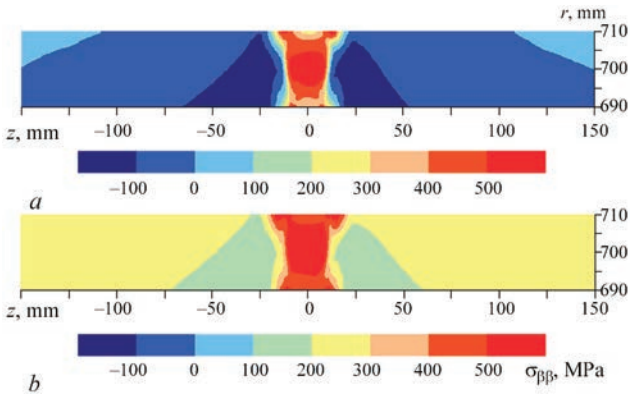

Figure 3. Calculation field of circumferential stresses $\sigma_{\beta\beta}$ in longitudinal pipe section: *a* — residual postwelding state; *b* — under condition of loading by inner pressure 7.5 MPa

reliability and operability of pipeline. Interaction of operation stresses with postwelding ones has a significantly nonlinear nature in both typical directions relatively to pipeline axis, namely circumferential and axial (Figures 3, 4). Inhomogeneity of a stress field at different stages of cyclic load of MG welded section provokes a corresponding spatial distribution of ranges of a stress intensity coefficient ΔK (Figure 5) and, as a result, a change of susceptibility of various sections of structure to brittle fracture in a process of long-term operation. The most susceptible to brittle fracture at static loading is a weld areas and HAZ. They are characterized with high total tensile stresses, caused by interaction of operation and postwelding SSS (Figure 6).

Regarding the fatigue strength of welded joints under effect of cyclic varying inner pressure or bending moment, the larger ranges of values of stress intensity coefficient in HAZ provoke significant decrease of the residual safety factors *n* in prediction of long-term brittle strength. As can be seen from investigation results (Figure 6) hydrogen degradation has the maximum effect on the brittle strength residual safety factor of HAZ metal under conditions of cyclic load by inner pressure:

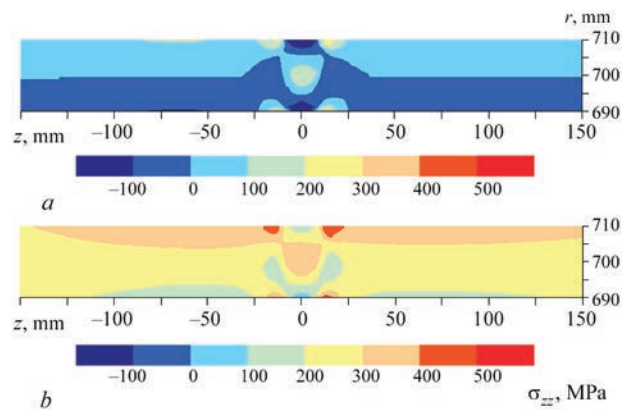

Figure 4. Calculation field of axial stresses σ_{zz} in longitudinal pipe section: *a* — residual postwelding state; *b* — under condition of loading by inner pressure 7.5 MPa and bending moment $8.4 \cdot 10^9$ N·mm

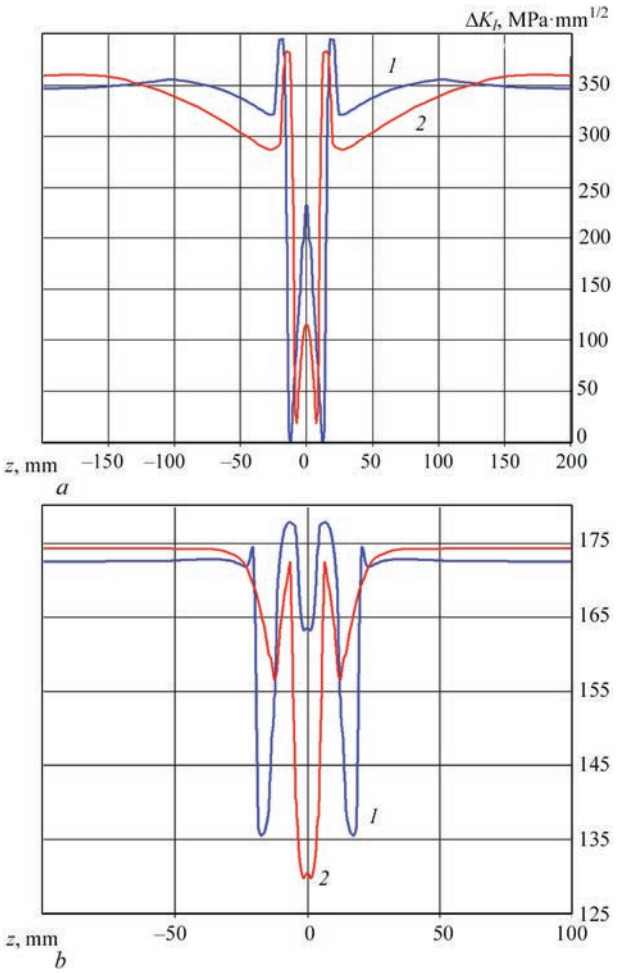

Figure 5. Distribution of values of range of stress intensity coefficient ΔK along inner (*1*) and outer (*2*) surfaces of pipe after 10000 cycles of loading by inner pressure (*a*) and bending moment (*b*)

a total decrease of *n* values exceeds 25 % in comparison with a case of transportation of pure natural gas. At that an effect of cyclic bending moment has not so dramatic influence on pipeline reliability.

The dependencies of a minimum brittle strength safety factor of MG welded element on volume of hydrogen concentration ν_H in a transported GHB in base metal and in HAZ under conditions of cyclic loading by inner pressure and bending moment are quasi-linear, have different angles of inclination (Figure 7) that corresponds to different metal susceptibility to brittle fracture in developed hydrogen degradation and cyclic loading. This effect can also be numerically characterized by a value of fatigue growth of crack size. Thus, in the case of cyclic change of inner pressure depending on hydrogen concentration in a blend the maximum increase of linear dimensions of defect for 10000 cycles of loading is in the range from 0.13 mm (at $\nu_H = 0$ %) to 4.7 mm ($\nu_H = 50$ %), in case of cyclic loading by bending moment from 0.013 to 0.31, respectively.

It is necessary to note that in scope of this investigation the consideration is given particularly to brittle strength of metal of MG welded section, but in area

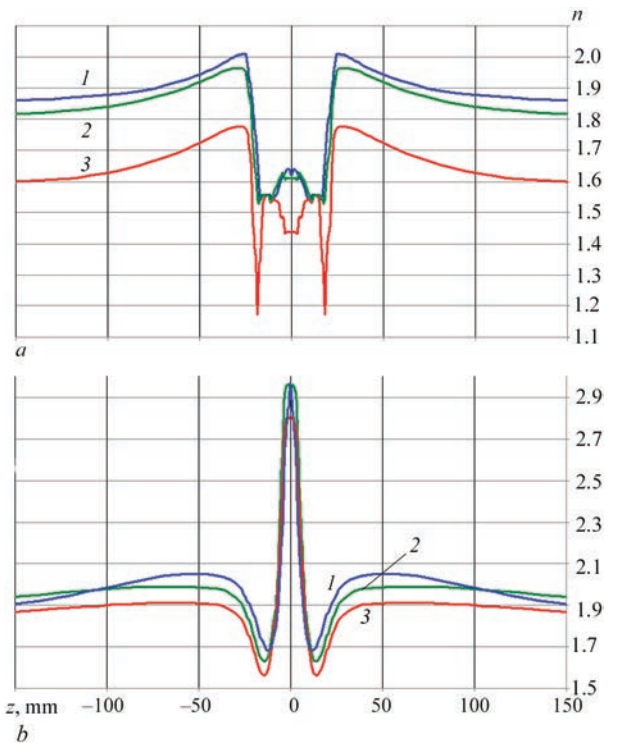

Figure 6. Distribution of values of brittle strength safety factor n along outer pipe surface under conditions of static and cyclic loading by inner pressure (*a*) and bending moment (*b*): *1* — static loading (ν_H = 0.5); *2* — cyclic loading (ν_H = 0.0, 10000 cycles); *3* — cyclic loading (ν_H = 0.5, 10000 cycles)

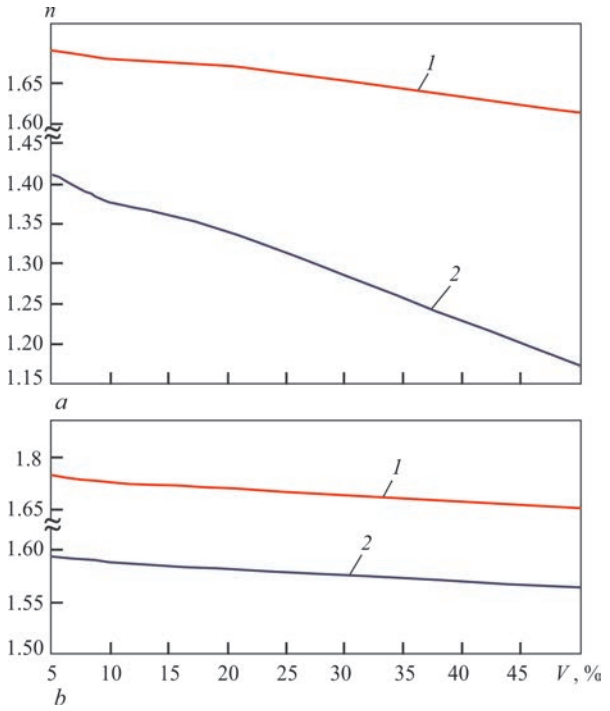

Figure 7. Dependencies of minimum brittle strength safety factor of MG welded element on volume concentration of hydrogen ν_H in transported blend in base metal (*1*) and in HAZ (*2*) under conditions of cyclic loading (10000 cycles) by inner pressure 0–7.5 MPa (*a*) and bending moment $8.4 \cdot 10^9$ N·mm

of welded joint, where stress value reaches material yield limit, the boundary condition and macroscopic failure can distinguish by tough or brittle-tough fracture. However, these types of fracture are not typical in a case of hydrogen embrittlement of metal in long-term operation of pipeline under conditions of continuous contact with hydrogenized medium.

CONCLUSIONS

1. It was developed a numerical procedure for analysis of brittle strength of the MG welded sections in transportation by them of the blends of natural gas and hydrogen. A basis of proposed procedure is a finite-element analysis of structure SSS in welding and further operation loading as well as calculation of a residual safety factor under assumption of presence of a postulated surface crack of certain size. At that the possibility was considered for prediction of brittle strength by static as well as cyclic loading. For this a rate of fatigue growth of defect size by the Paris's law was calculated.

2. A typical example of straight MG section ($D \times t$ = = 1420×20 mm, 17G1S) was used for investigation of a peculiarity of effect of hydrogen degradation of metal on pipeline reliability. Inner pressure (up to P = 7.5 MPa) and bending moment in an axis plane (up to $8.4 \cdot 10^9$ N·mm) was considered as an external loading. It is shown that the most susceptible to brittle fracture is a weld section and HAZ, which are characterized with the high total tensile stresses caused by interaction of operation and postwelding SSS. However, regarding fatigue strength of the welded joints under effect of cyclic loading by inner pressure or bending moment, the bigger ranges of values of stress intensity coefficient in HAZ provoke more substantial decrease of residual safety factors in prediction of long-term brittle fracture.

3. It is shown that the hydrogen degradation has the maximum effect on brittle strength of a welded pipeline under conditions of cyclic load by inner pressure: 10000 cycles of loading promote total decrease of a residual safety factor in HAZ for more than 25 % in comparison with a case of transportation of pure natural gas. At that the cyclic bending moment does not have significant effect of pipeline reliability.

REFERENCES

1. Nechaev, Yu.S. (2008) Physical complex problems of aging, embrittlement and fracture of metallic materials in hydrogen power engineering and main pipelines. *Uspekhi Fizicheskikh Nauk*, 178(**7**), 709–726 [in Russian].
2. Esaklul, K.A. (2017) *Hydrogen damage. Trends in oil and gas corrosion research and technologies production and transmission*. UK: Woodhead Publishing, 315–340. DOI: https://doi.org/10.1016/B978-0-08-101105-8.00013-9
3. Dmytrakh, I., Syrotyuk, A., Leshchak, R. (2022) Specific mechanism of hydrogen influence on deformability and fracture of low-alloyed pipeline steel. *Procedia Structural Integrity*, **36**, 298–305. DOI: https://doi.org/10.1016/j.prostr.2022.01.038

4. Nykyforchyn, H., Lunarska, E., Tsyrulnyk, O.T. et al. (2010) Environmentally assisted "in-bulk" steel degradation of long term service gas trunkline. *Eng. Failure Analysis*, 17(**3**), 624–632. DOI: https://doi.org/10.1016/j.engfailanal.2009.04.007
5. Milenin, O.S., Velykoivanenko, O.A., Rozynka, G.P., Pivtorak, N.I. (2022) Features of analysis of the technical state and support of reliability of the main gas pipelines at transportation of gas-hydrogen mixtures (Review). *The Paton Welding J.*, **6**, 49–56. DOI: https://doi.org/10.37434/tpwj2022.06.07
6. Karkhin, V.A. (2019) *Thermal processes in welding*. Singapore, Springer Singapore.
7. Makhnenko, V. (2013) Problems of examination of modern critical welded structures. *The Paton Welding J.*, **5**, 21–28.
8. Milenin, A., Velikoivanenko, E., Rozynka, G., Pivtorak, N. (2019) Probabilistic procedure for numerical assessment of corroded pipeline strength and operability. *Inter. J. of Pressure Vessels and Piping*, **171C**, 60–68. DOI: https://doi.org/10.1016/j.ijpvp.2019.02.003.
9. BS 7910:2013+A1:2015: *Guide to methods for assessing the acceptability of flaws in metallic structures*. The British Standards Institution.
10. (2007) Fitness-for-service. API 579-1/ASME FFS-1: *Recommended Practice 579*. 2nd Ed. Washington, API Publ. Services.
11. (1997) SNiP 2.05.06–85: *Main pipelines. Construction codes and regulations*. Moscow, VNIIST Minneftegazstroj [in Russian].
12. Hobbacher, A. (2008) *Recommendations for fatigue design of welded joints and components.* IIW Doc. XIII-2151r4-07/XV-1254r4-07. Paris, France, October 2008.
13. Furrer, D.U., Semiatin, S.L. (2009) *ASM Handbook.* Vol. 22A. *Fundamentals of modeling for metals processing*. Edit. Ohio, ASM International.
14. Meng, B., Gu, C.H., Zhang, L. et al. (2017) Hydrogen effects on X80 pipeline steel in high-pressure natural gas/hydrogen mixtures. *Inter. J. of Hydrogen Energy*, 42(**11**), 7404–7412. DOI: https://doi.org/10.1016/j.ijhydene.2016.05.145.
15. Stalheim, D., Boggess, T., SanMarchi, C. et al. (2010) Microstructure and mechanical property performance of commercial grade API pipeline steels in high pressure gaseous hydrogen. In: *Proc. of IPC 2010 8th Inter. Pipeline Conf. Calgary, Canada*.

ORCID
O.S. Milenin: 0000-0002-9465-7710

CONFLICT OF INTEREST
The Authors declare no conflict of interest

CORRESPONDING AUTHOR
O.S. Milenin
E.O. Paton Electric Welding Institute of the NASU
11 Kazymyr Malevych Str., 03150, Kyiv, Ukraine.
E-mail: asmilenin@ukr.net

SUGGESTED CITATION
O.S. Milenin, O.A. Velykoivanenko, G.P. Rozynka, N.I. Pivtorak (2023) Numerical assessment of brittle strength of field welds of the main gas pipelines at transportation of gas-hydrogen blends. *The Paton Welding J.*, **3**, 51–56.

JOURNAL HOME PAGE
https://patonpublishinghouse.com/eng/journals/tpwj

Received: 06.10.2023
Accepted: 24.04.2023